



HAL
open science

Identifying Synthetic Lethal and Selective Approaches to Target PBRM1-Deficiency in Clear Cell Renal Cell Carcinoma

Daphné Morel

► **To cite this version:**

Daphné Morel. Identifying Synthetic Lethal and Selective Approaches to Target PBRM1-Deficiency in Clear Cell Renal Cell Carcinoma. Cancer. Université Paris-Saclay, 2020. English. NNT : 2020UP-ASL017 . tel-04557429

HAL Id: tel-04557429

<https://theses.hal.science/tel-04557429>

Submitted on 24 Apr 2024

HAL is a multi-disciplinary open access archive for the deposit and dissemination of scientific research documents, whether they are published or not. The documents may come from teaching and research institutions in France or abroad, or from public or private research centers.

L'archive ouverte pluridisciplinaire **HAL**, est destinée au dépôt et à la diffusion de documents scientifiques de niveau recherche, publiés ou non, émanant des établissements d'enseignement et de recherche français ou étrangers, des laboratoires publics ou privés.

Identifying synthetic lethal and selective approaches to target PBRM1-deficiency in clear cell renal cell carcinoma

Thèse de doctorat de l'université Paris-Saclay

École doctorale n° 582 :

Cancérologie : biologie - médecine - santé (CBMS)

Unité de recherche : U981, Biomarqueurs prédictifs et nouvelles stratégies thérapeutiques en oncologie, 94800, Villejuif, France.

Référent : Faculté de médecine

Thèse présentée et soutenue à Villejuif, le 12 octobre 2020, par

Daphné MOREL

Composition du Jury

Christophe MASSARD

Professeur des universités-Praticien hospitalier,
Gustave Roussy, Villejuif

Président

Yvan CANITROT

Directeur de recherche, LBCMCP, Toulouse

Rapporteur

Irwin DAVIDSON

Directeur de recherche, IGBMC, Strasbourg

Rapporteur

Fanélie JOUENNE

Assistante Hospitalo-Universitaire, Hôpital Saint Louis,
Paris

Examinatrice

Jean-Charles SORIA

Professeur des universités, Directeur Général, Gustave
Roussy, Villejuif

Invité

Sophie POSTEL-VINAY

Praticien Hospitalier, Directrice d'équipe, Gustave
Roussy, Villejuif

Directrice de thèse

Eric DEUTSCH

Professeur des universités-Praticien hospitalier,
directeur d'équipe, Gustave Roussy, Villejuif

Co-Directeur de thèse

Acknowledgments

A mes directeurs de thèse,

Je souhaite remercier chaleureusement Dr Sophie Postel-Vinay pour son investissement dans ce projet. Elle m'a fait grandir tout au long de cette étude. Je lui dois la naissance de ma passion pour l'écriture, Sophie ayant la plume scientifique et médicale la plus affûtée qu'il m'ait été donné d'admirer. J'ai appris tellement auprès d'elle qu'il en serait impossible d'en visualiser toutes les dimensions, même avec l'aide de Léo et d'une PCA/t-SNE.

Je remercie également chaleureusement Pr Eric Deutsch, auprès de qui je continue l'aventure désormais. Eric est une immense source d'inspiration au quotidien, débordante d'idée, de valeurs et de bienveillance.

Aux membres du jury,

J'adresse un immense merci au Pr Jean-Charles Soria, Monsieur le Président du jury, Monsieur le Directeur Général, grâce à qui toute cette belle Histoire a commencé alors que je n'étais qu'une « petite interne de radiopharmacie en 1^{er} semestre ». Le Pr Soria a été le premier maillon de la chaîne de cette thèse ; c'est un grand honneur pour moi qu'il ait accepté de participer à en sceller le dernier.

Je remercie les Dr Irwin Davidson et Dr Yvan Canitrot d'avoir accepté de juger ce travail en qualité de rapporteurs et d'avoir dégagé du temps pour vous y consacrer. J'ai été touchée que vous ayez répondu favorablement et rapidement à ma demande, et j'espère que ce rapport est à la hauteur de vos attentes.

Je remercie également le Dr Fanélie Jouenne d'avoir accepté de nous apporter son regard de pharmacienne-généticienne sur ces travaux.

A mes collègues,

Je n'aurais absolument rien pu faire sans l'aide généreuse de l'équipe – initialement « thorax », puis « TSPV » – qui m'a formée et soutenue durant ces années. En particulier, je souhaite remercier grandement Nicolas, Marlène, Thomas, Léo et Roman, qui ont largement participé à ma formation scientifique. Je remercie également « les deux » Clémence A. et H., Asuka, Carine, Chloé, Nicolas S., Catherine, Widad, Angélique, Tony, Luc, Ken, Meï, Rosa, Justine, Bojana, Ibrahim, Loïc, Mathieu, Jonathan, Ludovic, Isabelle, Ingrid, Gonzalo, Francesco, Clément, Ramdan, Johan et Caroline, ainsi que toutes les personnes de l'U981 que j'oublie – mais que je n'oublie pas.

Je remercie également tous les collègues et confrères du « bâtiment principal » d'avoir été d'énormes bouffées d'oxygène ; en particulier Julia et Audrey.

A ma famille,

Je remercie encore une fois mes parents de m'avoir soutenue jusqu'au bout... du bout... du bout. J'ai passé mon bac en 2006, voilà qu'à peine 14 ans plus tard, je m'apprête à vivre un mois de septembre sans inscription à la fac. Coup de vieux ! C'est mamie qui va être contente. En tout cas, merci d'avoir toujours été là et de m'avoir suivie dans mes ambitions les plus folles. Vous êtes les meilleurs parents du Monde.

Merci également à toute ma famille, mes grands-parents, mes merveilleux oncles et tantes et surtout mes merveilleuses cousines !

Last but not least, je remercie mon mari et mon fils d'être ma source inépuisable de bonheur. Avec vous, je sais que je peux vivre d'Amour et d'eau fraîche, et ça tombe bien, il y en a au bout du jardin !

Publications

This thesis relates the following publications:

Chabanon RM* & **Morel D***, Colmet-Daage L, Eychenne T, Ilirjana Bajrami I, Dorvault N, Garrido M, Hopkins S, Meisenberg C, Lamb A, Roumeliotis TI, Jouny S, Hénon C, Asuka Kawai-Kawachi A, Astier C, Konde A, Margueron R, Pettitt SJ, Geneviève Almouzni G, Choudhary JS, Soria JC, Deutsch E, Downs J, Lord CJ, Postel-Vinay S. PBRM1 deficiency in cancer is synthetic lethal with DNA repair inhibitors. *In reviewing process for Cancer Discovery since March 24, 2020.*

*Authors share first authorship

Chabanon RM, **Morel D**, Postel-Vinay S. Exploiting epigenetic vulnerabilities in solid tumors: Novel therapeutic opportunities in the treatment of SWI/SNF-defective cancers. *Semin Cancer Biol.* 2020 Apr;61:180-198.

Morel D, Jeffery D, Aspeslagh S, Almouzni G, Postel-Vinay S. Combining epigenetic drugs with other therapies for solid tumours — past lessons and future promise. *Nat Rev Clin Oncol.* 2020 Feb;17(2):91-107

Morel D, Almouzni G, Soria JC, Postel-Vinay S. Targeting chromatin defects in selected solid tumors based on oncogene addiction, synthetic lethality and epigenetic antagonism. *Ann Oncol.* 2017 Feb 1;28(2):254-269

Contributions to other publications related to this work

Chabanon RM, Muirhead G, Krastev DB, Adam J, **Morel D**, Garrido M, Lamb A, Hénon C, Dorvault N, Rouanne M, Marlow R, Bajrami I, Cardeñosa ML, Konde A, Besse B, Ashworth A, Pettitt SJ, Haider S, Marabelle A, Tutt AN, Soria JC, Lord CJ, Postel-Vinay S. PARP inhibition enhances tumor cell-intrinsic immunity in ERCC1-deficient non-small cell lung cancer. *J Clin Invest.* 2019 Mar 1;129(3):1211-1228

Touat M, Sourisseau T, Dorvault N, Chabanon RM, Garrido M, **Morel D**, Krastev DB, Bigot L, Adam J, Frankum JR, Durand S, Pontoizeau C, Souquère S, Kuo MS, Sauvaigo S, Mardakheh F, Sarasin A, Olausson KA, Friboulet L, Bouillaud F, Pierron G, Ashworth A, Lombès A, Lord CJ, Soria JC, Postel-Vinay S. DNA repair deficiency sensitizes lung cancer cells to NAD⁺ biosynthesis blockade. *J Clin Invest.* 2018 Apr 2;128(4):1671-1687

Aspeshagh S, **Morel D**, Soria JC, Postel-Vinay S. Epigenetic modifiers as new immunomodulatory therapies in solid tumours. *Ann Oncol.* 2018 Apr 1;29(4):812-824

Presentations and contribution to other presentations

Chabanon RM, Morel D, Colmet-Daage L, Eychenne T, Dorvault N, Ilirjana Bajrami I, Garrido M, Hopkins S, Meisenberg C, Lamb A, Roumeliotis TI, Jouny S, Astier C, Konde A, Geneviève Almouzni G, Choudhary JS, Soria JC, Downs J, Lord CJ, Postel-Vinay S. - Targeting chromatin remodeling-associated genetic vulnerabilities in cancer: PBRM1 defects are synthetic lethal with PARP and ATR inhibitors – *Oral presentation 1058*, Session VMS.ET04.01 – Novel Targets and Therapies – AACR annual meeting congress 2020

Morel D. Identifying synthetic lethal and selective approaches to target PBRM1-deficiency in clear cell renal carcinoma. Poster presentation – 14eme Journées scientifiques de l'Ecole Doctorale de Cancérologie – Roscoff 2018

Grants and financial supports

This PhD work was greatly supported by:

- Drug Development Department of Gustave Roussy (DITEP) 2016-2018
- INSERM grant "support for translational research in oncology" 2018-2019
- Taxe d'apprentissage 2017 for the realization of whole transcriptomic analysis of 12 human cell lines

Abstract

Introduction

Polybromo-1 (PBRM1) inactivation occurs in multiple malignancies and is of particular importance in clear cell renal cell carcinomas (ccRCC), as it drives 40 to 50% of cases. Currently, no precision-medicine approach uses PBRM1 deficiency to specifically target tumour cells.

Method

To uncover novel synthetic lethal approaches to treat PBRM1-defective cancers, we performed (i) a high-throughput pharmacological screening, evaluating the sensitivity to 167 small molecules in a PBRM1-isogenic cellular model, and the (ii) systematic mapping of the whole transcriptomic and proteomic profiles associated with PBRM1 loss-of-function within this model.

We further investigated the mechanism underlying this synthetic lethal relationship.

Results

We identified and validated synthetic lethal effects between PBRM1 loss and both PARP and ATR inhibition. Combinatorial use of PARP with ATR inhibitors exerted additive cytotoxic effects in PBRM1-defective tumour cells.

These synthetic lethal relationships were characterized by a pre-existing replication stress in PBRM1-deficient cells associated with mitosis and DNA damage repair abnormalities, which were exacerbated upon PARP inhibition selectively in PBRM1-defective cells.

Conclusion

These data provide the preclinical basis for evaluating PARP inhibitors as a monotherapy or in combination in patients with PBRM1-deficient ccRCC.

Table of contents

Acknowledgments	- 4 -
Publications	- 7 -
This thesis relates the following publications:	- 7 -
Contributions to other publications related to this work	- 7 -
Presentations and contribution to other presentations	- 8 -
Grants and financial supports	- 9 -
Abstract	- 10 -
Table of contents	- 12 -
List of figures	- 16 -
List of tables	- 18 -
List of acronyms	- 19 -
List of genes and proteins	- 20 -
Chapter I: Introduction	- 22 -
Part I: Clear cell renal cell carcinoma	- 22 -
I. Epidemiology of kidney cancer	- 22 -
II. Definition of clear cell renal cell carcinoma	- 24 -
III. Molecular characterization of clear cell renal cell carcinoma	- 26 -
a. Primary tumour	- 26 -
b. Metastases	- 31 -
IV. Current clinical practice guidelines	- 33 -
a. Stage and risk assessment	- 34 -
b. Local/locoregional disease	- 37 -
c. Advanced and metastatic disease	- 37 -
Part II: SWI/SNF alterations in cancer	- 42 -
I. Epigenetics, chromatin modifiers and SWI/SNF complexes	- 42 -
a. Epigenetics: definition and discovery	- 42 -
b. Epigenetics: implication in carcinogenesis	- 45 -
	- 12 -

II.	SWI/SNF alterations in cancer: description and incidence	- 47 -
III.	Targeting SWI/SNF alterations in cancer	- 51 -
a.	Concepts of synthetic lethality and epigenetic antagonism	- 51 -
b.	Tumour vulnerability linked to SWI/SNF deficiency	- 52 -
Part III: PBRM1		- 56 -
I.	Genetic background	- 56 -
II.	Protein roles	- 57 -
a.	DNA repair	- 58 -
b.	Transcription	- 59 -
c.	Mitosis and cytoskeleton	- 59 -
III.	High-potential drug candidates for targeting PBRM1-defects	- 60 -
Part IV: Objectives, summation of the rationale to target PBRM1-deficiency in advanced ccRCC		- 62 -
Chapter II: Materials and Methods		- 64 -
I.	Tumour cell lines	- 64 -
II.	Probes	- 66 -
a.	Drugs	- 66 -
b.	Antibodies	- 66 -
c.	Other chemicals	- 67 -
III.	Protocols	- 68 -
a.	Preliminary screening	- 68 -
b.	Proliferation assays	- 69 -
c.	Western blot and co-immunoprecipitation	- 70 -
d.	Immunofluorescence and image analysis	- 70 -
e.	Time-lapse microscopy	- 71 -
f.	RT-qPCR	- 71 -
g.	DNA combing	- 72 -
h.	Proteomic and transcriptomic analyses of HAP1 cells	- 72 -
i.	DRIP-seq	- 75 -
IV.	Statistical analysis	- 76 -
Chapter III: Characterization of a PBRM1-isogenic cellular model		- 77 -
I.	Introduction and preliminary work	- 77 -
II.	Systematic characterizations of the HAP1 PBRM1-isogenic model	- 78 -
a.	Transcriptional characterization of the HAP1 model	- 78 -
b.	Proteomic characterization of the HAP1 model	- 80 -
III.	Discussion	- 82 -

Chapter IV: PBRM1-deficiency associates with increased sensitivity to PARP inhibitors - 84 -

I.	Introduction	- 84 -
II.	Results	- 84 -
a.	High-throughput drug screening	- 84 -
b.	Low-throughput validation in isogenic cellular models	- 91 -
c.	PBRM1-rescue restores initial phenotype	- 95 -
d.	Enlarging the findings to non-isogenic cellular model of ccRCC	- 95 -
III.	Discussion	- 96 -

Chapter V: PBRM1 loss associates with enhanced genomic instability and replication stress- 98 -

I.	Introduction	- 98 -
II.	Results	- 100 -
a.	Impact of PBRM1 loss on protein involved in PARPi response	- 100 -
b.	γ H2AX and RAD51 foci formation	- 101 -
c.	Mutational load of PBRM1-defective tumours	- 103 -
d.	Micronuclei formation	- 104 -
e.	Mitotic spindle abnormalities	- 106 -
f.	Impact of PBRM1 loss on the SWI/SNF stoichiometry	- 111 -
g.	Nucleolus fragmentation	- 113 -
h.	Replication fork progression	- 115 -
i.	Discussion	- 118 -

Chapter VI: PARPi exposure overtakes the capacity of PBRM1-deficient cells to maintain a phenotype suitable with survival - 121 -

I.	Introduction	- 121 -
II.	Results	- 123 -
a.	DNA damage response following PARPi	- 123 -
b.	Mitosis abnormalities	- 125 -
c.	R-loop quantification	- 127 -
d.	R-loop resolution defects of PBRM1-KO cells	- 133 -
III.	Discussion	- 135 -

Chapter VII: Conclusion, discussion and perspectives - 136 -

I.	Critical findings resulted from this PhD work	- 136 -
II.	Final discussion and perspectives	- 140 -

References - 149 -

ABSTRACTS - 161 -

List of figures

Figure 1. Estimated age-standardized incidence rates of kidney cancer in 2018	- 22 -
Figure 2. Estimated age-standardized mortality rates of kidney cancer in 2018	- 23 -
Figure 3. Simplified physiologic anatomy of the kidney	- 25 -
Figure 4. Micrograph at 100 X magnification of a nephrectomy sample	- 25 -
Figure 5. Overview of somatic driver alterations found in 101 ccRCC primary tumours from TRACERx Renal study	- 27 -
Figure 6. ccRCC phylogenetic trees	- 29 -
Figure 7. Mutational profiles of PBRM1, SETD2 and BAP1 in ccRCC samples from TCGA.	- 30 -
Figure 8. Fishplot of 3 hypothetical ccRCC typical evolutions over time	- 32 -
Figure 9. Algorithm for first-line and later-lines systemic treatment of advanced and metastatic ccRCC	- 39 -
Figure 10. Schematic representation of histone marks and global functional consequences following their alteration and in cancer.	- 44 -
Figure 11. Structure and composition of mSWI/SNF complexes.	- 48 -
Figure 12. mSWI/SNF subunit mutation rate disparities across human cancers	- 50 -
Figure 13. Mechanism-based approach for targeting loss-of-function mutation in human cancer.	- 52 -
Figure 14. PBRM1 genomic and proteic characteristics.	- 56 -
Figure 15. Known implications of PBRM1 within the cell cycle and other cellular functions	- 61 -
Figure 16. Western blot of PBRM1 expression on total cell extracts in four PBRM1-isogenic cellular models and four non-isogenic ccRCC cell lines. Actin is shown as a loading control.	- 78 -
Figure 17. GSEA displaying the top 20 of up- and down-regulated GO Biological Processes pathways in the transcriptome analysis of HAP1 PBRM1-KO cells compared to	- 80 -
Figure 18. GSEA displaying the top 20 of up- and down-regulated GO Biological Processes pathways in the proteome analysis of HAP1	- 81 -
Figure 19. High-throughput drug screen on PBRM1-WT and -KO HAP1 cells.	- 85 -
Figure 20. Low-throughput validation of PARPi sensitivity.	- 92 -
Figure 21. Dose-response colony-forming assay	- 93 -
Figure 22. Additivity effects on cell survival of PARPi combined with ATRi	- 94 -
Figure 23. PARPi sensitivity following PBRM1 rescue.	- 95 -
Figure 24. PARPi sensitivity in non-isogenic ccRCC cell lines.	- 96 -
Figure 25. Volcano plot showing the significantly dysregulated proteins	- 100 -
Figure 26. Quantification of γ H2AX and RAD51 foci per cells according to PBRM1 status.	- 102 -
Figure 27. Mutational load of tumours according to PBRM1 mutation and expression.	- 104 -
Figure 28. Micronuclei quantification according to PBRM1 status	- 105 -
Figure 29. Mitosis abnormalities observation.	- 107 -
Figure 30. PBRM1 immunofluorescent labeling.	- 108 -
Figure 31. Spindle poles observation.	- 110 -
	- 16 -

<i>Figure 32. Western blot of selected SWI/SNF subunits expressions</i>	- 112 -
<i>Figure 33. Nucleoli observation.</i>	- 114 -
<i>Figure 34. Replication stress assessment.</i>	- 117 -
<i>Figure 35. Quantification of γH2AX and RAD51 foci after exposure to PARPi.</i>	- 123 -
<i>Figure 36. Micronuclei quantification after exposure to PARPi.</i>	- 124 -
<i>Figure 37. Sensitivity to other DSB-inducers.</i>	- 125 -
<i>Figure 38. Mitosis abnormalities after exposure to olaparib</i>	- 126 -
<i>Figure 39. DRIP-sequencing of PBRM1-isogenic models.</i>	- 128 -
<i>Figure 40. Genomic localisations of DNA-RNA hybrids according to PBRM1 status.</i>	- 130 -
<i>Figure 41. Impact of talazoparib exposure on DNA-RNA hybrids.</i>	- 132 -
<i>Figure 42. DNA-RNA helicases expressions according to PBRM1 status</i>	- 134 -
<i>Figure 43. Model of PBRM1 defect-dependent cytotoxicity following exposure to DNA repair inhibitors.</i>	- 138 -

List of tables

<i>Table 1. Distribution and 5-year relative survival rates according to stage at diagnosis of kidney cancer (including renal pelvis).</i>	- 24 -
<i>Table 2. 2017 TNM classification system together with stage grouping ³⁰</i>	- 35 -
<i>Table 3. IMDC risk factors and associated risk groups ³¹</i>	- 36 -
<i>Table 4. International non-proprietary name (INN), type and year of European first approval of drugs which compose the current therapeutic arsenal for systemic treatment of advanced and metastatic ccRCC.</i>	- 38 -
<i>Table 5. Gene names and related mutation frequency in the pooled PanCancer Atlas cohort of TCGA</i>	- 46 -
<i>Table 6. Synthetic lethal interactions involving SWI/SNF loss-of-functions that have been described in preclinical models</i>	- 53 -
<i>Table 7. List of the cell lines used for this work</i>	- 65 -
<i>Table 8. List of primary antibodies that were used for this work for WB or IF</i>	- 67 -
<i>Table 9. List of other chemicals, including RT-qPCR primers</i>	- 68 -
<i>Table 10. High-throughput small molecule inhibitor screen</i>	- 86 -

List of acronyms

Acronym	Alias
ATRi	Inhibitor of ATR
AUC	Area Under the Curve
BAF	BRG1- or BRM-associated factors
BAH	Bromodomain-Adjacent Homology domain
BD	BromoDomain
cBAF	canonical BAF
ccRCC	Clear Cell Renal Cell Carcinoma
CI	Confidence Interval
DNA	DeoxyriboNucleic Acid
DSB	Double-Strand Break
HMG	High-Mobility Group box
HR	Homologous Recombination / Hazard Ratio
ncBAF	non-canonical BAF
NES	Normalized Enriched Score
NHEJ	Non-Homologous End Joining
PARPi	Inhibitor of PARP
pBAF	polybromo-associated BAF
PS	Performans Status
RNA	RiboNucleic Acid
TNM	Tumor Nodes Metastases

List of genes and proteins

Protein or gene	Alias
AKT	Serine/Threonine Kinase
ARID1A/1B/2	AT-Rich Interaction Domain 1A/1B/2
BAP1	BRCA Associated Protein 1
BIM	Bcl2 Interacting Mediator of Cell Death
BRCA1/2	BRest CAncer 1/2
BRD2/3/4/T	BRomDomain containing 2/3/4/T
CCND1	Cyclin D1
CREBBP	CREB Binding Protein
DOT1L	DOT1-like
EGF	Endothelial Growth Factor
ERCC1	Excision Repair Cross-Complementation group 1
EZH2	Enhancer Of Zeste 2 Polycomb Repressive Complex 2 Subunit
HDAC1/11	Histone DeACetylase 1/11
HER2	Human Epidermal Growth Factor Receptor 2
HIF1 α	Hypoxia-inducible factor α
Hsp90	Heat Shock Protein 90kDa
KMT2C/2D	K MethylTransferase 2C/2D
LSD1	LySine Demethylase 1
MDR1	Multi-Drug Resistance 1
MRP	Multidrug Resistance Protein
mTOR	Mechanistic Target Of Rapamycin Kinase
p53	Tumor Protein P53
PARP	Poly(ADP-Ribose) Polymerase
PBRM1	PolyBRoMo1
PI3K	Phosphatidylinositol 3 Kinase
PRMT5	Protein Arginine MethylTransferase 5
SETD2	SET Domain Containing 2
SIRT1/7	Sirtuin 1/7
SMARCA2/A4/B1	SWI/SNF-Related Matrix-Associated Actin-Dependent Regulator Of Chromatin A2/A4/B1
VEGF	Vascular Endothelial Growth Factor
VHL	Von Hippel-Lindau
XPA	Xeroderma Pigmentosum complementation group A

Part I: Clear cell renal cell carcinoma

I. Epidemiology of kidney cancer

Incidence: In 2018, kidney cancer affected over 400,000 new patients worldwide and caused approximately 175,000 deaths ¹. Renal cancer affects approximately two men for one woman (sex ratio: 2.0) and is of particular significance within Central and Western Europe, with the highest incidence rates ($> 10.0/100,000$ inhabitants) being observed in Czech Republic (12.9/100,000), Slovakia (12.1/100,000), Hungary and France (both 11.2/100,000) (Figure 1).



Figure 1. Estimated age-standardized incidence rates of kidney cancer in 2018
(source: WHO IARC GLOBOCAN 2018 assessed on May, 2020)

Risk factors: Overall, incidence and mortality rates are higher in the richest countries (Figure 1, 2), which indicates a potential role of lifestyle as a risk factor. Access to imaging facilities with advanced diagnostic techniques may also contribute to increase

statistics in developed countries. Established lifestyle risk factors include tobacco smoking, obesity (body mass index > 35 kg/m²) and hypertension ^{2,3}, while fruits, fiber-rich vegetables and coffee consumption, together with physical activity, seem to have a protective effect ⁴⁻⁶. Chronic kidney disease has also been linked to higher risk of developing kidney cancer (HR 2.58, 95% CI [1.21–5.50]) ³.

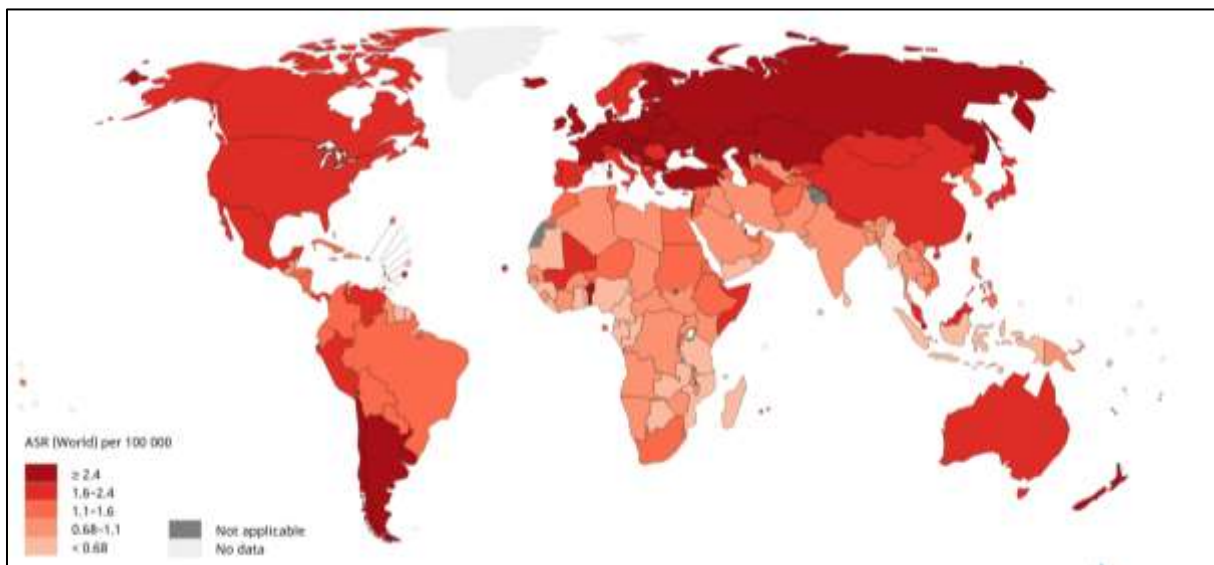


Figure 2. Estimated age-standardized mortality rates of kidney cancer in 2018
(source: WHO IARC GLOCOBAN 2018 assessed on May, 2020)

Heredity: Kidney cancer predominantly occurs in sporadic forms; however, a small proportion (2-4%) shows Mendelian inheritance within familial forms. Most of these cases are caused by germ-line mutations in the Von Hippel-Lindau (*VHL*) gene (von Hippel-Lindau disease), but other genetic conditions can lead to kidney cancer, such as tuberous sclerosis, Birt-Hogg-Dubé syndrome, hereditary leiomyomatosis, hereditary papillary renal carcinoma (HPRC) etc. ^{7,8}. Systematic screening for both renal and extra-renal cancer within these families is not systematically recommended and depends on the syndrome.

Prognosis: Approximately 50 to 90% of patients diagnosed with kidney cancer are still alive five years after diagnosis, with important disparities according to geographic, age and tumour-related parameters (e.g. tumour type, primary tumour size, overall tumour stage (TNM), Fuhrman grade, the presence of necrosis and molecular complexity) ^{9,10}. The 5-year survival rate of patients diagnosed with stage 1 (localized) disease is superior to 90%, while only 12% of patients who had developed metastasis are still alive after five years (Table 1).

Table 1. Distribution and 5-year relative survival rates according to stage at diagnosis of kidney cancer (including renal pelvis). Data were retrieved from the American Cancer Society 2020 report ¹¹that exploited cancer cases declared in the United States between 2009 and 2015.

Stage when first diagnosed	Distribution of stage at diagnosis	5-year survival rate
Localized	65%	93%
Loco-regional	16%	70%
Metastatic	16%	12%

II. Definition of clear cell renal cell carcinoma

Renal cell carcinoma (RCC) develops from renal parenchyma (Figure 3) and corresponds to 85-90% of all kidney cancer. Among multiple subtypes, clear cell renal cell carcinoma (ccRCC) represents the most common form of RCCs and accounts up to 80% of cases ^{12,13}. CcRCC can be found anywhere in the renal cortex (Figure 3). To note, the statistics cited above include not only ccRCC and other parenchymal tumours, but also urothelial tumours of the renal pelvis (all kidney cancer types), and therefore, prognosis data are more optimistic than reality for ccRCC.

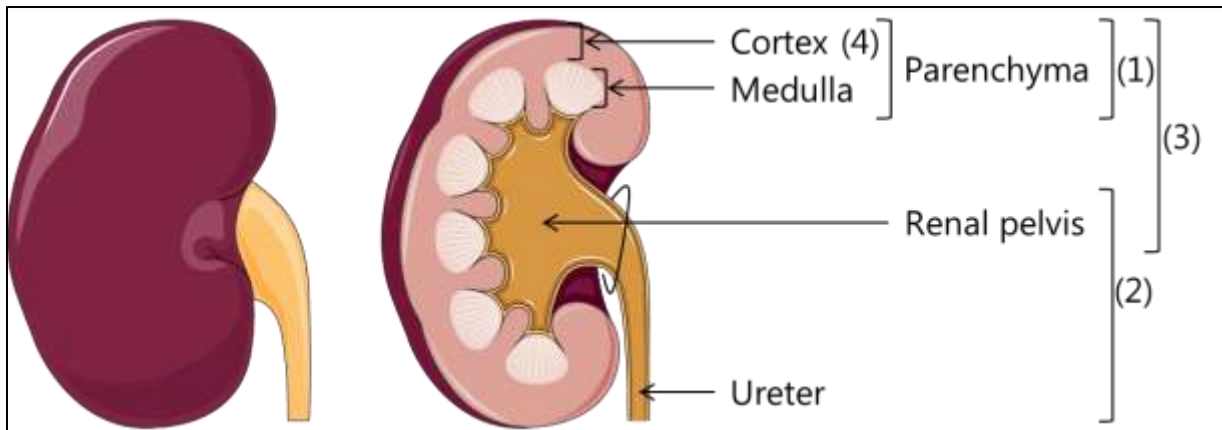


Figure 3. Simplified physiologic anatomy of the kidney with localizations of different types of kidney cancer: (1) renal-cell cancer, (2) urothelial cancer, (3) kidney cancer, includes renal cell cancer and renal pelvis carcinoma. Clear cell renal cell carcinoma develops against the cortical tissue (4).

The discovery is often fortuitous, thus 60% to 80% of ccRCC are found incidentally on imaging performed for other purpose. The final diagnosis shall be made by pathological examination of the nephrectomy sample, which typically shows malignant epithelial cells with water-clear cytoplasm, organized in nests (Figure 4). The classical presentation with clear cytoplasm is due to the abnormal cholesterol metabolism of these cells, which leads to lipid and glycogen accumulation in the cytoplasmic compartment¹⁴.

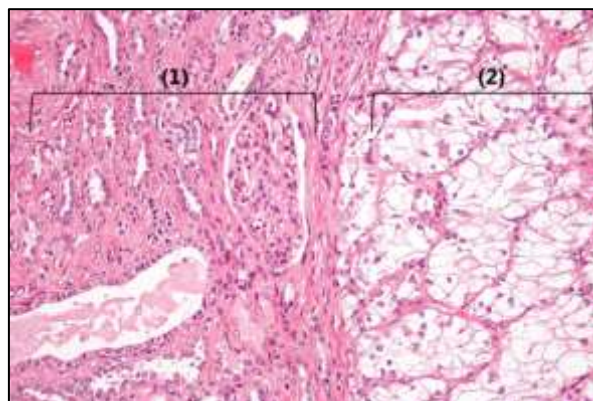


Figure 4. Micrograph at 100 X magnification of a nephrectomy sample after haematoxylin and eosin staining (H&E stain) showing both the non-tumoral kidney on the left (1) and typical ccRCC with Fuhrman grade 2/4 on the right (2). Original picture free from rights of unknown source, adapted from Wikipedia, last accessed on 12/05/2020.

III. **Molecular characterization of clear cell renal cell carcinoma**

a. **Primary tumour**

More than 30 years ago, *Zbar et al.* used a restriction fragment length polymorphisms (RFLP) technic to first identify the specific loss of part of the short arm of the chromosome 3 in 100% of 11 sporadic ccRCC samples, with the breakpoint clustering between 3p11 and 3p21 ¹⁵. Since then, our understanding of ccRCC drastically evolved, thanks to comprehensive genomic, epigenomic, transcriptomic and proteomic analysis of hundreds of cases using next-generation technics. In particular, The Cancer Genome Atlas (TCGA) Research Network and the International Cancer Genome Consortium (ICGC) with the CAGEKID (Cancer Genomics of the Kidney) project are considerable resources which collected and profiled more than 500 samples each of primary ccRCC tumours ^{16,17}. Additionally, the TRACKing Cancer Evolution through therapy (Rx) (TRACERx) study analyzed to date more than 1,200 primary tumour samples from 101 ccRCC patients (interim findings published in 2018, with final target accrual of 320 patients) ⁹. This project aims at drawing multi-region genomic profiling of ccRCCs and therefore at providing a comprehensive picture of the disease's subclonal heterogeneity.

The molecular characterization of sporadic ccRCC is characterized by the early loss of part of chromosome 3p - a pathognomonic event that drives up to 95% of ccRCC cases, as described 30 years ago (Figure 5) (cbioportal KIRC PanCancer Atlas, assessed on 13/05/2020; ⁹). The 3p chromosome fragment encompasses four genes commonly mutated in all cancer types, namely *VHL*, *PBRM1*, *SETD2* and *BAP1*. As these are tumour-suppressor genes located on an autosomal chromosome, complete loss of function shall require parallel event on the second copy of the gene, which usually results from a deleterious mutation or an epigenetic silencing through methylation of the promoter in the case of *VHL* (Figure 5). Thus, complete dysfunction of one, two or

three of these proteins is universally observed in ccRCC; however, complete loss of all of these four genes has never been described simultaneously within the same tumour subclone, suggesting that it may not be compatible with cell survival.

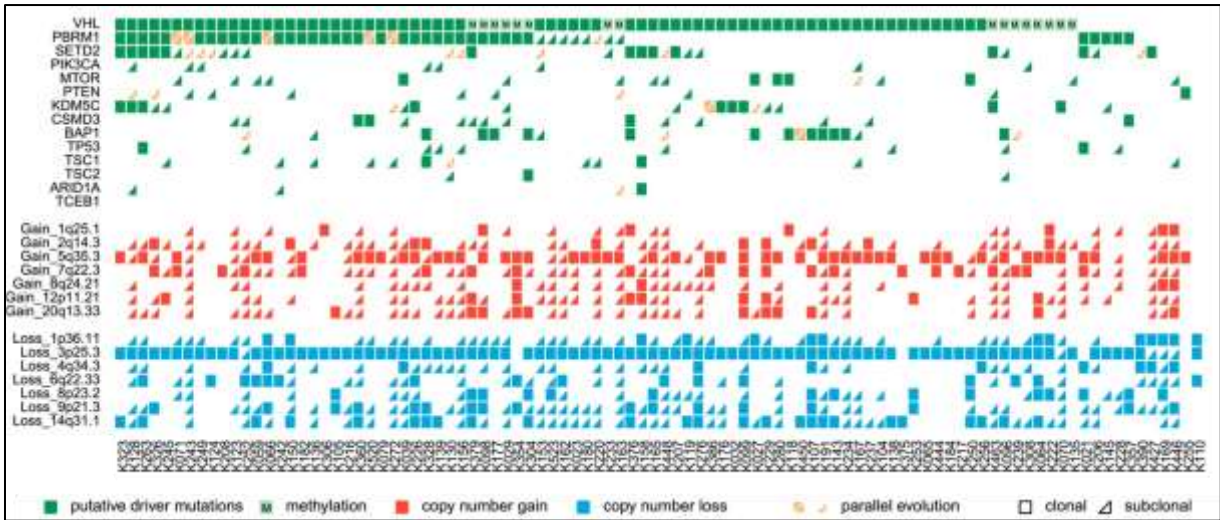


Figure 5. Overview of somatic driver alterations found in 101 ccRCC primary tumours from TRACERx Renal study, with the detail of whether the alteration was clonal (square) or subclonal (triangle). Each column represents one patient’s tumour genomic profile. Green “M” represent epigenetic silencing of the gene by overmethylation. Cropped from *Turajlic et al, Cell 2018*.

In ccRCC, the median number of driver events – defined as putative driver genes whose alteration is highly suspected to be related to cancer apparition or evolution – is often three, but up to 30 drivers events per tumour have been observed ⁹. Regarding total non-silent mutation count, the median mutational load of ccRCC is 52 in the TCGA cohort (n=512 cases), ranged from eight to 591 mutations per tumour (cbioportal KIRC PanCancer Atlas, assessed on 13/05/2020).

Driver events have been classified into three major groups ^{9,18,19}:

- Predominant truncal drivers – which are 3p loss and *VHL* mutations/methylation – ubiquitous events necessary to initiate tumour growth in a large majority of ccRCC (about 90% of cases)

- Facultative, early truncal drivers – which are *PBRM1* or *BAP1* mutations, 5q gain, 4q loss, 8p loss or 14q loss – acquired early during the evolution of the tumour, but in some cases may be found only in subclones (about 80% of cases harbor at least one of these alterations)
- Subclonal drivers (the largest group) – which include *SETD2*, *PTEN*, *TP53*, *KDM5C*, *PIK3CA* or *mTOR* alterations, 6q loss, 7p/7q gain, among others – found almost exclusively in subclones, suggesting their implication in disease evolution rather than initiation (about 40% of cases).

The order in which driver events are acquired during ccRCC evolution is complex to investigate, although multi-region sequencing of hundreds of ccRCC cases and their intra-tumoral heterogeneity analysis allowed identifying three main paths that encompass up to 90% of ccRCC cases^{9,18,20} (Figure 6):

- 3p loss + *VHL* mutation/methylation ► *PBRM1* mutation ► somatic copy number alteration (SCNA)
- 3p loss + *VHL* mutation/methylation ► *PBRM1* mutation ► *SETD2* or *PTEN* mutation or PI3K/AKT/mTOR pathway alteration
- 3p loss + *VHL* mutation/methylation ► *BAP1* mutation

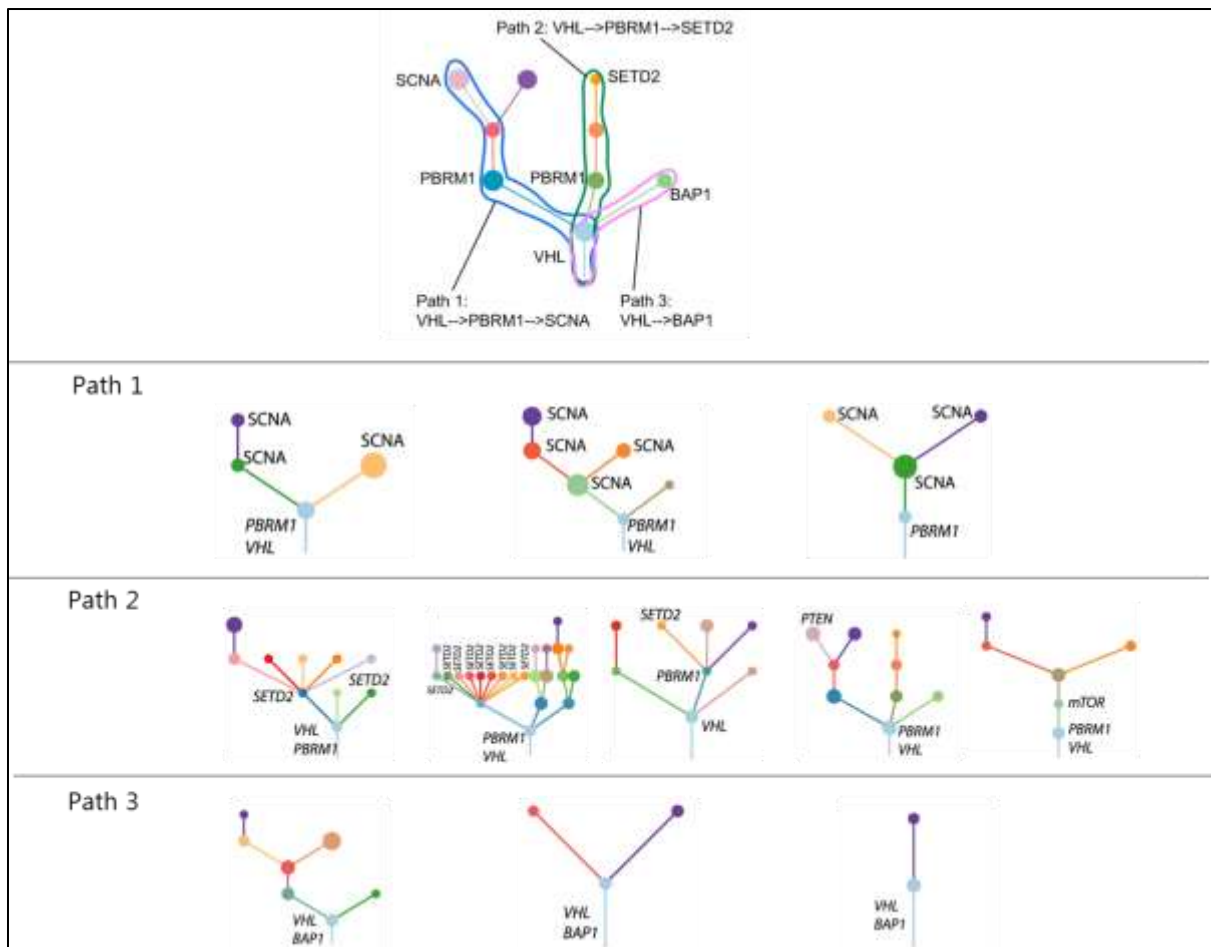


Figure 6. ccRCC phylogenetic trees. Up: illustrative schematic tree illustrating the three main evolutionary paths of occurrence of driver mutations in ccRCCs. Down: Examples of phylogenetic trees from ccRCC cases dissected for the TRACERx Renal study. At least 3 examples per evolution-type are shown. Adapted from *Turajlic et al, Cell 2018*

While *PBRM1* and *SETD2* alterations tend to co-occur and both proteins are largely co-expressed (Figure 7), a mutual exclusivity has been described between *BAP1* mutation and *PBRM1/SETD2* mutation, meaning that loss of function of both *BAP1* and *PBRM1* or *SETD2* might be lethal for the cells^{21,22}. Cases where *BAP1* and *PBRM1/SETD2* mutations were found to co-occur at a patient's level have been observed (Figure 5, ^{9,20}); however, *Turajlic et al.* demonstrated that these alterations were located in spatially separated major subclones of the tumour and were never found to co-occur at a subclonal level, within the same tumour cell⁹. Furthermore, this observation has been linked to the aggressiveness of the ccRCC subgroup that

displays concurrent loss of expression of both PBRM1 and BAP1, also called the “multiple clonal drivers” subtype.

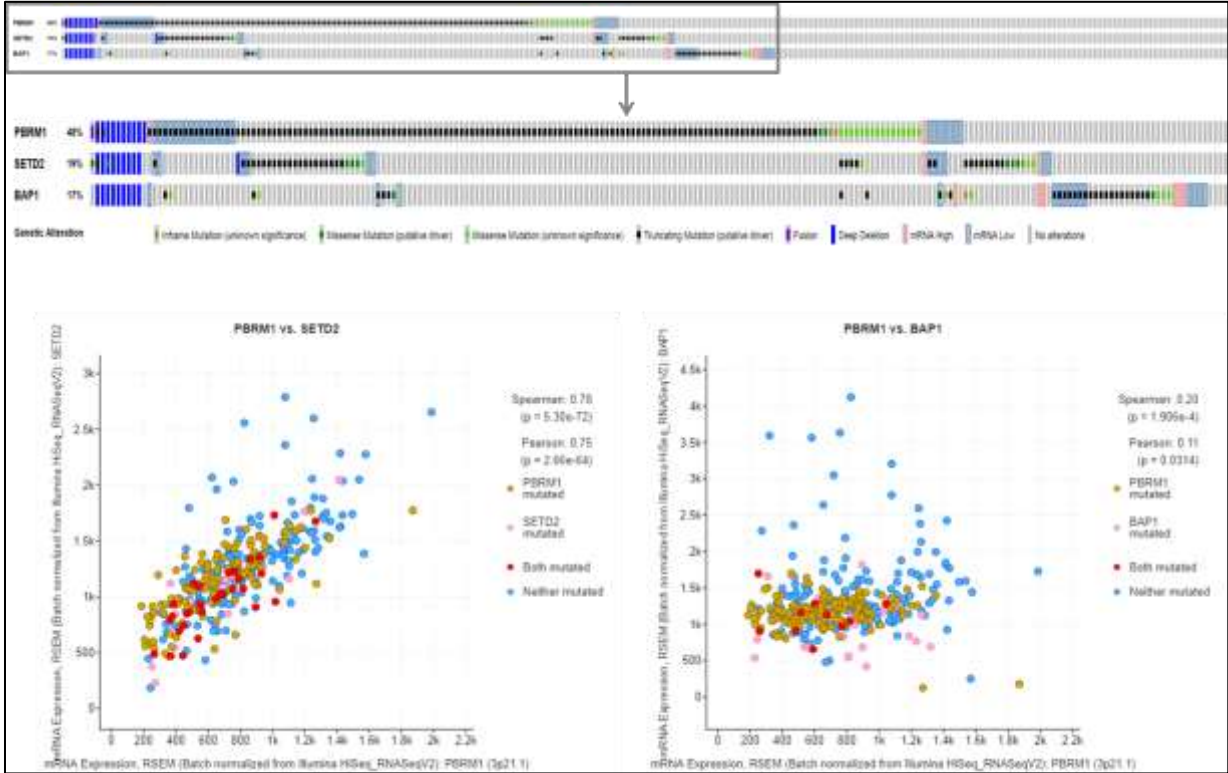


Figure 7. Mutational profiles of PBRM1, SETD2 and BAP1 in ccRCC samples from TCGA. Top: waterfall plot of genetic alterations within PBRM1, SETD2 and BAP1 in the TCGA ccRCC cohort (n= 352 cases). Each vertical feature corresponds to one sample where PBRM1 and/or SETD2 and/or BAP1 can be found altered. Bottom: dot plot of mRNA expressions of PBRM1 (x-axis) and SETD2 or BAP1 (left and right plots, respectively, on the y-axis) in the TCGA ccRCC cohort (n= 352 cases). Data were retrieved from cbiportal.org using the KIRC PanCancer Atlas cohort, last accessed on 14/05/2020.

b. **Metastases**

Large-scale sequencing projects such as the above-mentioned TCGA and ICGC focused on primary tumours profiling. Similar studies on metastases remained limited until the TRACERx Renal project published their analysis of 100 cases of metastatic ccRCC with matched biopsies from 575 primary sites and 335 paired metastatic sites²³. Their main findings are illustrated in Figure 8: (1) metastatic sites harbored less subclonal heterogeneity than primary sites, (2) the loss of chromosome 9p was a potent driver of both metastatic progression ($p = 0.0026$, $p_{adj} < 0.1$) and mortality risk (HR [95%CI] = 7.7 [2.8–20.8]) and may represent the main hallmark of ccRCC metastasis, (3) 14q loss also trended to be significantly enriched within metastatic sites ($p = 0.0275$, $p_{adj} = 0.303$), and (4) both loss of 9p and 14q were found in 71% of ccRCC metastases compared to 35% of non-metastatic primary tumours.

To note, 9p encompasses the *CDKN2A* gene which encodes for the p16 protein and 14q encompasses *hypoxia-inducible factor-1 A (HIF1A)* which encodes for HIF1 α , both proteins are implicated in the regulation of the vascular endothelial growth factor (VEGF).

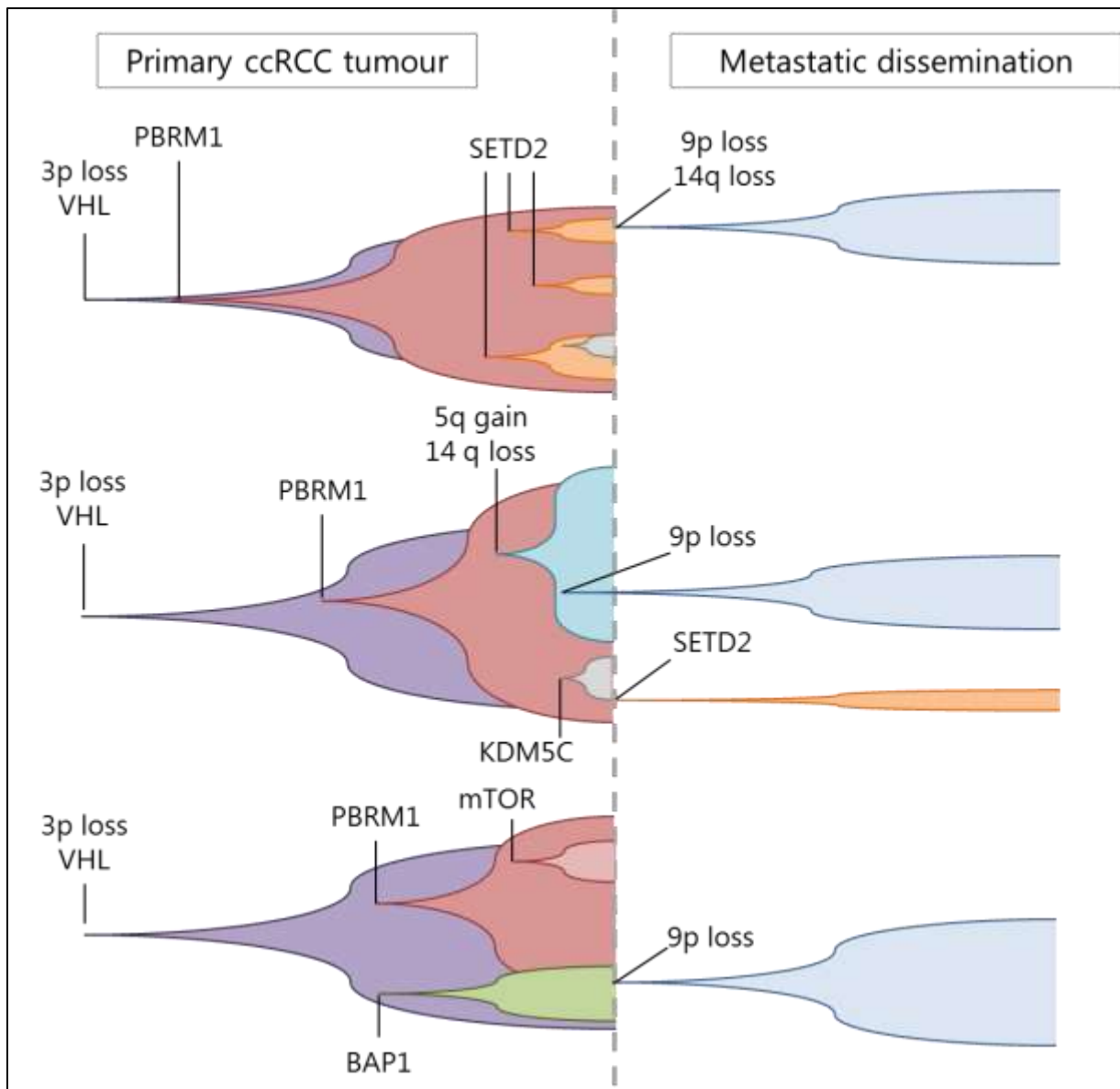


Figure 8. Fishplot of 3 hypothetical ccRCC typical evolutions over time, regarding acquisition of subclonal mutations and transition to a metastatic stage. Inspired from actual multiregion analysis of matched primary/metastatic ccRCC cases from TRACERx Renal study, described in 23

Other studies intended to compare genetic/proteic patterns of metastases to primary sites of metastatic ccRCC. Using immunochemistry assay to assess PBRM1 and BAP1 expressions on matched primary-metastases samples from 97 patients, *Eckel-Passow J et al.* found that patients' primary tumour was BAP1-negative in 20% of cases and PBRM1-negative in 57% of cases, including 6% of cases that were both BAP1- and PBRM1-negative²⁴. All patients whose primary site showed loss of one or both

expressions had consistently negative results on the metastatic sites. Additionally, two (2%) patients had BAP1-negative metastases while BAP1-positive primary site, and seven (7.2%) patients had PBRM1-negative metastases while PBRM1-positive primary site, suggesting that the emergence of BAP1 or PBRM1 alteration participated in cancer progression in these cases. This is in line with previous observation of *Pawlowski et al.*, who described a complete loss-of-expression of PBRM1 (assessed by immunochemistry) in 68% of 227 ccRCC samples, which was significantly correlated with advanced tumour stage ($p < 0.0001$), low differentiation grade ($p = 0.0002$) and poorer survival ($p = 0.025$)²⁵.

Using targeted next-generation sequencing of approximately 260 cancer-related genes on two cohorts of 349 ccRCC primary tumours compared to 229 unmatched metastases (cohort 1) and 177 ccRCC primary tumours compared to 80 unmatched metastases (cohort 2), *de Velasco et al.* only identified a significantly increased frequency of *TP53* mutation in metastases compared to primary tumours (14.9% *versus* 8.9%; $p = 0.031$) in cohort 1, which was not observed in cohort 2 (16.3% *versus* 12.3%; $p = 0.56$)²⁶. In cohort 1, *PBRM1* was mutated in 47.1% of metastatic cases and 39.2% of primary tumours ($p = 0.09$). Other known drivers' frequency of mutations was not significantly different between primary sites and metastases (including *VHL*, *SETD2*, *BAP1*, *KDM5C*, *PTEN*, *TSC1* and *TET2*).

IV. **Current clinical practice guidelines**

The objective of this background information is to identify the clinical need of innovative biomarker in ccRCC treatment and to appraise how this PhD work could impact clinical practice in the relatively-short term.

In the past few months, clinical practice guidelines drastically evolved following the 2019 publications of results from major randomized clinical trials. The latest versions (available on May, 2020) of European Association of Urology (EAU) Guidelines ¹⁰, ESMO Guidelines ²⁷ and NCCN Guidelines (V2.2020) ²⁸ were screened to draw the following – simplified – chart of management of ccRCC. As this pre-clinical work mostly focused on systemic treatments, emphasis is put on advanced and metastatic ccRCC disease for which local intervention is either not feasible or not sufficient to achieve favorable survival outcome.

a. **Stage and risk assessment**

Therapeutic options for ccRCC clinical management depend on the prognosis at the time of diagnosis, which is influenced by:

- Extent of the disease (stage), which should be assessed using the TNM classification system (Table 2);
- Histological factors such as sarcomatoid features, microvascular invasion and tumour necrosis;
- Grading, mostly using the Fuhrman nuclear grading system ²⁹;
- Clinical and biological factors that have been shown to have prognostic value, including performance status (PS), local symptoms, cachexia, hematological disturbance, increased CRP and decreased albuminemia.

Table 2. 2017 TNM classification system together with stage grouping ³⁰

T - Primary Tumour				
TX	Primary tumour cannot be assessed			
T0	No evidence of primary tumour			
T1	Tumour < 7 cm or less in greatest dimension, limited to the kidney			
	T1a	Tumour < 4 cm or less		
	T1b	Tumour > 4 cm but < 7 cm		
T2	Tumour > 7 cm in greatest dimension, limited to the kidney			
	T2a	Tumour > 7 cm but < 10 cm		
	T2b	Tumours > 10 cm, limited to the kidney		
T3	Tumour extends into major veins or perinephric tissues but not into the ipsilateral adrenal gland and not beyond Gerota fascia			
	T3a	Tumour grossly extends into the renal vein or its segmental (muscle-containing) branches, or tumour invades perirenal and/or renal sinus fat (peripelvic fat), but not beyond Gerota fascia		
	T3b	Tumour grossly extends into the vena cava below diaphragm		
	T3c	Tumour grossly extends into vena cava above the diaphragm or invades the wall of the vena cava		
T4	Tumour invades beyond Gerota fascia (including contiguous extension into the ipsilateral adrenal gland)			
N - Regional Lymph Nodes				
NX	Regional lymph nodes cannot be assessed			
N0	No regional lymph node metastasis			
N1	Metastasis in regional lymph node(s)			
M - Distant Metastasis				
M0	No distant metastasis			
M1	Distant metastasis			
pTNM stage grouping				
Stage I	T1	N0	M0	
Stage II	T2	N0	M0	
Stage III	T3	N0	M0	
	T1, T2, T3	N1	M0	
Stage IV	T4	Any N	M0	
	Any T	Any N	M1	

For stage III-IV disease, although multiple risk assessment scores exist, recent clinical trials often used the Metastatic Renal Cancer Database Consortium (IMDC) risk model to segregate patients into three categories: favorable-risk group, intermediate-risk group and high-risk group, based on prognostic factors for overall survival (Table 3)³⁰. To note, IMDC criteria were partly inspired by the MSKCC criteria³¹, which are quite similar and share four prognostic factors, detailed in Table 3.

Table 3. IMDC risk factors and associated risk groups³¹

Risk factors	Cut-off point used
Karnofsky performance status*	< 80%
Time from diagnosis to treatment*	< 12 months
Haemoglobin*	< Lower limit of laboratory reference range
Corrected serum calcium*	> 10.0 mg/dL (2.4 mmol/L)
Absolute neutrophil count (neutrophilia)	> upper limit of normal
Platelets (thrombocytosis)	> upper limit of normal

Score	Group
0	low (good)-risk
1-2	intermediate-risk
3-6	high (poor)-risk

*Risk factors that are shared with MSKCC score

b. Local/locoregional disease

Briefly, when the disease is confined to the kidney with a size inferior to 7 cm, partial nephrectomy is recommended, while radical nephrectomy is preferred when the tumour is larger than 7 cm or invaded adjacent tissue (T3-T4 of TNM classification). Active surveillance can be proposed to elderly and co-morbid patients with small and/or asymptomatic renal masses.

Adjuvant therapy is not approved for local disease by the European Medicines Agency (EMA), neither are neoadjuvant approaches, which should be restricted to clinical trials.

c. Advanced and metastatic disease

Surgery to reduce tumour size is called cytoreductive nephrectomy and is recommended for good-risk patients with good performance status and no symptom associated with the primary tumour. Tumour resection might be curative if all lesions are excised, otherwise the cytoreductive nephrectomy is considered palliative and systemic treatments are necessary. Additionally to surgery, local radiotherapy can be proposed to relief symptoms associated with bone or brain metastases.

At least 17 systemic drugs with different mechanisms of action are approved in Europe (as of May, 2020) for the treatment of advanced and metastatic ccRCC (Table 4). While cytotoxic chemotherapy still represents the standard of care for the majority of advanced and metastatic cancers, ccRCC is largely chemo-resistant, and no cytotoxic drug is currently recommended.

In the 90s, based on observations of spontaneous regressions of metastases (including brain, bone, liver and pulmonary metastases) following local nephrectomy – on an abscopal fashion – the assumption was made that adaptive immunity might

play an important role in ccRCC malignancy ³². Therefore, cytokine immunotherapies with IFN α and IL-2 were initially tested in the late 1980s and first achieved clinical responses by then.

Table 4. International non-proprietary name (INN), type and year of European first approval of drugs which compose the current therapeutic arsenal for systemic treatment of advanced and metastatic ccRCC.

Drug	Type of therapy	Year of first approval (EMA)
Interleukine-2	Non-specific immunotherapy	1989
Interferon- α	Non-specific immunotherapy	1999
Sorafenib	Targeted therapy antiangiogenic	2006
Sunitinib	Targeted therapy antiangiogenic	2006
Bevacizumab	Targeted therapy antiangiogenic	2007
Temsirolimus	Targeted therapy anti-mTOR	2007
Everolimus	Targeted therapy anti-mTOR	2009
Pazopanib	Targeted therapy antiangiogenic	2010
Axitinib	Targeted therapy antiangiogenic	2011
Cabozantinib	Targeted therapy antiangiogenic	2014
Nivolumab	Immune-checkpoint blocker	2015
Ipilimumab	Immune-checkpoint blocker	2015
Pembrolizumab	Immune-checkpoint blocker	2015
Lenvatinib	Targeted therapy antiangiogenic	2015
Atezolizumab	Immune-checkpoint blocker	2017
Avelumab	Immune-checkpoint blocker	2017
Tivozanib	Targeted therapy antiangiogenic	2017

Subsequently, the improvement of biological knowledge on the disease describing specific VHL-dysfunction guided treatments over anti-angiogenic strategies. Indeed, as VHL-inactivation results in accumulation of HIF1 α , ccRCC tumour cells often over-express pro-angiogenic factors such as VEGF and platelet-derived growth factor (PDGF) ^{33,34}, which explains the increased vascularity that drives these tumours. Hence, anti-angiogenic therapies targeting the VEGF pathway largely outperformed the old-fashioned immunotherapies in the 2000s.

More recently, immune-checkpoint inhibitors used in combination demonstrated clinical superiority over anti-angiogenic therapies in first-line setting ^{35,36}. Since then, these are preferred options for patients with advanced or metastatic ccRCC for whom systemic treatment is required. Which setting depends on the IMDC risk assessment as described in Section IV.a, additionally to personal condition (contraindication to immune-checkpoint blockers, for example) (Figure 9).

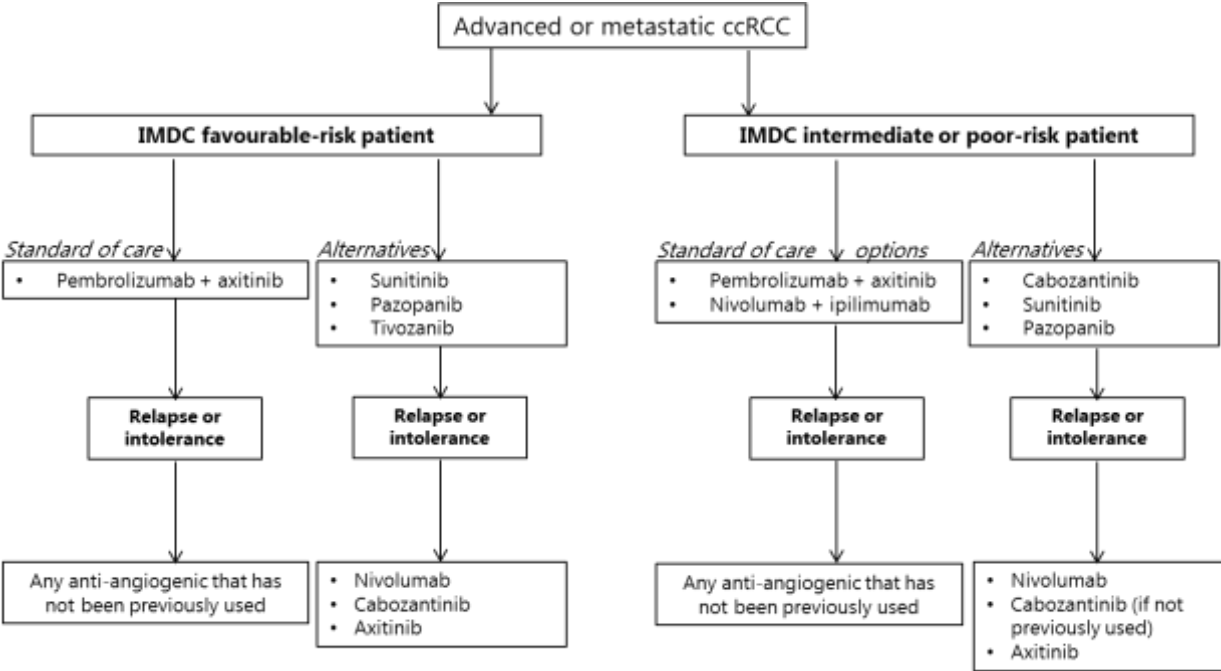


Figure 9. Algorithm for first-line and later-lines systemic treatment of advanced and metastatic ccRCC, according to EAU, ESMO and NCCN Guidelines available in May, 2020.

Although therapeutic alternatives are multiple (Table 4), personalized decision making is currently limited to the IMDC group upon which the patient belongs at the time of diagnosis. No molecular biomarker is validated so far to decipher whether a patient with advanced ccRCC could specifically benefit more from one option compared to one other, perhaps due to (i) lack of robust clinical evidence, (ii) absence of molecular profiling of tumours in phase III pivotal trials that recently led to immune-checkpoint inhibitor approvals, (iii) conflicting data on the predictive values of facultative truncal drivers – namely *PBRM1* and *BAP1* mutations – with existing treatment options, and (iv) the difficulty in re-biopsying patients once they have received anti-angiogenic drugs.

For example, the prospective IMmotion150 trial randomized 305 newly-diagnosed metastatic ccRCC patients to receive atezolizumab (immune-checkpoint blocker anti-PDL1) alone or combined with bevacizumab (anti-angiogenic) or sunitinib (anti-angiogenic)³⁷. Their findings were in favor of a correlation between *PBRM1*-mutation and improved survival following anti-angiogenic treatments compared to atezolizumab monotherapy. In another recent study, *PBRM1* loss was also found to be associated with a less immunogenic microenvironment, even with a resistant phenotype to immune-checkpoint blockers, and by contrast, to a more angiogenic phenotype³⁸, suggesting that these tumours might more benefit from a first line antiangiogenic as monotherapy, than from immune-checkpoint blockers.

On the other hand, the *post-hoc* analysis of the CHECKMATE025 trial revealed a correlation between *PBRM1*-mutation and benefit both in progression-free survival and overall survival (HR [95%CI] = 0.67 [0.47–0.96]; p = 0.03, and 0.65 [0.44–0.96]; p = 0.03 respectively) following nivolumab (immune-checkpoint blocker anti-PD1) compared to sunitinib, in metastatic ccRCC patients previously treated with anti-angiogenics³⁹. Additionally, *Miao et al.* described that patients with metastatic ccRCC

harboring PBRM1 loss-of-function significantly benefited more of immune-checkpoint anti-PD1 therapy than patients with intact PBRM1 (overall survival $p = 0.012$ and $p = 0.0074$ on the validation cohort) independently from the number of previous treatment lines ⁴⁰. However, they could not correlate this finding with a particular immune-microenvironment signature that would be specifically induced by PBRM1 dysfunction; and these results were not comparative with anti-angiogenic administration.

Potential causes of these divergent observations may be related to (i) differences in the patient populations studied, which notably varied on the number and type of previous lines of treatment, (ii) the choice of the comparatives (i.e. randomization with standard-of-care or just observational observation of the impact of PBRM1 mutation on the outcome) and (iii) the retrospective nature of the majority of these studies ⁴¹.

Altogether, these data suggest that molecular targeting in advanced ccRCC is of great interest but evidence-based observations are still limited and conflicting, calling for further investigations.

Part II: SWI/SNF alterations in cancer

I. Epigenetics, chromatin modifiers and SWI/SNF complexes

a. Epigenetics: definition and discovery

The term *epigenetics* comes from the contraction of the Greek $\acute{\epsilon}\pi\iota$ (above) and *genetics*, and designates the study of expression changes of a gene – and the cellular phenotypic characteristics resulting from it – which are transmissible during cell divisions, and which are not being generated by a modification of the DNA sequence of this gene⁴². Epigenetics adapts the phenotype without altering the genotype of the cell. Epigenetic modifications have the characteristics of being (i) reversible and (ii) transmissible to daughter cells during mitosis.

Conrad H. Waddington was presumably the first to describe the concept of epigenetics⁴³. In the 1940s, the British scientist and philosopher uttered the need to establish a link between genotype and phenotype, after observing malformations in flies, which were induced by thermal shocks and notably transmissible to descendants. He formulated the hypothesis of the existence of an additional code of interpretation to the genetic code. Such code would allow the cell to identify itself functionally and morphologically within a complex organism. Thus, from an initial stem cell, differentiated cells could develop (for examples, a muscle cell and a neuronal cell) whose transcriptional landscape will be different despite a strictly identical DNA sequence.

In the 1980s, different teams discovered that one of the DNA bases, the cytosine, can be methylated to 5-methyl-cytosine and that their hyper-methylation, in particular across CpG islands within the promoter region of genes, prevented their transcription by RNA polymerase II^{44,45}. This phenomenon is mediated by enzymes called DNA

methyltransferases (DNMT). This mechanism constitutes an epigenetic mark that is directly affixed onto DNA, but the whole nuclear epigenetic code goes further and implies modifications of the nucleosome around which the DNA is wound.

Indeed, eukaryotic DNA is super-wound around octamers of core histones called nucleosomes which are formed of one histone 3-histone 4 (H3-H4) tetramer and two histone 2A-histone 2B (H2A-H2B) dimers. Each nucleosome supports approximately 146 to 147 base pairs of DNA. Each histone has two tails (N-terminal and C-terminal) and a body, and is enriched in basic amino acids (lysine and arginine). At physiological pH, these basic residues are positively charged, which allows the strong interaction with the DNA phosphate groups (negatively charged). Each residue - mainly lysine and arginine, but not exclusively - of each histone can undergo, depending on cellular needs, modifications by addition or removal of chemical groups (acetyl, methyl, phosphoryl etc), resulting in a 3D conformational change of the chromatin and promoting or preventing local access to DNA on this region.

For example, lysines 9 and 27 of histone H3 (H3K9, H3K27) are associated with repression of the surrounding chromatin when they are tri-methylated, while they are associated with activation of the surrounding chromatin when acetylated. Another example would be the phosphorylation of lysine 139 from histone H2AX (commonly known as γ H2AX) which occurs as soon as the cell detects a DNA double-strand break (DSB). This is followed by a series of molecular responses to resolve the break and restore the initial genotype.

The chemical groups are added by enzymes called "writers" such as histone-acetyltransferases (HAT), histone-methyltransferases (KMT for lysine methyltransferase, PRMT for arginine methyltransferase) etc., and are removed by enzymes called "eraser", such as histone deacetylases (HDAC), histone demethylases

(KDM for lysine, PRDM for arginine) etc (Figure 10). A third group of epigenetic modifying proteins are called the "readers", which recognize, through specific protein domains, the acetyl/methyl/phosphoryl etc. groups, and can modify at this location the interactions between DNA and nucleosome by hydrolysis of ATP. For example, proteins containing a bromodomain recognize acetylated lysines; proteins with chromodomain recognize methylated lysines etc. These are generally part of a multi-protein complex which also contains an ATPase enzyme, catalytic subunit necessary for the remodeling of chromatin.

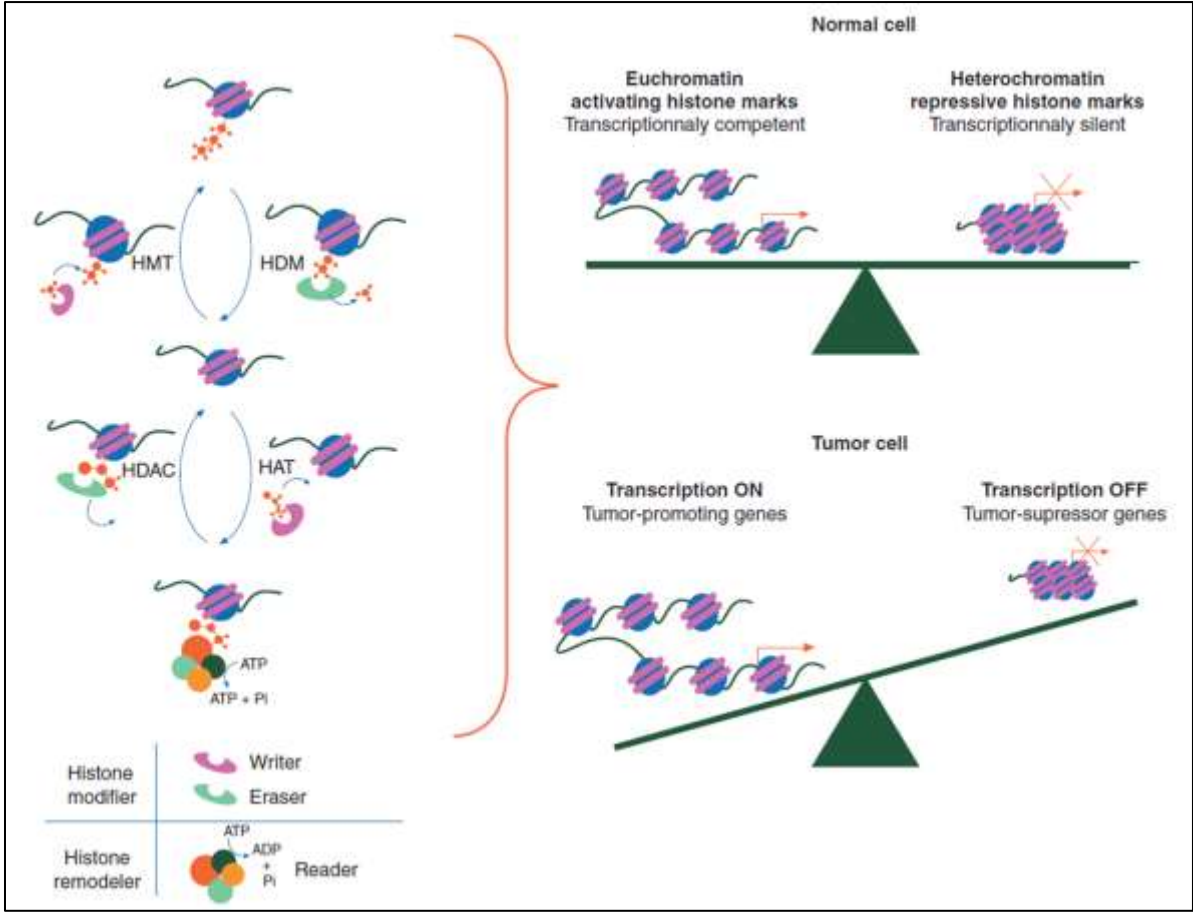


Figure 10. Schematic representation of histone marks and global functional consequences following their alteration and in cancer. Published in *Morel et al.* ⁴⁶.

Therefore, possibilities of modulating (activating or repressing) the expression of one single DNA sequence are almost infinite, at the scale of an organism, a specific tissue but also within a single cell, all along the cell cycle. Indeed, the chromatin is constantly re-arranged to allow transcription, repair of DNA damage, replication etc., and each cell must, during these various actions, maintain its phenotype and its place within the tissue to which it belongs.

b. Epigenetics: implication in carcinogenesis

Functional modifications of the epigenetic code (DNA methylation, methylation / acetylation of histones etc.) have been described almost 40 years ago; although the key role of epigenetics dysfunction in carcinogenesis, and in particular of genes involved in chromatin-remodeling has been suspected about 20 years later^{47,48}.

In 2010, the team of Bert Vogelstein discovered that *ARID1A* was found mutated in almost half of clear cell ovarian cancer samples⁴⁹ - the *ARID1A* gene encodes for a subunit of the SWItch/Sucrose Non-Fermentable (SWI/SNF) chromatin-remodeling complex. Thus, they suggested that *ARID1A*-mutation does not directly contribute to the formation or maintenance of the tumour, but rather involves gene expression changes which themselves contributed to carcinogenesis and maintenance of the tumour.

Since then, thanks to the advent of high-throughput sequencing techniques, mutations in several epigenetic-modifying genes have been identified in many diseases, and in particular in solid malignancies. Indeed, among genes mutated in more than 4% of cases (all cancer types), about 28.3% (13/46) are epigenetic-modifying genes (Table 5). Of course this proportion is underestimated as it does not take account of copy-number alterations and possible epigenetic silencing of epigenetic-modifying genes.

Table 5. Gene names and related mutation frequency in the pooled PanCancer Atlas cohort of TCGA, totaling 10.437 profiled samples from 32 cancer types (last assessed on cbiportal on 20/05/2020). Lines in bold refer to genes encoding an epigenetic-modifying protein. To note, the mutation frequency may not reflect the exact incidence of the mutation within all cancers, as several cancer types are over-represented in the PanCancer Atlas cohort and mutation frequency has not been normalized on the cancer type incidence (for example, 5.4% of samples were glioblastoma while it represents less than 0.02% of all cancers)

N°	Gene	Frequency (%)
1	TP53	36.8%
2	PIK3CA	13.1%
3	LRP1B	12.4%
4	PCLO	10.4%
5	KMT2D	9.3%
6	FAT4	8.9%
7	KMT2C	8.7%
8	PTEN	8.2%
9	ARID1A	7.8%
10	APC	7.6%
11	KRAS	7.3%
12	BRAF	7.1%
13	FAT1	6.7%
14	RELN	6.6%
15	ATRX	6.1%
16	NF1	6.0%
17	ATM	5.3%
18	IDH1	5.3%
19	PRKDC	5.2%
20	MGAM	5.1%
21	LRRK2	5.0%
22	PTPRT	5.0%
23	PTPRD	4.9%
24	PDE4DIP	4.9%
25	ZFHX3	4.9%
26	TRRAP	4.8%
27	RNF213	4.8%
28	KMT2A	4.6%
29	GRIN2A	4.6%
30	CREBBP	4.4%
31	PREX2	4.4%
32	ERBB4	4.3%
33	BRCA2	4.3%
34	ROS1	4.3%
35	FBXW7	4.3%
36	PTPRB	4.3%
37	RB1	4.3%
38	KMT2B	4.3%

39	MKI67	4.2%
40	SPEN	4.2%
41	SETD2	4.1%
42	PBRM1	4.1%
43	MGA	4.1%
44	EP300	4.1%
45	NOTCH1	4.1%
46	CTNNB1	4.0%

Alteration in a gene coding for an epigenetic-modifying protein can be found in all types of cancer. However, there are cancer types among which almost all cases will harbor a dysfunction in at least one of these genes, and therefore, there is a high probability that this alteration has a driver impact on carcinogenesis. This is the case, for example, of rhabdoid tumours, epithelioid sarcomas and ovarian carcinomas of hypercalcemic clear cell subtype⁵⁰⁻⁵³, which all exhibit complete inactivation of SMARCB1 and / or SMARCA2/SMARCA4, three proteins belonging to the SWI/SNF complex. In addition, rhabdoid tumours affect young children with a highly aggressive presentation, and whose mutational landscape is characterized by a very low rate of mutations per megabase, of the order of 100 times less than for melanoma or lung cancer⁵⁰. The loss of a protein belonging to the SWI/SNF remodeling complex, found in 100% of these cases, therefore seems sufficient for the appearance and maintenance of the tumour phenotype. Accordingly, when a mutation is found in 95 to 100% of tumours of a histological type, it seems reasonable to consider it as a major, even sufficient, event for the carcinogenesis process.

II. **SWI/SNF alterations in cancer: description and incidence**

The SWI/SNF complex was first characterized in yeast (*S. cerevisiae*) and described as a large multi-subunit complex required for transcription of multiple genes⁵⁴. Although the general structure of the complex is highly conserved in all eukaryote

species, the mammalian SWI/SNF (mSWI/SNF) has the particularity of being ubiquitously found under three different forms: the canonical brahma-related gene 1/brahma (BRG1/BRM)-associated factor (cBAF) complex, the polybromo-associated BAF (PBAF) complex, and the lately defined non-canonical BAF (ncBAF) complex (Figure 11). Overall, 28 subunits have been described so far to be either essential or facultative part of one, two of all the three forms of mSWI/SNF. For example, PBRM1, ARID2 and BRD7 are found only in the PBAF complex and therefore are mentioned as “PBAF-specific” subunits, while the catalytic subunit SMARCA4 may be found in all forms of mSWI/SNF; however, SMARCA4 is alternately incorporated into one complex with its paralog SMARCA2, thus it is not present in every complex.

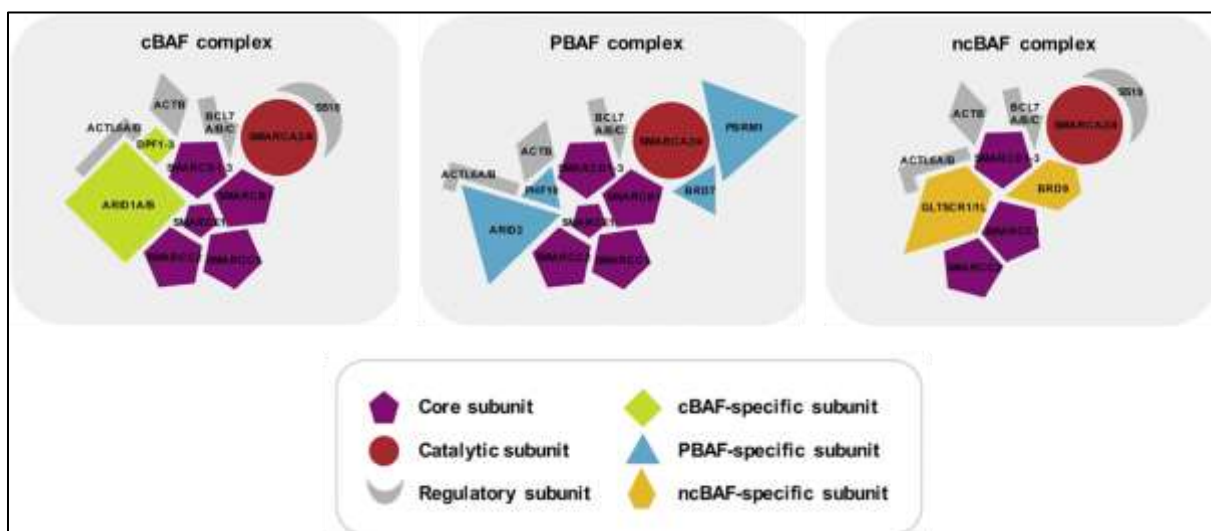


Figure 11. Structure and composition of mSWI/SNF complexes. Each complex is composed of three or five core subunits (SMARCC1, SMARCC2, SMARCD1-3, SMARCB1 and SMARCE1), one ATPase subunit (SMARCA2 or SMARCA4), multiple complex-specific subunits (ARID1A/B and DPF1-3 in cBAF; PBRM1, ARID2, BRD7 and PHF10 in PBAF; GLTSCR1/1L and BRD9 in ncBAF) and several additional regulatory subunits that include ACT6A/B, ACTB, BCL7A/B/C and SS18. Adapted from *Chabanon, Morel and Postel-Vinay*⁵⁵

Large "multi-omic" analysis estimated that SWI/SNF is dysfunctional in 20% of all human cancers^{56,57}. Again, this might be underestimated as new subunits have been discovered since then, although these are marginally found mutated in cancer compared to the ones previously described. The incidence rates vary from almost 0% to almost 100% of cases depending on the cancer type. Interestingly, the profile of altered subunits, and even of altered specific complex, also largely varies from one tumour type to another (Figure 12), suggesting tissue-specific functions of each subunit. For example, *PBRM1* (PBAF-specific) is mutated in about 39% of ccRCCs, while *ARID2* and *BRD7* (also PBAF-specific) are altered in less than 2% of ccRCC cases. On the other hand, *ARID2* is altered in almost 14% of melanomas, whilst *PBRM1* in 5.4% of cases.

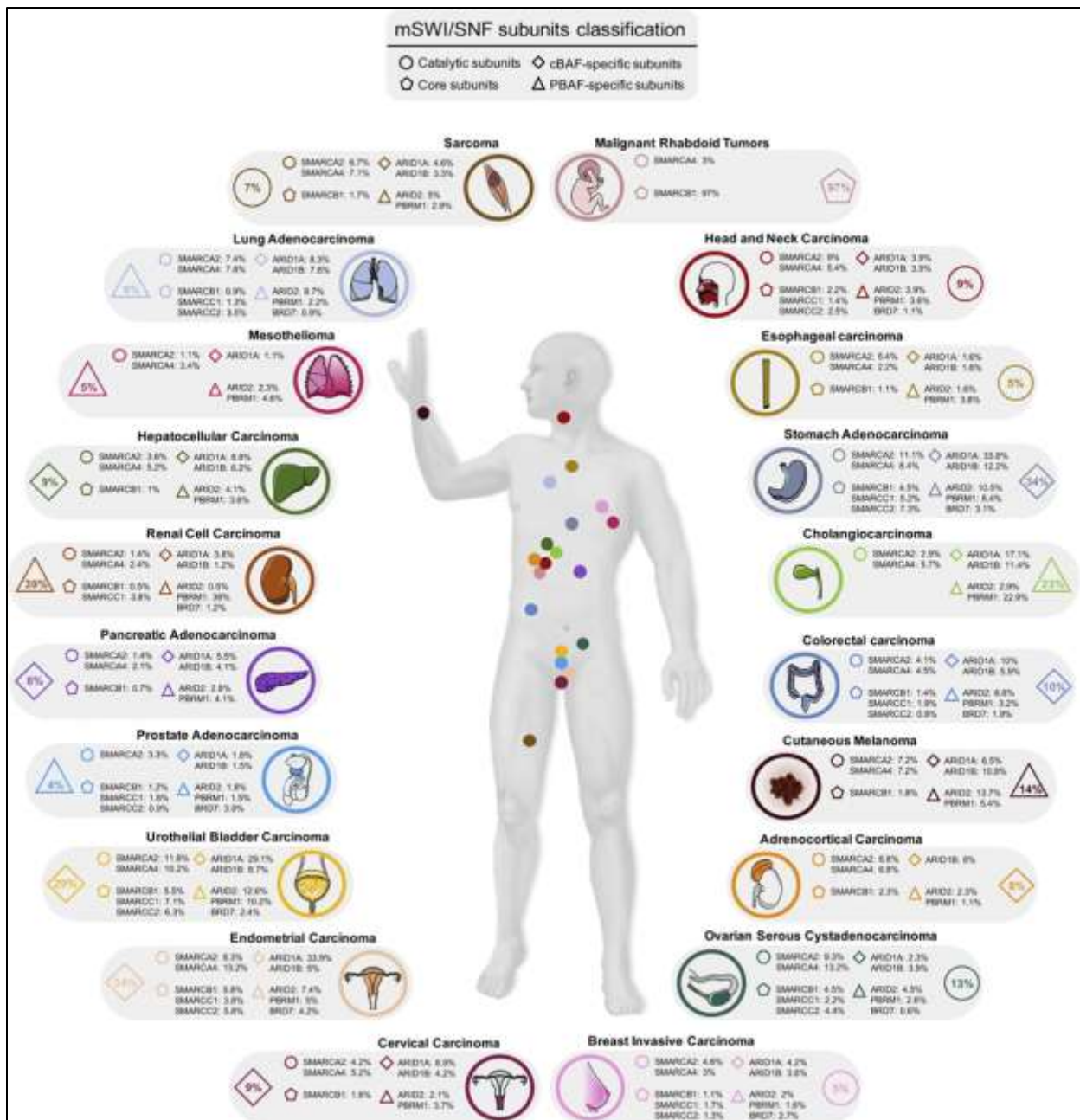


Figure 12. mSWI/SNF subunit mutation rate disparities across human cancers. Published in *Chabanon, Morel and Postel-Vinay* ⁵⁵.

III. **Targeting SWI/SNF alterations in cancer**

In almost all cases, SWI/SNF alteration implies loss-of-function events, even though rare gene amplifications have been described (amplification of *PBRM1* in < 2% of cases of uterine, esophagus and ovarian cancer in the PanCan atlas cohort).

Unlike gain-of-function alterations, which are conceptually straightforward to target using specific inhibitors directed against the overexpressed oncogene or its downstream pathway, loss-of-function mutations are more challenging to approach therapeutically.

a. Concepts of synthetic lethality and epigenetic antagonism

Synthetic lethality was first described in the 1940s in the fruit fly *Drosophyllia*⁵⁸. However, the potential clinical interest of the synthetic lethal approach was only introduced to cancer therapy 50 years later^{59,60}.

Synthetic lethality defines a relationship between two proteins, where the loss of either protein is compatible with cell survival – and perhaps cancer initiation or evolution – while the loss of both proteins leads to cell death. In case of cancer therapy, protein 1 would be specifically loss in tumour cells as part of the abnormal tumour landscape; and protein 2 would be inhibited using a pharmacological inhibitor (Figure 13). Theoretically, normal cells should be proficient for protein 1, and therefore, pharmacological inhibition of protein 2 should not affect their viability.

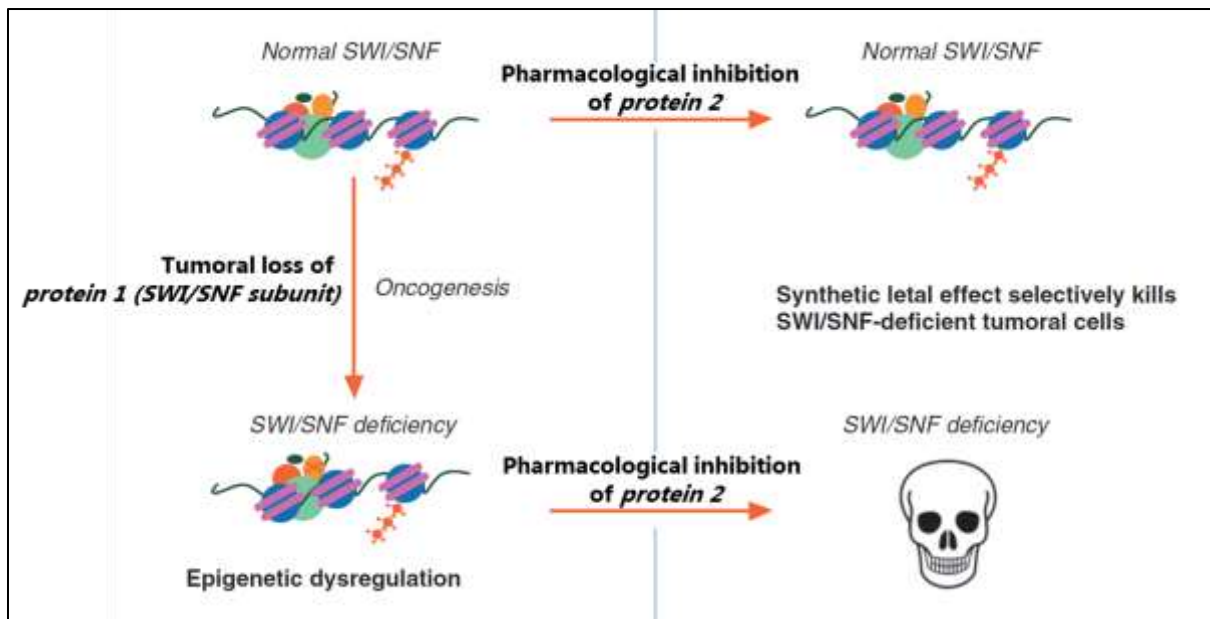


Figure 13. Mechanism-based approach for targeting loss-of-function mutation in human cancer. Loss of fully-functional SWI/SNF represents an epigenetic vulnerability specific to tumour cells that can be therapeutically exploited while preserving healthy tissue. Adapted from Morel et al. 46.

Conceptually, synthetic lethality can engage any type of synthetic lethal interaction which may or may not involve two proteins of similar functions (for example, DNA repair proteins), and which may or may not involve proteins related to epigenetic modulation. However, a particular synthetic lethal situation is sometimes called *epigenetic antagonism*; in that case, both proteins involved in the synthetic lethal relationship physiologically serve antagonistic roles through epigenetic modulation, and both proteins are necessary to maintain a steady epigenetic cellular state. Inhibition of both proteins often leads to cell death.

b. Tumour vulnerability linked to SWI/SNF deficiency

Facing the obvious role of SWI/SNF alterations in carcinogenesis and cancer progression, numerous research teams intended to specifically target SWI/SNF subunits' loss-of-functions. So far, four subunits defects of the SWI/SNF complex exhibited *in vitro* +/- *in vivo* sensitivity to exogenous inhibition of potential synthetic lethal partner, three of which being currently under clinical evaluation (Table 6).

Table 6. Synthetic lethal interactions involving SWI/SNF loss-of-functions that have been described in preclinical models, with the level of evidence (+ if a single peer-reviewed publication reported the interaction; ++ if 2 publications; +++ if at least 3 publications reported the interaction). References of preclinical work and NCT numbers of ongoing clinical trials are detailed in *Chabanon, Morel and Postel-Vinay*⁵⁵.

SWI/SNF dysfunction	Associated vulnerability	Histology	Preclinical evidence	Clinical trial ongoing
SMARCB1 deficiency	EZH2	Rhabdoid tumour	+++	Yes
		Lymphoma	No	Yes
		Non-Hodgkin lymphoma	No	Yes
	BRD9	Rhabdoid tumour	++	No
	MDM2/4	Rhabdoid tumour	+	No
	UBE2C	Renal medullary carcinoma	+	No
	Autophagy	Rhabdoid tumour	+	No
	UPP	Rhabdoid tumour	+	No
	HDAC	Rhabdoid tumour	+	No
PARP	Urothelial cancer with DDR defects	No	Yes	
SMARCA4 deficiency	EZH2	Lung cancer	+++	No
		Non-Hodgkin lymphoma	No	Yes
	SMARCA2	Lung cancer	+++	No
	MAX	Lung cancer	+	No
	CDK4/6	Lung cancer	+	No
		Ovarian cancer	+	No
	AURKA	Lung cancer	+	No
	OxPHOS	Lung cancer	+	No
	RTKs	Ovarian cancer	+	No
	PARP	Cervical carcinoma	+	Yes
ATR	Gynecological cancer	No	Yes	
ARID1A deficiency	EZH2	Ovarian cancer	++	No
	ARID1B	Ovarian cancer	++	No
		Colorectal cancer	+	No
		Triple-negatif breast cancer	+	No
	PARP	Solid tumours with DDR defects	No	Yes
		Biliary tract cancer with DDR defects	No	Yes
		Colorectal cancer	+	No
		Triple-negatif breast cancer	+	No
	ATR	Gynecological cancer with DDR defects	No	Yes
		Solid tumours with DDR defects	No	Yes
	HDAC6	Ovarian cancer	+	No
		Ovarian cancer	+	No
	PI3K/AKT	Gastric cancer	+	No
Solid tumours with DDR		No	Yes	

		defects		
	RTKs	Ovarian cancer	+	Yes
	AURKA	Colorectal cancer	+	No
	GCL	Ovarian cancer	+	No
PBRM1 deficiency	EZH2	ccRCC	+	No

Of note, the epigenetic antagonism described between these SWI/SNF subunits and EZH2 inhibition was first revealed in *Drosophila* mutant models⁶¹. It was further evidenced in SWI/SNF-deficient human tumour models, including in rhabdoid tumours which are largely driven by the loss of SMARCB1. These studies revealed that SMARCB1 deficiency led to EZH2 overall hyperexpression and that pharmacological inhibition of EZH2 using tazemetostat (potent first-in-class EZH2 inhibitor) induced dramatic tumour shrinkage.

Remarkably, the first-in-human phase I clinical trial that evaluated the safety of tazemetostat in patients with relapsed or refractory B-cell non-Hodgkin lymphoma and advanced solid tumours (including but not restricted to SWI/SNF-deficient tumours) showed clinical responses (including complete responses) in eight (38%) of 21 patients with B-cell non-Hodgkin lymphoma and in two (5%) of 43 patients with solid tumours⁶². No response was observed in patients whose tumour was not mutated for *SMARCB1* neither for *SMARCA4*. This remarkable clinical efficacy recently led to the accelerated approval by the U.S. Food and Drug Administration of tazemetostat for patients over 16 who present a metastatic or locally-advanced unresectable epithelioid sarcoma, a rare soft tissue sarcoma which lacks SMARCB1 expression in more than 90% of cases^{63,64}. Tazemetostat is not yet approved by European authorities.

The epigenetic antagonism described in 2015 between PBRM1 loss and EZH2 inhibition by *Kim et al.* was based on an *in vitro* observation on three non-isogenic

PBRM1-mutant ccRCC cell lines of which cell growth was compared to four non-isogenic non-ccRCC SWI/SNF-wild type cell lines⁶⁵. This epigenetic antagonism was neither further validated in a more recent study⁶⁶ nor in the clinic.

We therefore decided to focus my PhD on the search of synthetic lethal partners with *PBRM1* deficiency in ccRCC, as no robust synthetic lethality had been described with this subunit.

Part III: PBRM1

I. Genetic background

PBRM1 (*Polybromo 1*, aka *PB1* or *BAF180*) is a long gene composed of 140,566 DNA bases located on the short arm of the chromosome 3, and more precisely in 3p21.1 (Figure 14, top). The gene encompasses 30 exons, and 21 transcript variants of mRNA have been described to date, 16 of which putatively encode for a functional protein isoform

(<https://www.ncbi.nlm.nih.gov/IEB/Research/Acembly/av.cgi?db=human&c=Gene&l=PBRM1>).

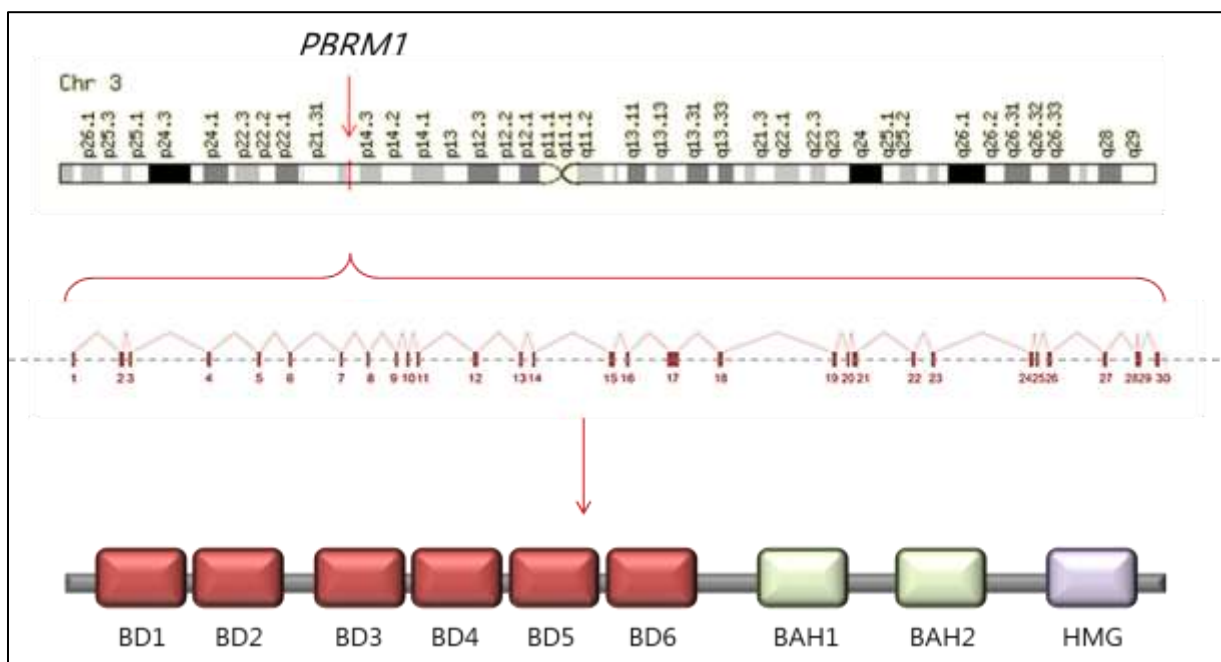


Figure 14. PBRM1 genomic and protein characteristics. Up: cytogenetic bands of human chromosome 3 with genomic location of the PBRM1 locus indicated in red. Medium: detail of the positions of the 30 exons within the gene. Down: detail of positions of the specific domains within the PBRM1 full protein.

The longest isoform of the protein (isoform 5, NCBI reference sequence NP_001337003.1) is 1,618 amino acids long, has a molecular mass of approximately 193 kDa and contains six tandem bromodomains (BD1-6), known to recognize acetylated lysine residues, two bromo-adjacent domains (BAH1-2) that may function as a transcription regulatory part, and a high-mobility group (HMG) box that tethers PBRM1 onto the DNA (Figure 14, down). It is found ubiquitously in all human cells, including in embryonic cells.

PBRM1 different bromodomains display a distinct pattern of affinity for specific acetylated histone mark peptides^{67,68}. The strongest binding is observed with BD2, which preferentially recognizes acetylated lysine 14 of histone H3 (H3K14ac) – a histone mark that is implicated in DNA repair and active transcription among other functions^{67,69–73}. However, BD2, BD4 and BD5 have been shown to collaborate to strongly bind H3K14ac and a modification in a neighboring BD may modulate the overall profile of the PBRM1-chromatin interaction^{70,71}.

Beyond ccRCC, tumour types known to frequently harbor deep loss of function of PBRM1 include chordoma (up to 60% of cases)⁷⁴, intrahepatic cholangiocarcinoma (up to 35% of cases)^{75,76}, mesothelioma (up to 20% of cases)⁷⁷, cutaneous squamous cell carcinoma (up to 16% of cases) (cbioportal.org) and endometrial carcinoma (up to 12% of cases) (cbioportal.org).

II. **Protein roles**

The mSWI/SNF complexes contain several protein domains that collectively aim at localizing their ATP-dependant chromatin remodeling functions to specific regions over the genome⁷⁸. In particular, the PBAF complex contains at least (i) eight bromodomains (six on the PBRM1 subunit, one on BRD7, one on either SMARCA2 or SMARCA4), (ii) one to four PHD finger proteins (PHF10, DPF1, DPF2, either DPF3a or DPF3b), (iii) two chromodomains (SMARCC1, SMARCC2), (iv) between seven and nine

other DNA-binding domains that can recognize specific DNA architectural features such as cruciform DNA (HMG domains)⁷⁹, AT-rich sequences (ARID domains) etc.⁷⁸. Among these domains, nine are present on PBRM1, which suggests that PBRM1 has a role in guiding locus recognition by the complex. Therefore, in the absence of PBRM1, the affinity of SWI/SNF complexes for specific genomic regions might be modified, with functional consequences on multiple cellular activities.

a. **DNA repair**

The role of PBRM1 in DNA repair has been first introduced with its yeast homologue, RSC, more than 15 years ago. It was thereupon described that UV exposure induced local H2AX phosphorylation on serine 139 (γ H2AX) and subsequent H3K14 acetylation on adjacent nucleosomes, which acted as a "docking site" to anchor RSC (yeast) / SWI/SNF (mammals) onto the nucleosome and facilitate DNA repair^{69,72,73,80-83}.

It was further described that the specific loss of PBRM1 subunit was associated with hypersensitivity to DNA damage, in particular at early time-points after DNA DSBs^{84,85}. *Brownlee et al.* showed that PBRM1 defect led to increased frequency of chromosome aberrations and global increased chromosomal instability following DNA damage⁸⁴. Additionally, *Kakarougkas et al.* described that PBRM1 was phosphorylated at sites of DNA DSBs by Ataxia Telangiectasia Mutated (ATM), and that this step was critical to ensure correct DNA damage signalization and processing⁸⁵.

Another described role of PBRM1 in the process of DNA repair consists of repressing gene transcription near a DNA DSB during interphase, which is a process required to lower the risk of genome alteration⁸⁶.

Finally, when a DNA DSB occurs during replication, PBRM1 has been shown to be involved in the repriming of the stalled replication fork after restoration of the DNA damage⁸⁷.

b. Transcription

The histone mark H3K14ac – recognized by PBRM1 – is also particularly enriched in transcriptional start sites (TSS) of genes, and therefore its presence is highly predictive of active gene transcription which could require PBRM1 to facilitate DNA access to the transcriptional machinery^{88,89}. Next-generation RNA sequencing of ccRCC samples and isogenic cellular models indeed showed differences in the expression profiles of PBRM1-deficient cells compared to PBRM1-proficient cells^{90,91}. Such method identified multiple cellular functions that are modified by the loss of PBRM1, including cell adhesion, cholesterol metabolism (responsible for the “clear cell” phenotype observed in pathology), cellular homeostasis, cell cycle progression, stress response following hypoxia or DNA damage and apoptosis.

Although several studies consistently revealed such alterations following PBRM1 dysfunction, they never clearly depicted whether these were resulting from a transcriptional dysfunction or an independent mechanism.

c. Mitosis and cytoskeleton

Consistently with what was initially described in yeast, PBRM1 has been found at kinetochores of chromosomes during mitosis (mostly during prophase) and participate in the maintenance of centromeric chromatin structures during chromosomal segregation^{84,92}.

Recently, it was observed that PBRM1 could directly recognize and bind α -tubulin trimethylated on lysine 40, which is an epigenetic mark on tubulin localized to the mitotic spindle and spindle poles during mitosis⁹³. Such ability suggests a role of

PBAF not only for chromatin-remodeling, but also possibly for cellular missions involving microtubules, including proper mitotic spindle segregation.

III. **High-potential drug candidates for targeting PBRM1-defects**

To summarize, PBRM1 has known roles in multiple cellular processes requiring chromatin-remodeling, including DNA repair, mitosis, transcription and replication. All of these processes can be efficiently targeted with already approved drugs or drugs currently under clinical development (Figure 15).

For example, we could hypothesize that PBRM1 loss-induced epigenetic dysregulation that may be efficiently targeted using epigenetic-modifying drugs⁹⁴. Other SWI/SNF subunits deficiencies were indeed previously shown to be associated with increased sensitivity to EZH2 inhibitors, bromodomain and extraterminal motif protein (BET) inhibitors⁹⁵ or HDAC inhibitors (Table 6)^{46,55}. Importantly, the sensitivity to EZH2 inhibition concerns various subunit deficiencies (SMARCB1, ARID1A, SMARCA4), although data remain divergent regarding PBRM1^{65,66}.

Similarly, mitotic defects could be targeted using spindle toxins that inhibit the polymerization of microtubules (such as vinca alkaloid drugs, e.g. vincristine, vinblastine, vinorelbin etc.) or their depolymerization (such as taxane drugs, e.g. paclitaxel, docetaxel etc); inhibitors of topoisomerase I (such as topotecan, irinotecan etc) or topoisomerase II (etoposide, anthracyclines etc) act by blocking the relaxing of DNA supercoiling during interphase, and therefore generate DNA DSBs. Others agents such as platinum salts (cisplatin, carboplatin etc), nitrogen mustards (cyclophosphamide, ifosfamide, melphalan, bendamustine etc), nitrosoureas (carmustine, lomustine etc), alkyl sulfonates (busulfan), triazine (dacarbazine,

temozolomide) might be toxic for PBRM1-defective cells with reduced DNA repair capacities.

However, no drug is registered to date to specifically target PBRM1-defective tumours. We therefore aimed at identifying such drug during my PhD.

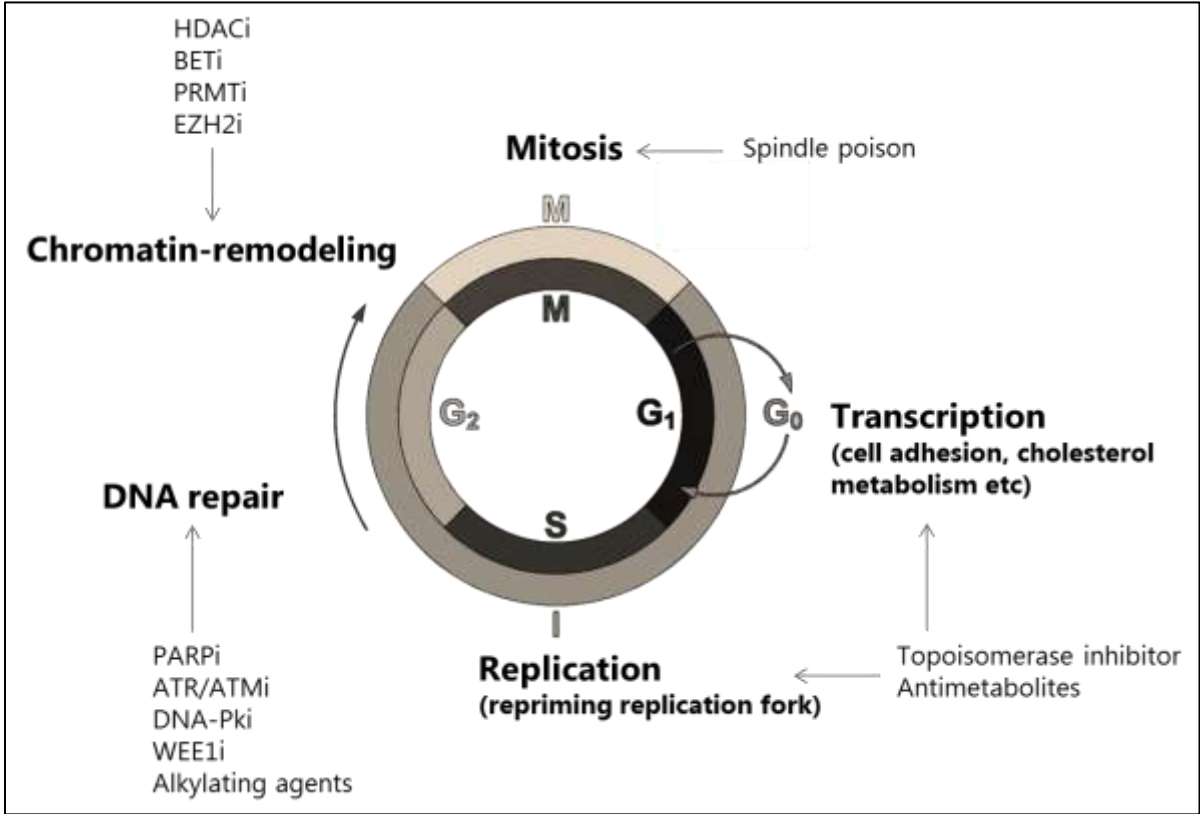


Figure 15. Known implications of PBRM1 within the cell cycle and other cellular functions and examples of potential drug-family candidates that could elicit cytotoxicity in a context of PBRM1 deficiency.

Part IV: Objectives, summation of the rationale to target PBRM1-deficiency in advanced ccRCC

The main objective of this PhD work was to identify therapeutic approach(es) that could selectively target the deficiency in PBRM1 for patients suffering from advanced or metastatic ccRCC and whom could not expect to be cured with surgery or other local treatment. This relies on:

- *PBRM1* is the second most altered gene in ccRCC after *VHL*, and complete loss of its protein expression drives almost half of ccRCCs
- PBRM1 loss is an early event in the course of ccRCC, therefore its deficiency is often clonal (present in all tumour cells). Consequently, the risk shall be very low to develop a resistance to treatment that would be caused by the selection and expansion of a subclone which would not harbor PBRM1 deficiency
- Germline mutations in *PBRM1* are exceptional ⁹⁶, therefore it is expected that healthy cells are PBRM1-proficient and should not be affected by a treatment targeting PBRM1-deficiency (tumour-specific)
- PBRM1 status is easy and cheap to assess in routine using IHC, PCR or targeted sequencing on tumour sample
- The tumour phenotype associated with PBRM1 deficiency (DNA repair defects, mitosis defects etc) is highly "actionable", meaning that anticancer drugs already approved are high-potential candidates
- Loss-of-function alterations in tumour suppressor genes have already been successfully targeted in the past (PARP inhibitors approved in BRCA-deficient ovarian cancer) using synthetic lethal approaches

Secondary objectives of the study were (1) to characterize the main mechanistic processes underlying the synthetic lethal relationships that we discovered, and (2) to explore the cell-type independency potential of these findings and consider generalizing to all *PBRM1*-mutated cancers.

Chapter II: Materials and Methods

I. Tumour cell lines

HAP1 PBRM1-WT and PBRM1-KO cell lines were purchased from Horizon Discovery. U2OS, H1299, RCC-MF and RCC-FG2 parental cell lines were purchased from ATCC. 786-O and A498 parental cells were kindly provided by Dr. Sophie Le Gad's laboratory. The generation of PBRM1-KO secondary mutant cell lines was performed on 786-O, A498, U2OS and H1299 cell lines (Table 7) using CRISPR-Cas9 site directed mutagenesis, as described below. U2OS, 786-O and A498 and derived cell lines were grown in high glucose-Dulbecco's Modified Eagle Medium (DMEM) supplemented with 10% fetal bovine serum (FBS). RCC-MF were maintained in Roswell Park Memorial Institute-1640 (RPMI) medium supplemented with 4.5 g/L glucose, 2 mM L-glutamine and 10% FBS. RCC-FG2 were cultured in RPMI supplemented with 2mM L-glutamine and 10% FBS. HAP1 cells were cultured in Iscove's Modified Dulbecco's Medium (IMDM) supplemented with 10% FBS. All cells were grown at 37°C in 5% CO₂. MycoAlert™ detection kit (Lonza) was used for mycoplasma detection for all cell lines. All cell lines were short tandem repeat typed (STR typed) using StemElite ID (Promega) to confirm identity prior to the study.

Table 7. List of the cell lines used for this work and details on whether they were utterly obtained or genetically modified at the lab

Cell line	Histology	Purchased /retrieved	Generated for the study
HAP1 WT (parental)	CML	X	
HAP1 PBRM1-KO	CML	X	
HAP1 ARID2-KO	CML	X	
786-0 WT (parental)	ccRCC	X	
786-0 PBRM1-KO	ccRCC		X
786-0 PBRM1-KO PBRM1-induced	ccRCC		X
786-0 WT H2B-mCherry	ccRCC		X
786-0 PBRM1-KO H2B-mCherry	ccRCC		X
RCC-FG2	ccRCC	X	
RCC-MF	ccRCC	X	
A498 WT (parental)	ccRCC	X	
A498 PBRM1-KO	ccRCC		X
U2OS WT (parental)	osteosarcoma	X	
U2OS PBRM1-KO	osteosarcoma		X
H1299 WT (parental)	NSCLC	X	
H1299 PBRM1-KO	NSCLC		X

786-O cells were transduced by a lentiviral vector to stably express H2B-mCherry. Lentiviral particles were produced in 293FT cells using the following plasmids: pLenti6-H2B-mCherry (Addgene, ref 89766), psPAX2 (Addgene, ref 12260) and pMD2.G (Addgene, ref 12259). Successfully transduced H2B-mCherry expressing 786-O cells were selected in the presence of blasticidin. *PBRM1*-KO was performed in U2OS, 786-O, 786-O H2B-mCherry, A498 and H1299 cell lines using a CRISPR/Cas9-based gene editing approach. A guide-RNA (TTCATCCTTATAGTCTCGGA) was designed to generate a frameshift deletion in exon 3 of the *Baf180* gene (encoding PBRM1). PBRM1 KO in the resulting cell lines (U2OS PBRM1-KO, 786-O PBRM1-KO, 786-O H2B-mCherry PBRM1-KO, A498 PBRM1-KO and H1299 PBRM1-KO) was monitored by western blot analysis and sequencing after genomic amplification by PCR. PBRM1 shRNA-based silencing was performed in U2OS as previously described (SR Hopkins et al., *DNA repair*, 2016). PBRM1 rescue was performed in 786-O PBRM1-

KO cell line using TetO-FUW-PBRM1-pgk-puro (Addgene, ref 85746) and pLenti CMV rtTA3 (Addgene, ref 26429) plasmids.

II. **Probes**

a. **Drugs**

The PARPi olaparib (AZD-2281, Astra Zeneca), rucaparib (PF-01367338, Clovis Oncology), talazoparib (BMN-673, Pfizer), and veliparib (ABT-888, Abbvie), the ATRi berzosertib (VE-822, Merck), VE-821 (Merck), and ceralasertib (AZD6738, Astra Zeneca), as well as the BETi JQ1 were purchased from Selleck Chemicals. The PARPi niraparib (MK-4827, Tesaro) was obtained from MedChemExpress. Mitomycin C (MMC) and 5,6-dichlorobenzimidazole 1- β -D-ribofuranoside (DRB) were purchased from Sigma-Aldrich.

Inhibitor stock solutions were prepared from powder, diluted in 100% DMSO and stored at -80°C in aliquots of stock solutions at 50 mM or 100 mM when feasible, except for MMC which were diluted in RNase-free water and stored at 4°C for a maximum of 8 days, as recommended in the Good Practice of database of stabilities and compatibilities of injectable drugs (<https://www.stabilis.org/>).

b. **Antibodies**

Primary antibodies that were used for this work are listed in Table 8. For western blotting (WB), horseradish peroxidase (HRP)-conjugated secondary antibodies were purchased from Sigma Aldrich and diluted in milk to 1:10000. For immunofluorescence (IF), Alexa Fluor® (AF)-555-conjugated (A21422) and AF-488-conjugated (A11034) secondary antibodies were purchased from ThermoFisher and diluted to 1:1000.

Table 8. List of primary antibodies that were used for this work for WB or IF

Target	Host	Company	Ref
PBRM1	Rabbit	Bethyl	A301-591A-M
Actin	Mouse	Sigma Aldrich	A1978
ARID2	Mouse	Santa Cruz	sc-166117
ARID1A	Mouse	Santa Cruz	sc-32761
ARID1B	Mouse	Abcam	ab57461
BRD7	Mouse	Santa Cruz	sc-376180
BRD7	Rabbit	Cell Signaling	15125S
SMARCA4	Mouse	Santa Cruz	sc-17796
SMARCA2	Rabbit	Abcam	ab15597
SMARCC2	Rabbit	Cell Signaling	12760S
SMARCC1	Rabbit	Cell Signaling	11956S
SMARCD1	Mouse	Santa Cruz	sc-135843
SMARCB1	Mouse	Santa Cruz	sc-166165
PARP1	Rabbit	Abcam	ab191217
BRCA1	Rabbit	Cell Signaling	9010S
BRCA2	Mouse	Calbiochem	OP95M
RAD51	Rabbit	Cell Signaling	8875S
RAD51	Rabbit	Santa Cruz	sc-8349
pATM (S1981)	Rabbit	Cell Signaling	5883S
ATM	Rabbit	Cell Signaling	2873S
pATR (S428)	Rabbit	Cell Signaling	2853S
ATR	Rabbit	Cell Signaling	2790S
pCHK1 (S345)	Rabbit	Cell Signaling	2341P
CHK1	Mouse	Santa Cruz	sc-8408
SETX	Rabbit	Bethyl	A301-104A
pH2AX	Mouse	Millipore	05-636
α -tubulin (IF)	Mouse	Abcam	ab7291
S9.6	Mouse	Kerafast	ENH001
ssDNA	Mouse	Millipore	MAB3868

c. **Other chemicals**

All chemicals were purchased from Sigma Aldrich except for probes for reverse transcription quantitative PCR (RT-qPCR) which were obtained from ThermoFisher (Table 9).

Table 9. List of other chemicals, including RT-qPCR primers

Probe	Company
BRCA1 PCR primer (Hs01556193_m1)	ThermoFisher
BRCA2 PCR primer (Hs00609073_m1)	ThermoFisher
RAD51 PCR primer (Hs00947967_m1)	ThermoFisher
PicoGreen Quant-iT dsDNA	ThermoFisher
Hoechst 33342	ThermoFisher
5,6-Dichlorobenzimidazole 1- β -D-ribofuranoside (DRB)	Sigma Aldrich
Iodo-deoxyuridine (IdU)	Sigma Aldrich
5-Chloro-2'-deoxyuridine (CldU)	Sigma Aldrich
Dimethyl sulfoxide (DMSO)	Sigma Aldrich

III. **Protocols**

a. **Preliminary screening**

HAP1 cells growing in log phase were seeded in 384 well-plates at a density of 250 cells per well. The cells were dispensed in 25 μ L of tissue culture media using a Thermo Fisher Multi-Drop Combi. Cells were initially plated at a density to ensure that each cell line was in growth phase by the end of the five-day treatment, similar to Garnett et al., 2012 (PMID: 22460902). 24 hours after seeding, 25 μ l of media containing the small molecule inhibitor library was added to the cells using a Hamilton Microlab Star liquid handling platform to make a final concentration of 0.5, 1, 5, 10, 50, 100, 500, 1000 nM. Each plate was performed in triplicate. Two compound libraries were used in this study. The compounds used, which selectively target the DNA-repair pathway, were purchased as custom plates from Selleckchem. Cells were then continuously cultured in the presence of the small molecule inhibitors for a period of five days. Cell viability was estimated by removing the media and adding 20 μ l (diluted 1 in 4 in PBS) of Cell-Titer Glo (Promega) and after a 10-minute incubation at RT, Cell-Titer Glo generated luminescence was captured using a Victor X-Light plate reader. Luminescence values from each well were normalized to the median of signals from wells exposed to DMSO only (no small molecule inhibitor) to

generate surviving fractions (SF). Surviving fractions were then used to plot dose-response survival curves, generated using 3-parameter logistic regression analysis via the drc R-package (Ritz and Streibig, 2005 Bioassay Analysis using R. J Statist Software 12, 1-22). Using drc, Area Under the Curve (AUC) values were calculated from dose-response survival curves.

b. Proliferation assays

Cells were seeded in quadruplicates in 96-well plates for IC50 assessment or 6-well plates for colony-forming assays (CFA). After 24 hours, cells were treated and continuously exposed to the drug during 7 days (IC50) or at least 10 days (CFA). For IC50, cells were lysed and assessed for viability using CellTiterGlo® from Promega (ref G7571) following the manufacturer's instructions and quantified using a VICTOR multilabel plate reader from PerkinElmer. Surviving fraction was calculated as follow: mean of luminescence from drug-treated samples / mean of luminescence from vehicle-treated samples. Figures were made using GraphPad Prism V8.0.2 software. For combination treatment, synergy analysis was computed in 3 steps using R-3.6 package BIGL-1.4.1. First, marginal curves were modeled with non-linear least squares estimation procedure using Levenberg-Marquardt algorithm. Second, expected effects were compute according to a Generalized Loewe null model using variance heterogeneity estimator. Finally, maxR statistical test was used to compare the expected response with the observed effect. These steps are described in Van der Borght et al. (Van der Borght K, Tourny A, Bagdziunas R, et al. BIGL: Biochemically Intuitive Generalized Loewe null model for prediction of the expected combined effect compatible with partial agonism and antagonism. Sci Rep. 2017;7(1):17935. Published 2017 Dec 20. doi:10.1038/s41598-017-18068-5).

For CFA, cells were washed once with PBS and then fixed with crystal violet 0.5% in methanol during 20 minutes at room temperature (RT). Cells were washed several

times in clean water and let to air dry. Colony number was manually evaluated and surviving fraction was calculated as mean of number of colonies of at least 50 cells in drug-treated wells / mean of number of colonies of at least 50 cells in vehicle-treated wells.

Spheroids were grown by seeding 5000 cells per well in round-bottomed inertGrade 96-well microplates from Sigma-Aldrich (ref BR781900-40EA). The plates were centrifuged for 15 minutes at 600 x g. The day after (J0), spheroids were treated with the drug or DMSO. Pictures were taken after indicated times using an EVOS Cell Imaging System (ThermoFisher) at 4X magnification. Spheroid areas were estimated using ImageJ software. All experiments were performed at least 3 times.

c. Western blot and co-immunoprecipitation

Cells were lysed using the following lysis buffer: 50 mM Tris-HCl, 137 mM NaCl, 10% glycerol, 1% NP40 and 1 anti-protease tablet (ref 11836153001) for 10 mL of buffer. For IP, 300 µg of proteins were incubated with 50 µL of Dynabeads protein G (10004A) purchased from ThermoFisher Scientific and 0.25 µg SMARCC2 antibody or rabbit polyclonal IgG isotype (2729S) O/N at 4°C on a rotating wheel. Non-IP and IP fractions were collected using the lysis buffer. Considering the blotting part, primary antibodies were used at a 1:1000 dilution, except for b-actin (1:5000) and pATM, pATR and pChk1 (1:500) (see Antibodies Table 8 for references). HRP-conjugated secondary antibodies anti-mouse or anti-rabbit were obtained from ThermoFisher Scientific and were used at a 1:10000 dilution.

d. Immunofluorescence and image analysis

For quantification of γ H2AX foci and RPA2 foci and micronuclei cells were seeded in 96W microplates from Greiner Bio-One (ref 655090) and treated with indicated drugs or irradiated using the X-RAD320 biological irradiator. Cells were then fixed in 4%

paraformaldehyde (PFA) for 20 minutes at RT, washed twice with PBS, and permeabilized with 0.2% Triton X-100 in PBS for 10 min. Following labeling and automatic quantification steps were performed as described in *Chabanon et al.*⁹⁷.

e. **Time-lapse microscopy**

Asynchronously growing 786-0 H2B-mCherry cells were seeded in immunofluorescence-adapted 4-well slides from Ibidi (ref 80426). Once attached to the slides, cells were incubated with 2mM thymidine (Sigma-Aldrich, ref T9250) for 18 hours, washed three times with PBS, released into fresh media for 8 hours, incubated with 2mM thymidine again for 16 hours to synchronize into G1/early S phase. After the second blockade, cells were washed three times in PBS, then released into pre-chilled media containing 10 μ M of olaparib or DMSO. After 6 hours, pictures were taken every 15 minutes for 48 hours, using a Leica HR-SP8 confocal microscope in the mCherry channel, at 40X magnification. Four fields per condition were observed by two independent readers. The experiment was repeated 4 times.

f. **RT-qPCR**

RNA was extracted using the RNeasy mini kit (ref 74104, Qiagen), quantified using NanoDrop™ 2000 spectrophotometer (ThermoFisher Scientific) and diluted to equal concentrations across all samples. Reverse transcription was performed using a Transcriptor First Strand cDNA Synthesis Kit (ref 4896866001, Roche) or SuperScript VILO cDNA Synthesis Kit (ref 11754050, ThermoFisher Scientific), following the manufacturers' protocol. qPCRs were performed using SYBR™ Select Master Mix PCR system (ThermoFisher Scientific), and samples were analyzed using the Applied Biosystems® ViiA7 or QuantStudio™ 6 Flex real-time PCR systems. Results were normalized to GAPDH expression.

g. **DNA combing**

Cells were grown in 100 mm dishes with 10 μ M of olaparib during 48 hours or DMSO in order to reach 70% confluence at the time of harvesting. For replication fork labelling, cells received pre-warmed medium containing 100 μ M CldU and were incubated at 37°C, 5% CO₂ for 30 minutes. Cells were then rinsed 3 times with pre-chilled PBS and incubated with 100 μ M IdU for 30 minutes. Cells were then collected in cold PBS, counted and adjusted to 50.000 cells per 50 μ L PBS on ice. The plugs were generated by adding 50 μ L of pre-warmed 1% low-melting point agarose to the 50 μ L cells; the resulting 100 μ L mix were cautiously homogenized and quickly transferred into a casting mold, let to solidify for 1 hour at 4°C. Following steps are described in *M. Bialic et al. DNA replication: Methods in molecular biology vol.1300 DOI 10.1007/978-1-4939-2596-4_4*. For the analysis, initiation, termination and cluster patterns of origins of replication were considered to measure fork velocity.

h. **Proteomic and transcriptomic analyses of HAP1 cells**

Proteomic analysis was performed on 6 independent replicates of HAP1 parental cell line and 3 independent replicates of HAP1 PBRM1-KO cell line. Cells were harvested at 70% confluence. Cell pellets were dissolved in 150 μ L lysis buffer of 1% sodium deoxycholate (SDC), 100mM triethylammonium bicarbonate (TEAB), 10% isopropanol, 50mM NaCl and Halt protease and phosphatase inhibitor cocktail (100X) (Thermo, #78442) on ice with pulsed probe sonication for 15 sec followed by boiling at 90 °C for 5 min and re-sonication for 5 sec. Protein concentration was measured with the Coomassie Plus Bradford Protein Assay (Pierce) according to manufacturer's instructions. Protein aliquots of 100 μ g were reduced with 5 mM tris-2-carboxyethyl phosphine (TCEP) for 1 h at 60 °C and alkylated with 10 mM Iodoacetamide (IAA) for 30 min. Proteins were finally digested with trypsin (Pierce) at 75 ng/ μ L overnight. The peptides were labelled with the TMT-11plex reagents (Thermo) according to manufacturer's instructions. Peptides were fractionated with the XBridge C18 column

(2.1 x 150 mm, 3.5 μ m, Waters) on a Dionex Ultimate 3000 HPLC system at high-pH. Mobile phase A was 0.1% ammonium hydroxide and mobile phase B was acetonitrile, 0.1% ammonium hydroxide. The TMT labelled peptide mixture was fractionated using a multi-step gradient elution at 0.2 mL/min. The separation method was: for 5 minutes isocratic at 5% B, for 35 min gradient to 35% B, gradient to 80% B in 5 min, isocratic for 5 minutes and re-equilibration to 5% B. Fractions were collected every 30 sec and vacuum dried. LC-MS analysis was performed on the Dionex Ultimate 3000 system coupled with the Orbitrap Lumos Mass Spectrometer (Thermo Scientific). Peptide fractions were reconstituted in 40 μ L 0.1% formic acid and 10 μ L were loaded to the Acclaim PepMap 100, 100 μ m x 2 cm C18, 5 μ m, 100 Å trapping column at 10 μ L/min flow rate. The samples were then analysed with the Acclaim PepMap RSLC (75 μ m x 50 cm, 2 μ m, 100 Å) C18 capillary column at 45 °C. Mobile phase A was 0.1% formic acid and mobile phase B was 80% acetonitrile, 0.1% formic acid. The gradient method at flow rate 300 nL/min was: for 90 min gradient from 5%-38% B, for 10 min up to 95% B, for 5 min isocratic at 95% B, re-equilibration to 5% B in 5 min, for 10 min isocratic at 10% B. Precursor ions within 375-1,500 m/z were selected at mass resolution of 120 k in top speed mode (3 sec cycle) and were isolated for CID fragmentation with quadrupole isolation width 0.7 Th, collision energy 35% and max IT 50 ms. MS3 spectra were obtained with further HCD fragmentation of the top 5 most abundant CID fragments isolated with Synchronous Precursor Selection (SPS). Collision energy was applied at 65% with 105 ms IT and 50 k resolution. Targeted precursors were dynamically excluded for further activation for 45 seconds with 7 ppm mass tolerance. The mass spectra were submitted to SequestHT for database search in Proteome Discoverer 2.2 (Thermo Scientific) using reviewed UniProt human protein entries. The precursor mass tolerance was 20 ppm and the fragment ion mass tolerance was 0.5 Da for fully tryptic peptides. TMT6plex at N-terminus/K and Carbamidomethyl at C were selected as static modifications. Dynamic modifications were oxidation of M and Deamidation of N/Q. Peptide confidence was estimated with

the Percolator node and peptides were filtered for $q\text{-value} < 0.01$ based on decoy database search. The reporter ion quantifier node included a TMT 11plex quantification method with an integration window of 15 ppm at the MS3 level. Only unique peptides were used for quantification, considering protein groups for peptide uniqueness. Peptides with average reporter signal-to-noise > 3 were used for protein quantification.

Transcriptomic analysis was performed on 4 independent replicates of HAP1 PBRM1-KO and -WT cell lines, harvested at 70% confluence. RNA quality was verified for RNA Integrity Number (RIN) above 9. Gene expression was assessed using 8 X 60K Agilent® Human microarray (ID 039494) at the genomic platform of Gustave Roussy.

Transcriptomic and proteomic differential expression analysis were performed using Limma-Voom after normalization and removing outliers, following Law et al. (Law, C.W., Chen, Y., Shi, W. et al. voom: precision weights unlock linear model analysis tools for RNA-seq read counts. *Genome Biol* 15, R29 (2014). and Smyth GK *Stat Appl Genet Mol Biol*. 2004;3:Article3. Epub 2004 Feb 12 Linear Models and Empirical Bayes Methods for Assessing Differential Expression in Microarray Experiments. *Statistical Applications in Genetics and Molecular Biology*, 3(1)). Enrichment analysis was performed using R package clusterProfiler-v3.0.4 (Yu G, Wang L, Han Y and He Q. clusterProfiler: a R package for comparing biological themes among gene clusters. *OMICS: A Journal of Integrative Biology*, 2012, 16(5):284-287.)

i. **DRIP-seq**

786-0 and H1299 cells were plated in DMEM and RPMI medium, respectively. The day after plating, cells were treated with talazoparib (500 nM for H1299 cells and 1 μ M for 786-0) or DMSO for 24h. Cells at 75-80% confluence were then collected. DRIP-seq was performed as in Sanz et al, Nat. Protoc 2019 Nat Protoc. 2019 Jun;14(6):1734-1755. Briefly, trypsinized cells were washed in PBS and lysed in 1.6mL TE buffer (10mM Tris-HCl pH8, 1mM EDTA) supplemented with 50 μ L of SDS 20% and 5 μ L Proteinase K (20mg/mL) at 37°C O/N. Genomic DNA was extracted with phenol/chloroform, ethanol precipitated and fragmented using a cocktail of restriction enzymes (BsrGI, EcoRI, HindIII, SspI, XbaI; New England Biolabs, 30U each) by digestion overnight at 37°C. Fragmented DNA was purified by Phenol/Chloroform followed by ethanol precipitation. 8.8 μ g of DNA was then subjected to immunoprecipitation with 10 μ g of S9.6 DNA:RNA hybrid-specific monoclonal antibody (Kerafast) by incubating O/N at 4°C. Immune complexes were captured using Dynabeads Protein G magnetic beads (Invitrogen), eluted and purified by phenol/chloroform followed by ethanol precipitation. A specificity control of the reaction was done by treating 10 μ g of fragmented DNA with RNaseH before performing the immunoprecipitation reaction. An aliquot of the DRIP reaction was used to perform quantitative PCR reaction to evaluate DRIP efficiency. The amount of DNA in input and immunoprecipitated material was quantified in 3 R-loops positive regions (RPL13A, TFPT and CALM3) and 2 negative regions (EGR1 and SNRNP).

Sequencing libraries for all the samples were constructed using NEBNext® Ultra™ II DNA Library Prep Kit for Illumina®, quality controlled with Agilent Bioanalyzer 2100 (DNA High Sensitivity Kit) and quantified with Qubit Fluorometer (Invitrogen). The libraries were sequenced on NovaSeq sequencer.

Alignment to the Hg38 build was carried out using Bowtie2 (Langmead B, Salzberg S. Fast gapped-read alignment with Bowtie 2. *Nature Methods*. 2012, 9:357-359.), and peak calling was done using MACS2 (Zhang, Y., Liu, T., Meyer, C.A. et al. Model-based Analysis of ChIP-Seq (MACS). *Genome Biol* 9, R137 (2008) doi:10.1186/gb-2008-9-9-r137), peaks were called using all mapped reads after removing duplicates, enforcing a greater than 1-fold enrichment above input control datasets, as well as an FDR<0.01. Differential analysis was performed using R package DiffBind-v3.1 (Stark R, Brown G (2011). DiffBind: differential binding analysis of ChIP-Seq peak data.)

IV. **Statistical analysis**

No statistical methods were used to predetermine sample size and the experiments were not randomized. The investigators were not blinded to allocation during experiments and outcome assessment. Unless stated otherwise, all bar graphs show mean values with error bars (standard deviation, SD); 95% confidence intervals were used, and significance was considered when * $P < 0.05$, ** $P < 0.01$, *** $P < 0.001$, **** $P < 0.0001$; ns, not significant.

All statistical tests were performed using GraphPad Prism V8.0.2 software. All tests and *post-hoc* analyses were selected under the supervision of a biostatistician.

Chapter III: Characterization of a *PBRM1*-isogenic cellular model

I. Introduction and preliminary work

To initiate this work, we choose a functional genomic approach that consisted in: (i) selecting and generating relevant cellular models of *PBRM1* deficiency to work with *in vitro*, (ii) characterizing the whole transcriptional impact of *PBRM1* deficiency in one model, and (iii) characterizing the resultant impact on whole proteomic expression of *PBRM1* deficiency in this same model. The systematic characterization of the molecular response to *PBRM1* loss may eventually uncover evidence of functional vulnerabilities that could be efficiently targeted.

To do so in a relatively unbiased fashion, we collected and generated multiple stable isogenic pairs of cell lines, as described in Chapter II – Table 7; which all comprise a parental cell line expressing a wild type *PBRM1* gene (*PBRM1*-WT) and a daughter cell line deriving from the parental only by one single genetic intervention – via Clustered Regularly Interspaced Short Palindromic Repeats (CRISPR)/Cas9 – to stably disable the *PBRM1* gene (*PBRM1*-KO). This method minimizes the impact of the whole genetic background of the cells to allow a proper assessment of what are likely to be the specific consequences of *PBRM1* loss. Altogether, we collected and generated four *PBRM1*-isogenic pairs from various histological backgrounds (HAP1, haploid chronic myeloid leukemia; U2OS, osteosarcoma; 786-O, ccRCC; H1299, non-small cell lung cancer), and four non-isogenic ccRCC cell lines that were naturally proficient (786-O, A498) or deficient (RCC-MF, RCC-FG2) for *PBRM1* (Figure 16).

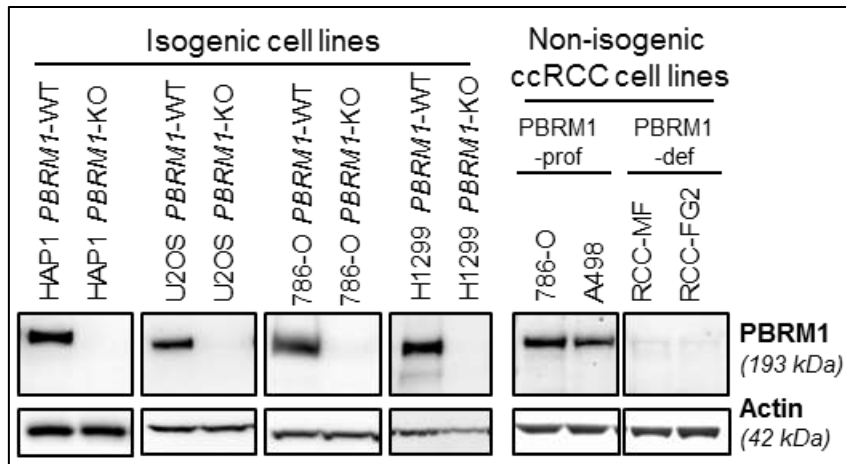


Figure 16. Western blot of PBRM1 expression on total cell extracts in four PBRM1-isogenic cellular models and four non-isogenic ccRCC cell lines. Actin is shown as a loading control.

In this preliminary Chapter, are presented the transcriptional and proteomic impacts of the loss of PBRM1 in the HAP1 *PBRM1*-isogenic model.

II. **Systematic characterizations of the HAP1 *PBRM1*-isogenic model**

a. **Transcriptional characterization of the HAP1 model**

To study the transcriptomic modifications induced by PBRM1 loss, we performed a transcriptomic analysis on the HAP1 cellular model using 8 X 60K Agilent® Human microarray. After *in silico* removal of lower quality reads, and subsequent alignment of trimmed reads to the human reference genome (GRCh38), a differential expression analysis was performed to measure gene expression changes between the HAP1 *PBRM1*-WT and HAP1 *PBRM1*-KO cell lines.

Differentially expressed genes were defined as those with a Benjamini-Hochberg adjusted P-value of < 0.05 together with a > 1.5-fold change in expression. Subsequently, a Gene Set Enrichment Analysis (GSEA) was performed using the Gene Ontology (GO) terms of the Biological Process knowledgebase (N = 1286 GO terms),

in order to investigate whether enrichments in specific pathways were generated by the loss of PBRM1.

Out of 1286, we found 127 biological processes significantly under-expressed in HAP1 *PBRM1*-KO cells compared to -WT cells, and 127 additional biological processes significantly overexpressed. We present here the top 20 of the most significantly down- and up-regulated pathways following PBRM1 loss (Figure 17).

Not surprisingly, the majority of the most downregulated pathways related to epigenetic processes such as regulation of gene and chromatin silencing, nucleosome and chromatin assembly, DNA packaging etc. Importantly, *PBRM1*-KO cells were found significantly enriched in downregulated DNA DSB repair pathway (NES = -1.82; adjusted p-value = 0.022).

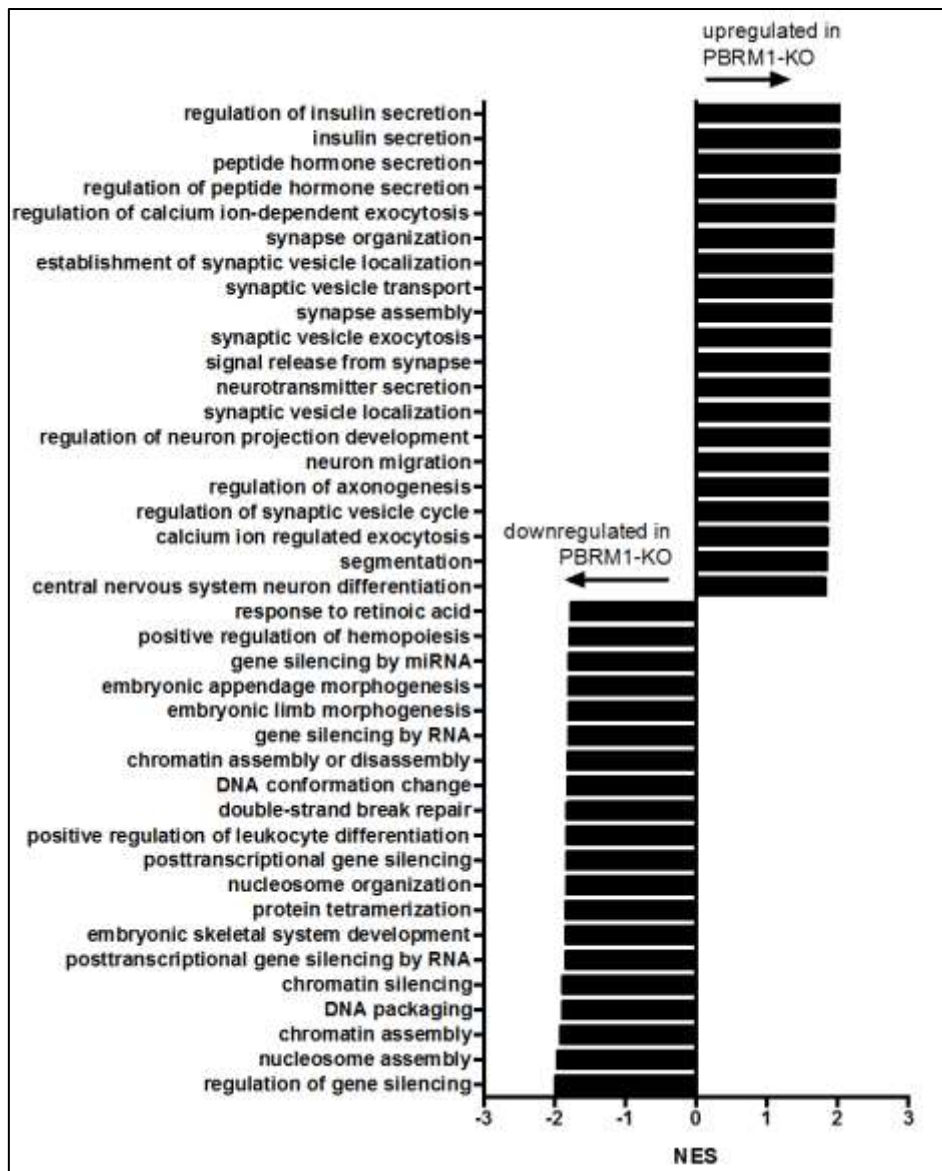


Figure 17. GSEA displaying the top 20 of up- and down-regulated GO Biological Processes pathways in the transcriptome analysis of HAP1 *PBRM1*-KO cells compared to *PBRM1*-WT cells. NES: normalized enrichment score.

b. Proteomic characterization of the HAP1 model

To further investigate the functional impact of PBRM1 deficiency at the proteomic level, we additionally performed a whole proteome analysis on the HAP1 isogenic model using liquid chromatography – mass spectrometry (LC-MS). Differential expression analysis and subsequent enrichment analysis were performed using the same precision weights unlock linear model analysis tools and the same cut-offs to allow comparison with transcriptomic data (Figure 18).

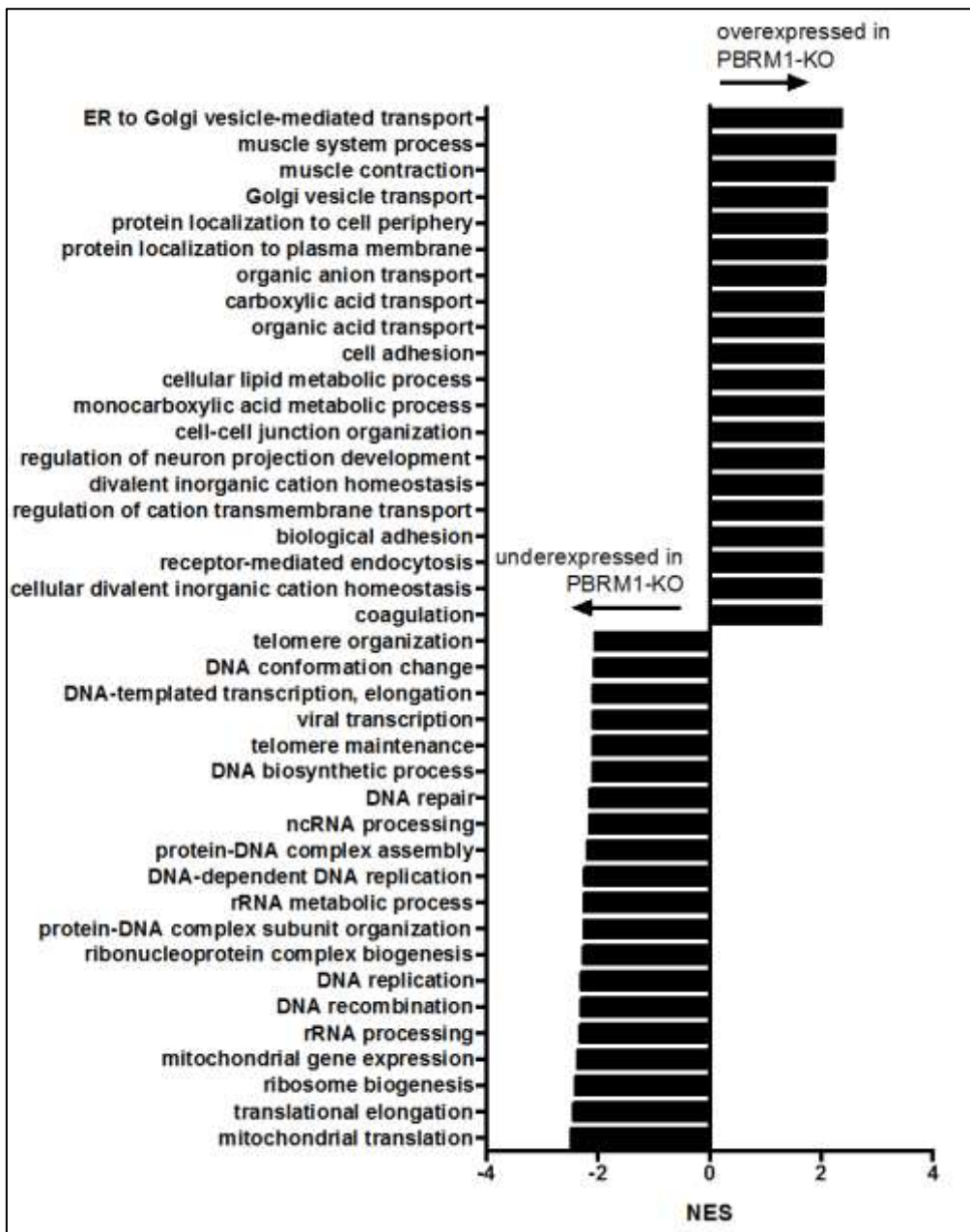


Figure 18. GSEA displaying the top 20 of up- and down-regulated GO Biological Processes pathways in the proteome analysis of HAP1 *PBRM1*-KO cells compared to HAP1 *PBRM1*-WT cells. NES: normalized enrichment score.

The GSEA of the proteomic data showed 142 and 309 biological processes respectively significantly under-expressed and over-expressed. Among the 20 biological processes significantly enriched to be downregulated in *PBRM1*-KO cells compared to -WT cells, we again found deregulation in proteins implicated in DNA

repair (NES = -2.1; adjusted p-value = 0.0079). The “double-strand break repair” GO term previously highlighted in the transcriptomic analysis was found ranked #22 out of 142 significantly downregulated enriched terms (NES = -2.0; adjusted p-value = 0.0079).

To note, the epigenetic processes that were found downregulated in the transcriptomic analysis were found decreased to a much less extent in the proteomic analysis, suggesting that these alterations might be partly compensated during post-transcriptional regulation processes. In contrast, biological processes related to ribosomal transcription appeared to be newly significantly decreased in the proteomic analysis (ribosome and ribonucleoprotein biogenesis, rRNA processing, translational elongation etc). Additionally, DNA replication related processes appeared among the most under-expressed biological processes following PBRM1 loss in our model (“DNA replication”, ranked #8; NES = - 2.29; adjusted p-val = 0.0078; “DNA-dependent DNA replication”, ranked #12; NES = - 2.23; adjusted p-val = 0.0078). In the transcriptomic analysis, the “DNA replication” GO term was also found significantly down-regulated (ranked #42; NES = - 1.65; adjusted p-val = 0.022).

To note, EZH2 protein expression was decreased in HAP1 *PBRM1*-KO cells compared to -WT cells (-29% decrease of mean expression, p = 0.0015).

III. Discussion

In this preliminary Chapter, we aimed at drawing a general picture of the molecular and cellular impact of PBRM1 loss on the global transcriptional and proteomic landscapes of the cells. Consistently with previous reports^{73,82,85}, whole transcriptome and proteome analysis showed consistent down-regulation in DNA repair biological processes. Additionally, we observed previously-unknown modifications in the

processes related to transcriptional elongation and to DNA replication, both mechanisms appearing to be down-regulated following PBRM1 defects.

Of note, our HAP1 *PBRM1*-isogenic model showed a down-regulation in EZH2 expression following loss of PBRM1, suggesting that the regulation of EZH2 expression, in that cell line model, might not be similar to what has been described with the loss of SMARCB1 in malignant rhabdoid tumor ⁹⁸.

Overall, these preliminary observations could not identify an evident genetic or epigenetic vulnerability related to PBRM1 defect; although we observed a potentially global DNA repair deficiency. We therefore hypothesized that targeting DNA repair defects using PARP, ATR, ATM or DNA-PK inhibitors for example, might selectively affect the growth of PBRM1-deficient tumour cells.

Chapter IV: PBRM1-deficiency associates with increased sensitivity to PARP inhibitors

I. Introduction

The investigation of previously published roles of PBRM1 highlighted a wide variety of processes that could represent vulnerabilities for *PBRM1*-KO cells (Figure 15), notably DNA repair (Cf Chapter III). To limit bias associated with the manual choice of potential drug candidates and to maximize our chances to uncover the best therapeutic options associated with PBRM1-deficiency, we performed a high-throughput pharmacological screening on the above-described HAP1 *PBRM1*-isogenic model. We mostly focused on drugs implicated in the targeting of DNA damage repair deficiencies, epigenetic-modifying drugs and some cytotoxic compounds approved for the treatment of solid cancers.

The findings associated with the analysis of the screen were then validated in multiple cellular models using low-throughput conventional assessment of cellular growth and survival, with both 2D and 3D cellular culture methods.

II. Results

a. High-throughput drug screening

Because already had characterized the *PBRM1*-WT and -KO HAP1 isogenic model at the transcriptome and proteome level, we choose this model for the drug screen. Both cell lines were exposed for five days to 167 small molecules including cytotoxic agents, epigenetic-modifying drugs, protein kinase inhibitors and DNA repair inhibitors (Figure 19). Small molecule inhibitors were evaluated in dose-response at eight concentrations in triplicate for each cell line. Area Under the Curve (AUC) values

were calculated for each small molecule inhibitor, identifying 37 small molecule inhibitors that exerted interesting cytotoxic effects selectively in the *PBRM1*-KO cell line, including two clinical PARP inhibitors (olaparib and veliparib) and two ATR inhibitors (VE-822 and VE-821), as being selectively toxic towards *PBRM1*-defective cells. Details of the compounds and associated AUC differences are provided in Table 10.

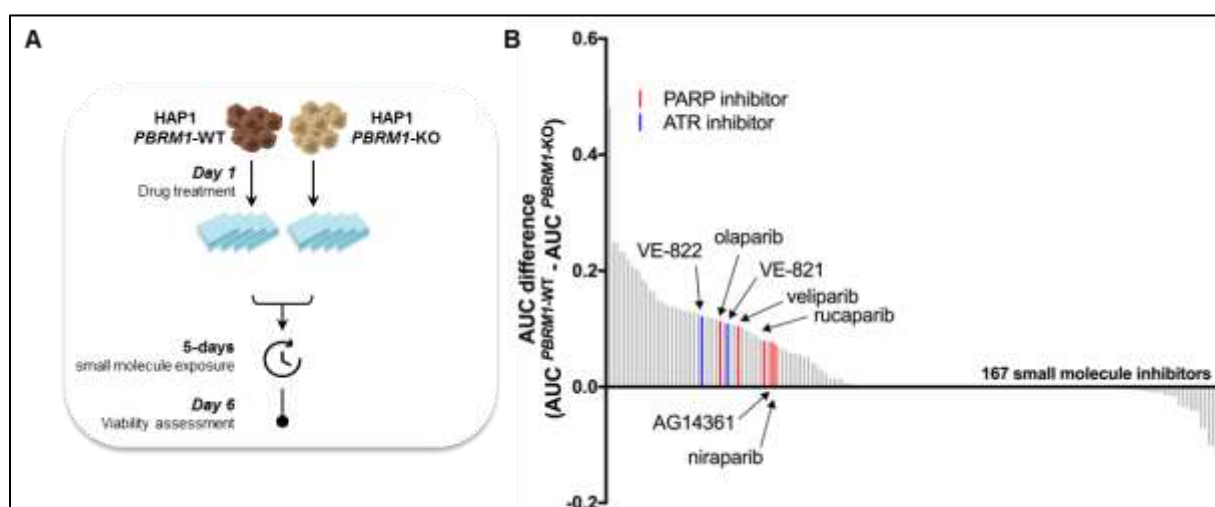


Figure 19. High-throughput drug screen on *PBRM1*-WT and -KO HAP1 cells. A. Schematic representation of the high-throughput drug screen in HAP1 *PBRM1*-isogenic cells. B, barplot displaying the AUC difference between the HAP1 *PBRM1*-WT and -KO cells for the 167 evaluated small molecules. PARP and ATR inhibitors are highlighted in red and blue, respectively. AUC, Area Under the Curve.

Table 10. High-throughput small molecule inhibitor screen in *PBRM1*-WT and -KO HAP1 cells. Drug screen AUC difference (AUC_diff) between HAP1 *PBRM1*-KO and -WT. Compounds are ranked by alphabetical order.

ID	Compound ID	AUC_diff
1	17-AAG	0.103
2	2-METHOXYESTRADIOL	0
3	A-1210477	0
4	A-674563	0.207
5	ABIRATERONE	0
6	ABT-737	0
7	ABT888/VELIPARIB	0.105
8	AFATINIB	0
9	AFIMOXIFENE	0
10	AG-14361	0.078
11	AG-14699	0.081
12	AG-14699	0.003
13	AMONAFIDE	0.151
14	AT7519	0.082
15	AT7519 HCL	0.057
16	AZD4547	0
17	AZD5438	0
18	AZD7762	0.028
19	AZD8055	0.204
20	BENDAMUSTINEHCL	0
21	BETA-LAPACHONE	0
22	BEZ-235	0.013
23	BI-2536	0
24	BLEOMYCIN	0.129
25	BLEOMYCIN	-0.014
26	BMN-673	0
27	BMN-673	-0.007
28	BMS-265246	0.481
29	BMS-911543	0
30	CABOZANTINIB	0
31	CAMPTOTHECIN	0.041
32	CAMPTOTHECIN	-0.008
33	CANERTINIB	0
34	CARMOFUR	0

35	CCT271850	0.118
36	CELECOXIB	0
37	CLOFARABINE	-0.004
38	CRIZOTINIB	0.055
39	CYCLOPHOSPHAMIDE	0
40	DASATINIB	0.059
41	DAUNORUBICINHCL	0.097
42	DECITABINE	-0.04
43	DINACICLIB	0.051
44	DMX_1783	0
45	DMX_1783	0
46	DMX_1913	0.131
47	DMX_2320	-0.121
48	DMX2131	0
49	DOXORUBICIN	0.143
50	DOXORUBICIN	-0.041
51	E3330	0
52	EPIRUBICIN HCL	0.139
53	EPZ6438	0
54	ERLOTINIB	0
55	ETOPOSIDE	0.126
56	ETOPOSIDE	-0.101
57	EVEROLIMUS	0.031
58	FLAVOPIRIDOL	0.057
59	FLAVOPIRIDOL	-0.005
60	FLAVOPIRIDOLHCL	0.079
61	FLUDARABINE	0
62	FLUOROURACIL	0
63	FLUOROURACIL	0
64	FORETINIB	-0.009
65	GATIFLOXACIN	0
66	GEFITINIB	0
67	GEMCITABINE	-0.123
68	GSK2194069A	0.001
69	GSK-2334470A	0
70	IMATINIB	0
71	INIPARIB	0
72	IRINOTECAN	0.051

73	IRINOTECAN TRIHYDRATE	0.007
74	JNJ-7706621	0.068
75	KU0057788	0
76	KU0057788	0.147
77	KU-55933	-0.001
78	KU60019	0.107
79	KU60019	-0.031
80	LAPATINIB	0
81	LDC000067	0
82	LEE011	0.12
83	LESTAUTINIB	-0.035
84	LOMUSTINE	0
85	LY2603618	0.129
86	LY2835219	0.25
87	MERCAPTOPYRINE	0
88	METHOTREXATE	-0.014
89	METHOTREXATE/ABITREXATE	-0.01
90	MILCICLIB	0.112
91	MITOXANTRONE HCL	0.137
92	MK0752	-0.016
93	MK-1775	0
94	MK2206	0
95	MK4827	-0.101
96	MK-8776	0.074
97	ML167	0.185
98	MLN-4924	0.062
99	MLN-4924	-0.071
100	MSC2504877A	0.066
101	MSC4070	0.199
102	NILOTINIB	0
103	NU6027	0
104	NUTLIN3	0
105	NUTLIN3	0
106	NVP656	0
107	OLAPARIB	0.114
108	OLAPARIB	0.015
109	OSI-027	0
110	OSI-906	0

111	P276-00	0.088
112	PACLITAXEL	0.002
113	PALBOCICLIB	0.18
114	PALBOCICLIB MERCK	0.234
115	PD173074	0
116	PD-184352	0
117	PD407824	0.108
118	PEFLOXACIN	0
119	PF-00299804	0
120	PF-00477736	0.164
121	PF-00477736	0.005
122	PF-02341066	-0.01
123	PF-03758309	0.04
124	PF-03814735	-0.072
125	PF-04691502	0.014
126	PF-332991	-0.005
127	PF3644022	0
128	PHA-767491	0
129	PHA-793887	0.131
130	PIK-75	0.138
131	PIRARUBICIN	0.117
132	PLX-4720	0.166
133	PP121	0.249
134	PURVALANOL A	0
135	RO-3306	0
136	R547	0.098
137	RALTITREXED	-0.01
138	RESVERATROL	0
139	RITA(NSC652287)	0
140	RO-3306	0
141	SALINOMYCIN	-0.017
142	SAPACITABINE	-0.004
143	SAR-20106	-0.003
144	SATRAPLATIN	0.12
145	SN-38	0.022
146	SNS-032	0.219
147	SNX-5422	-0.005
148	SORAFENIB	0

149	SOTRASTAUIN/AEB071	0
150	SU9516	0.005
151	SUNITINIB	0.015
152	TEMOZOLOMIDE	0
153	TEMOZOLOMIDE	0
154	TG003	0
155	TOPOTECAN HCL	0.135
156	TORIN	0.231
157	TRIAPINE	-0.042
158	UPF1035	0
159	UPF-1069	0
160	VE-821	0.111
161	VINOURELBINE	0.09
162	VISMODEGIB	0
163	VORINOSTAT	0
164	VX-970	0.122
165	XAV-939	0
166	YM155	-0.034
167	ZEBULARINE	0

Because PARP and ATR inhibitors were among the most clinically-advanced small molecule inhibitors identified in our screen, we chose to focus on these molecules for further developments and mechanistic investigations.

b. **Low-throughput validation in isogenic cellular models**

In order to validate the synthetic lethal effects of PARPi that we identified in the screen, we used three chemically-distinct approved clinical PARP inhibitors (PARPi: olaparib, rucaparib and talazoparib) in four of our *PBRM1*-isogenic systems to assess the effect of PARPi on cell survival.

We first validated the selective sensitivity of HAP1 *PBRM1*-KO cells to olaparib, rucaparib and talazoparib, which was previously detected in drug screen (Figure 19), and confirmed that the *PBRM1*-KO HAP1 cell line was significantly more sensitive to all the three PARPi than its *PBRM1*-WT isogenic counterpart in 7-days IC₅₀ assays (Figure 20A; $p < 0.0001$, two-way ANOVA). We then intended to extend these results to our other isogenic systems and consistently found that *PBRM1*-KO cells were more sensitive to multiple PARPi than their *PBRM1*-WT parental cells (Figure 20B-C).

Because the access to nutrients and oxygen might influence the epigenetic programs⁹⁹, we also optimized 3D cell culture when the cell line phenotypes allowed it (HAP1, 786-O). Although the magnitude of the effect on cell survival varied according to the cell type and the selected drug, a significant difference between *PBRM1*-KO and -WT cells could be observed either in 2D culture IC₅₀-assays or in 3D spheroid growth assay, after at least 7 days of treatment (and up to 20 days in 3D culture) (Figure 20D-E). We additionally confirmed these findings in long-term colony-forming assay (Figure 21).

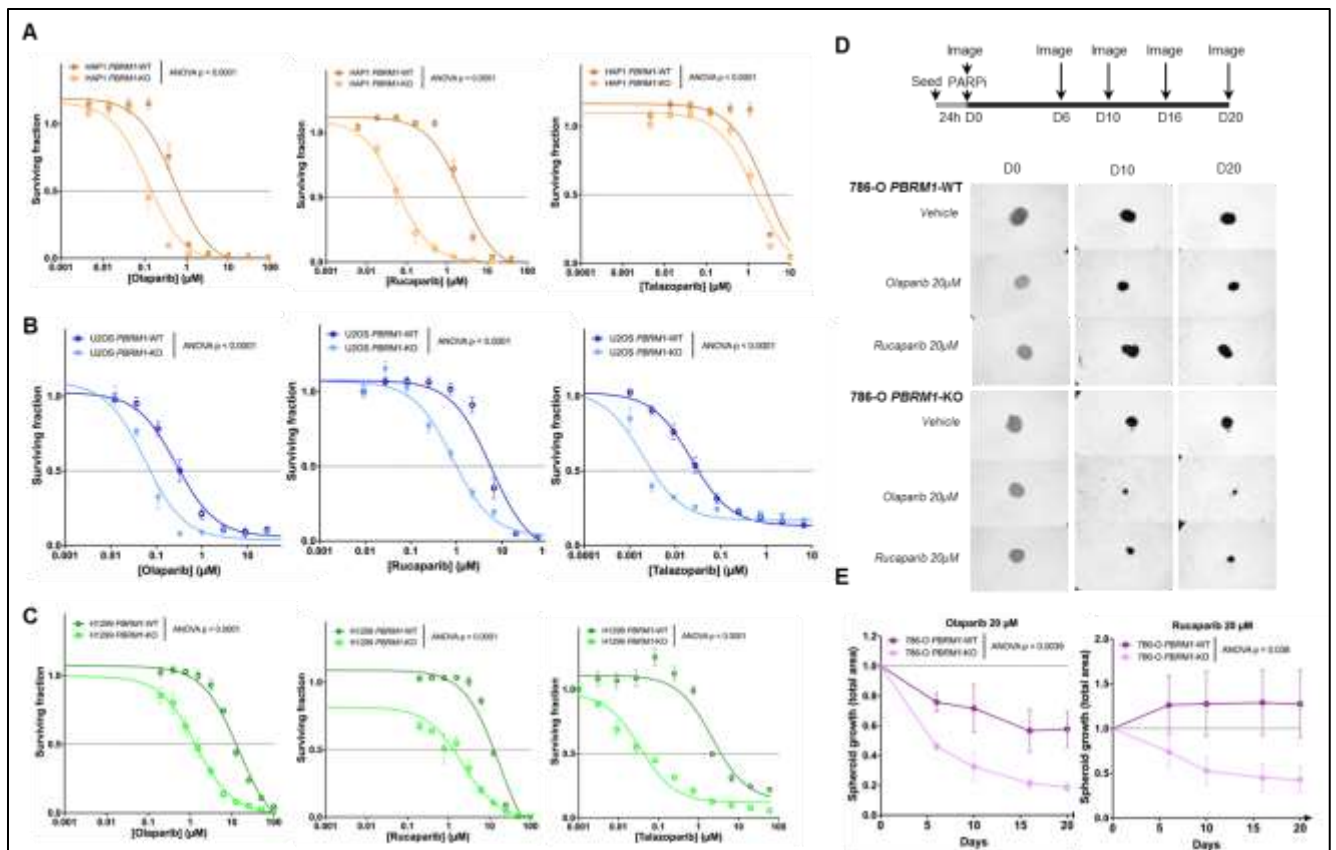


Figure 20. Low-throughput validation of PARPi sensitivity. A-C, Dose-response survival curves of the HAP1 (A), U2OS (B) and H1299 (C) *PBRM1*-isogenic models exposed to increasing concentrations of several clinical PARP inhibitors (from left to right: olaparib, rucaparib and talzoparib) in 2D culture for 7 days. Mean \pm SD, $n = 3$ independent replicates; two-way ANOVA. D, Representative pictures of spheroid of 786-O PBRM1-WT or -KO cells exposed to 20 μM of olaparib or rucaparib for 20 days in 3D assay. Representative images were taken using an EVOS® microscope at X4 objective at D0, D10 and D20. Spheroid area was measured using ImageJ® software. E, Evolution of the spheroid area over time following olaparib (left) or rucaparib (right) exposure, normalized to the DMSO condition for each cell line. Mean \pm SD, $n = 3$; two-way ANOVA.

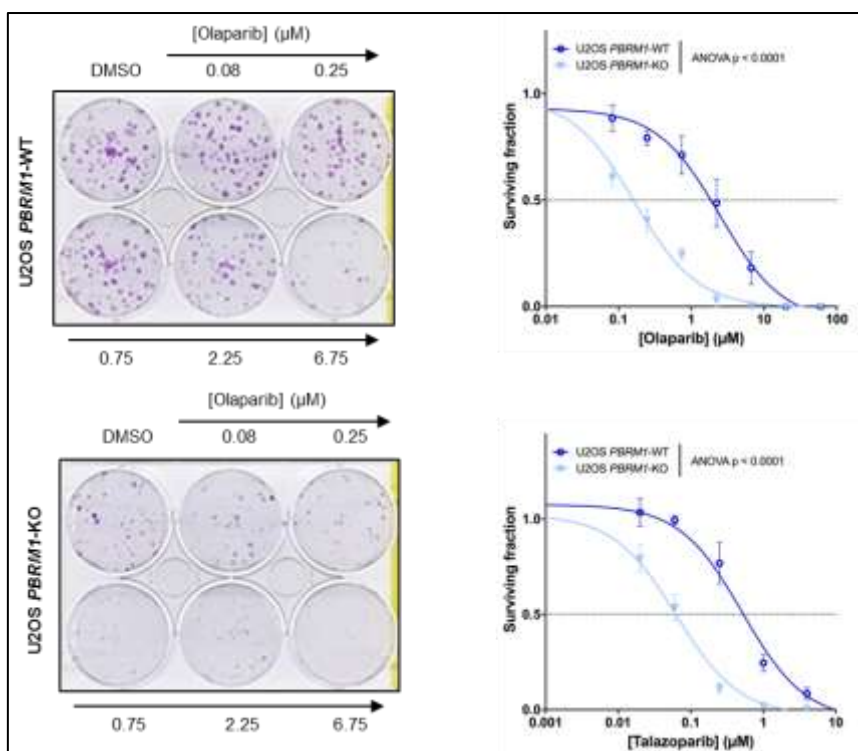


Figure 21. Dose-response colony-forming assay survival curves (right) and representative pictures (left) of the U2OS *PBRM1*-isogenic cells exposed to increasing concentrations of olaparib for 10 days (U2OS *PBRM1*-WT) or 14 days (U2OS *PBRM1*-KO) in colony formation assay. Mean \pm SD, n = 3; two-way ANOVA.

Regarding the sensitivity to ATRi that we observed in the preliminary screen 2, low-throughput assessment of the effect of ATRi in monotherapy on our models confirmed that *PBRM1*-KO cells were more sensitive than -WT cells, although the effect was less profound than with PARPi (Figure 22A). As drug combinations comprising a PARPi and an ATRi are currently under clinical development, including in *ARID1A*-mutated gynecological cancers (NCT04065269, NCT03682289, NCT03462342, NCT04267939 etc.), we evaluated whether *in vitro* combining of PARPi and ATRi in *PBRM1*-deficient models could increase the therapeutic window between *PBRM1*-KO and *PBRM1*-WT cells. We observed that adding an ATRi (VE821) to a PARPi (either olaparib or talazoparib) elicited additive effects and could indeed increase the shift between survival fractions of *PBRM1*-KO and *PBRM1*-WT cells in 786-O (Figure 22B) and U2OS models. However, unlike what was recently published in ATM-deficient models¹⁰⁰, we could not identify a synergistic activity neither

according to Bliss interaction analysis nor to Loewe interaction analysis (Figure 22C-D).

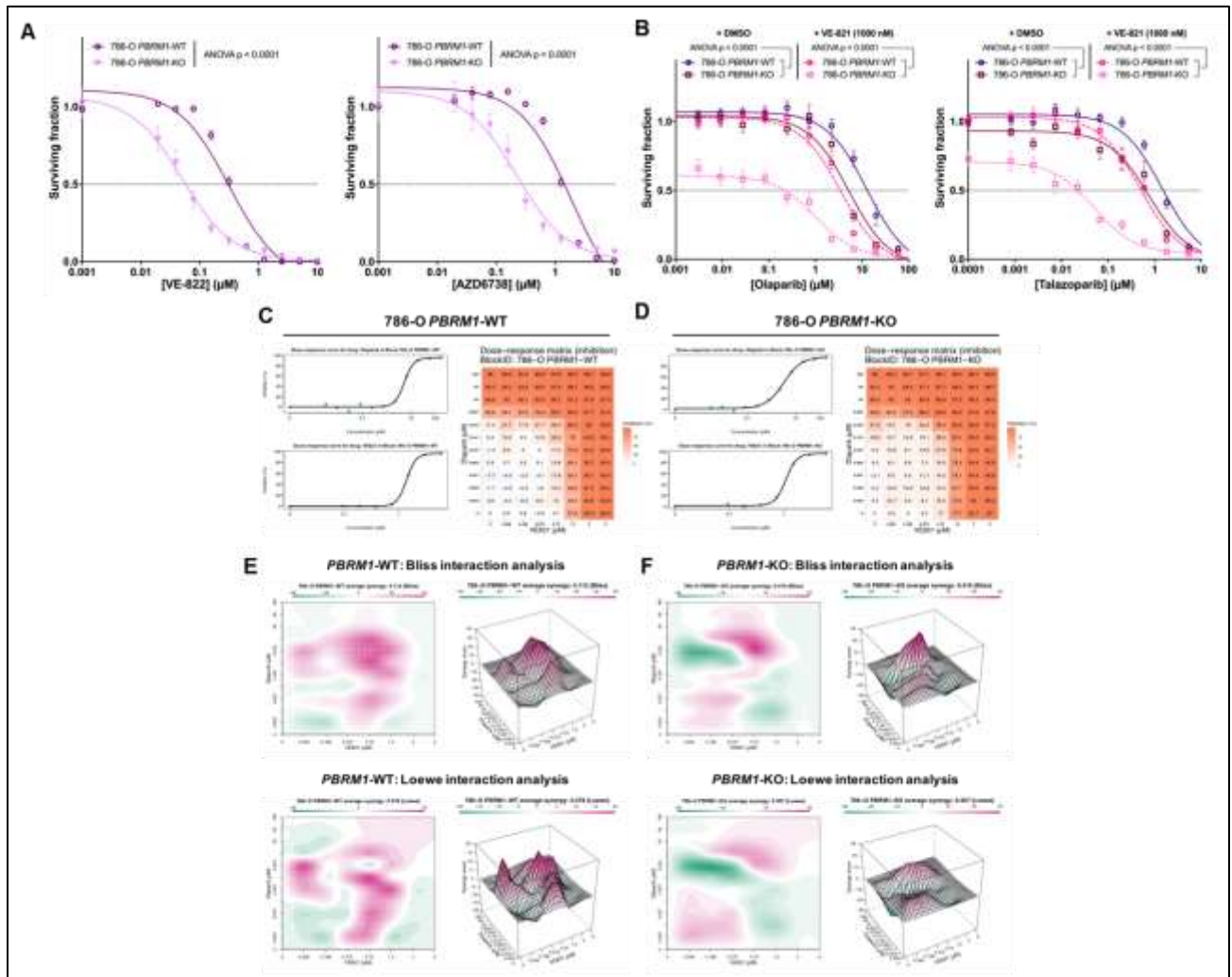


Figure 22. Additivity effects on cell survival of PARPi combined with ATRi. A, Dose-response survival curves of 786-O *PBRM1*-WT or -KO cells exposed to increasing concentrations of VE-822 (left) or AZD6738 (right) for 7 days. Mean \pm SD, $n = 3$; two-way ANOVA. B, Dose-response survival curves of 786-O *PBRM1*-isogenic cells exposed to increasing concentrations of olaparib (left) or talazoparib (right) in the presence or absence of VE-821 at 1000 nM. Survival fractions were normalized to the DMSO vehicle (absence of drug). Mean \pm SD, $n = 3$; two-way ANOVA. D-F, Dose-response curves, dose-response matrixes and synergy plots associated with the combination of olaparib and VE-821 in 786-O *PBRM1*-WT (C,E) and 786-O *PBRM1*-KO (D,F) cell lines. Synergy scores were calculated according to the Bliss (E,F, top panels) and Loewe (E,F, bottom panels) interaction methods. Synergy score < 10 indicates an antagonistic interaction; synergy score = 0 indicates the absence of interaction; Synergy score > 10 indicates a synergistic interaction.

c. **PBRM1-rescue restores initial phenotype**

To further confirm that PARPi sensitivity was a primary effect of PBRM1 deficiency, we re-expressed *PBRM1* in 786-O *PBRM1*-KO cells, by transducing a doxycycline-inducible cDNA (Figure 23A). Assessed in 3D spheroid growth assay, PBRM1 re-expression restored PARPi resistance (Figure 23B), thereby establishing the direct causality of PBRM1 loss-of-function in PARPi sensitivity.

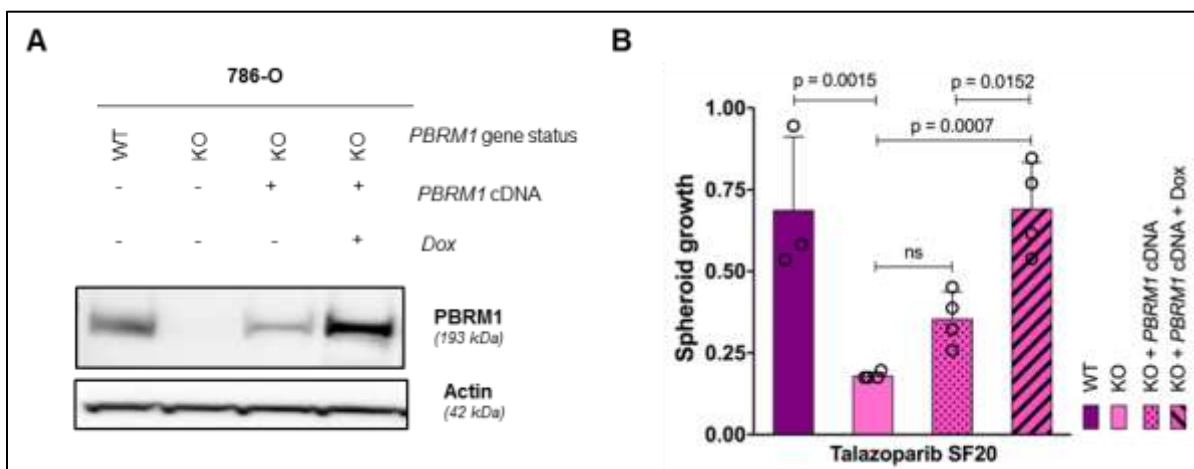


Figure 23. PARPi sensitivity following PBRM1 rescue. A, Western blot of PBRM1 expression in total cell extracts of 786-O *PBRM1*-isogenic cells before and after transduction with a doxycycline-inducible construct containing PBRM1 cDNA in the absence (+ PBRM1 cDNA) or presence (+ PBRM1 cDNA + Dox) of doxycycline. B, Spheroid growth of 786-O *PBRM1*-isogenic cells (as described in A) after 16 days of treatment with talazoparib at the *PBRM1*-KO model SF20 (5 μM). Mean ± SD, n = 3; two-way ANOVA and post hoc Tukey's test, relative to DMSO control.

d. **Enlarging the findings to non-isogenic cellular model of ccRCC**

Finally, to investigate the generality of this effect, we determined PARPi sensitivity in a molecularly diverse non-isogenic panel of ccRCC cell lines composed of two PBRM1-proficient cell lines (786-O and A498, homozygous and heterozygous *VHL*-mutant, respectively) and two PBRM1-deficient cell lines (RCC-MF and RCC-FG2, *VHL*-WT and -mutant, respectively) (Figure 24). Consistent with the observations made in

isogenic systems, loss of PBRM1 expression in *PBRM1* non-isogenic ccRCC cell lines was associated with sensitivity to several clinical PARPi.

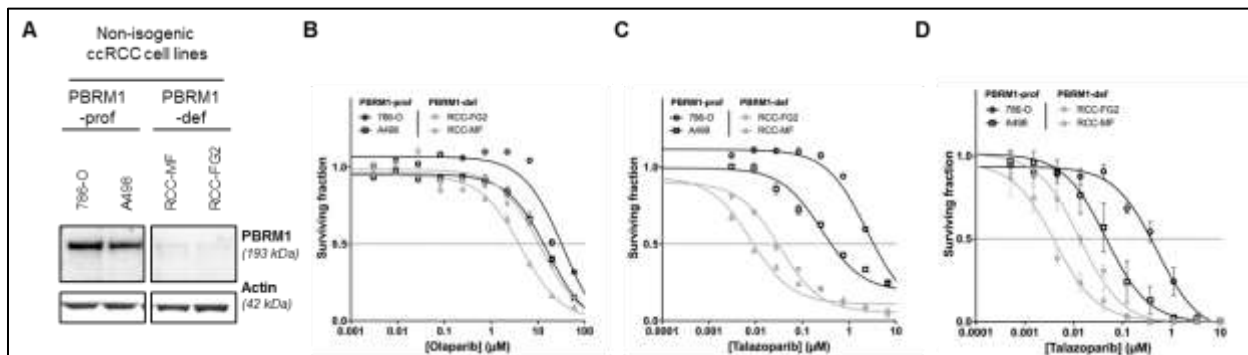


Figure 24. PARPi sensitivity in non-isogenic ccRCC cell lines. A, Western blot of PBRM1 expression in total extracts of PBRM1-proficient (786-O and A498) and -deficient (RCC-FG2 and RCC-MF) ccRCC cell lines. B,C, Dose-response survival curves of the PBRM1-proficient (786-O and A498) and -deficient (RCC-FG2 and RCC-MF) ccRCC cell lines exposed to olaparib (B) or talazoparib (C) for 7 days. Mean \pm SD, n = 3. D, Dose-response colony forming assay survival curves of PBRM1-proficient (786-O and A498) and -deficient (RCC-FG2 and RCC-MF) ccRCC cell lines exposed to increasing concentrations of talazoparib for 14 days in colony formation assay. Mean \pm SD, n = 3; two-way ANOVA.

III. Discussion

In this Chapter, we identified that the loss of PBRM1 triggered an increased sensitivity to PARPi *in vitro*, an effect that could be enhanced by adding an ATRi.

We observed some variability in the magnitude of the effect across various cell lines and PARPi, suggesting that the synthetic lethal effects of these drugs may be more profound in some systems than others. However, we consistently observed a significant therapeutic window between PBRM1-proficient and -deficient cell lines in both isogenic and non-isogenic systems following PARPi, which is in favor of a relatively penetrant PBRM1/PARPi synthetic lethality that may be cell-type independent.

Importantly, the re-expression of PBRM1 in the 786-O ccRCC *PBRM1*-KO cellular model rescued the initial phenotype, which was in favor of a direct link between the loss of PBRM1 and the sensitivity to PARPi.

In light of these findings, we hypothesized that DNA repair defects associated with PBRM1 deficiency might be the major cause of enhanced sensitivity to PARPi +/- ATRi and therefore, we undertook to more deeply characterize the DNA repair capacities of *PBRM1*-KO cells.

Chapter V: PBRM1 loss associates with enhanced genomic instability and replication stress

I. Introduction

The preliminary transcriptomic and proteomic analyses of the HAP1 *PBRM1*-isogenic model detailed in Chapter III highlighted that *PBRM1*-KO cells were enriched in down-regulated DNA repair capacities compared to *PBRM1*-WT cells. Additionally, we described in Chapter IV that *PBRM1*-KO cells were consistently more sensitive to PARPi than *PBRM1*-WT cells.

The main described mechanism by which a cell could be vulnerable to PARPi implies a deficiency in the homologous recombination (HR) DNA repair pathway¹⁰¹. In physiological condition, PARP1 (and the less abundant other PARP proteins, including PARP2) are DNA damage sensors that binds damaged DNA preferentially at sites of single-strand breaks (SSBs) during S phase¹⁰². Consequently to DNA binding, PARP1 undergoes a conformational change that activates its catalytic activity for adding poly(ADP-ribose) negatively-charged chains (PARylation) to various DNA repair enzymes, adjacent histones and itself, until its auto-PARylation prompts it to be released from the site to spatially allow the pursuing of DNA repair processes¹⁰³.

PARPi not only inhibit the catalytic PARylation activity of PARP1 and PARP2, but also prevent the release of PARP1 from DNA by “trapping” PARP1 at the site of damage, and thereby creating a “PARP1-DNA” nucleoprotein complex. These PARP1-DNA trapping lesions, when encountered by a progressing replication fork during S-phase, are source of replication fork collapse and therefore often result in a DNA DSB generation¹⁰⁴.

In case of HR primary deficiency (for example, BRCA1 or BRCA2 loss-of-function), error-free DNA repair that uses homologous DNA sequence to guide accurate repair could not be completed, thus collateral error-prone repair mechanisms – such as Non-Homologous End-Joining (NHEJ) – take over the damage, thus promoting genomic instability¹⁰¹. In such case, intense generation of DNA DSBs by PARPi rapidly over-exceeds the cell capacity to handle replication stress and often directs the cell to death within a few cell cycles.

Synthetic lethal interactions associated with PARPi sensitivity have been described beyond germline *BRCA* gene mutations¹⁰⁵. This “BRCAness” basically defines tumours that share certain phenotypes with *BRCA*-mutated tumours, including therapeutic vulnerabilities, but are BRCA1- and BRCA2-wild type. For example, deficiencies in other DNA repair proteins such as *ATM*, *ATR*, *PALB2* and the *FANCD1* gene family have been shown to cause PARPi vulnerability. Importantly, the PRIMA phase III randomized, double-blinded clinical trial provided the proof-of-concept that patients with platinum-sensitive advanced ovarian cancer whose tumour did not harbor HR deficiency could also significantly benefit from a PARPi therapy¹⁰⁶, suggesting that unknown mechanisms which are HR-independent can also drive PARPi sensitivity.

Although PBRM1 has been previously shown to have several roles during DNA repair⁸⁴⁻⁸⁷, it remains unclear by which mechanism PBRM1 loss drives sensitivity to PARPi, and more particularly, whether PBRM1 loss impacts the expression of one or several HR proteins. In this Chapter, we investigated the functional impact of PBRM1 deficiency in the absence of exogenous stress, in order to explore the mechanism underlying the PARPi sensitivity in *in vitro* isogenic models and in tumour samples from the TCGA publicly-available dataset.

II. Results

a. Impact of PBRM1 loss on protein involved in PARPi response

Because DNA repair dysfunctions have been shown to be targetable using PARP inhibitors (PARPi), we first investigated the differential expressions of each protein individually previously observed as being implicated in the sensitivity to PARPi, using the proteomic data of the HAP1 *PBRM1*-isogenic model (*list kindly provided by C. Lord, internal data*) (Figure 25).

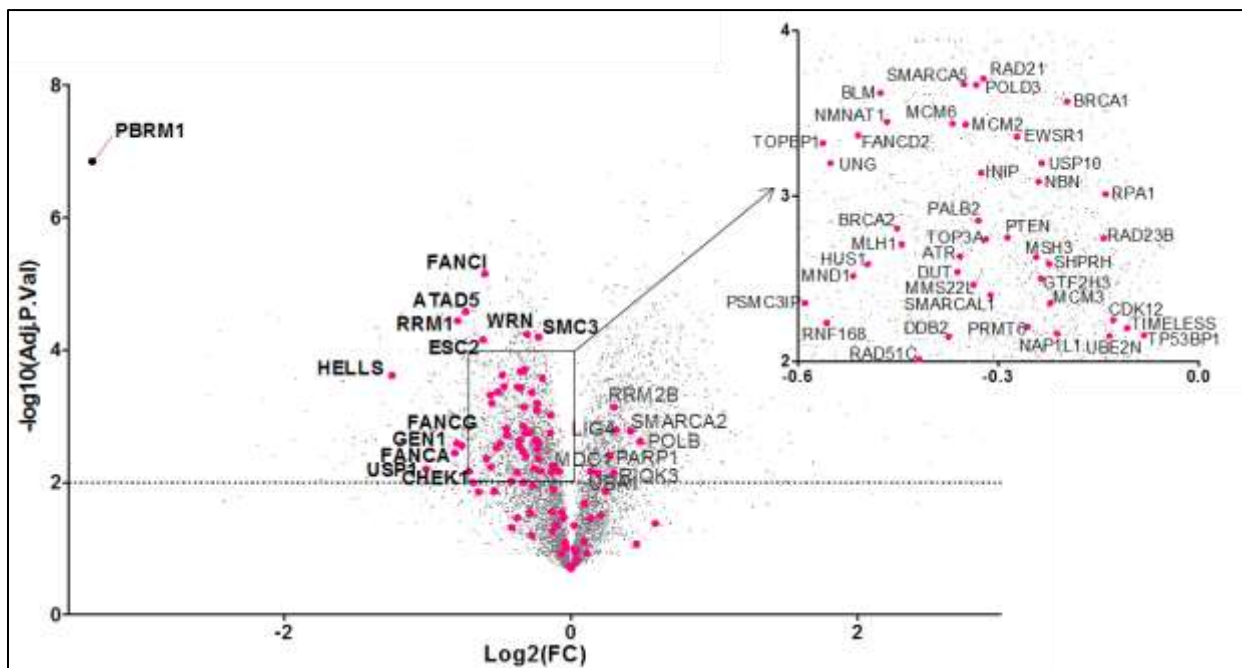


Figure 25. Volcano plot showing the significantly dysregulated proteins (grey dots) in HAP1 *PBRM1*-KO cells, as compared to HAP1 *PBRM1*-WT cells assessed by mass spectrometry. Proteins that have been reported to be involved in PARPi response are shown as pink dots; names of the significantly dysregulated ones (FDR q-value < 0.01) are depicted.

We observed that the majority of the protein involved in PARPi response were indeed significantly down-regulated in HAP1 *PBRM1*-KO cells compared to -WT cells,

although the magnitude of the observed down-regulations (in fold-change) was consistently modest and might not be sufficient to induce sensitivity to PARP inhibitors.

b. γ H2AX and RAD51 foci formation

γ H2AX foci are well-established marks of early DNA damage signaling which occur rapidly after a DNA DSB¹⁰⁷. In addition, RAD51 recruitment to γ H2AX sites indicates the activation of the HR pathway onto the lesions, downstream of BRCA1 and BRCA2, which is in favor of efficient HR repair processing¹⁰⁸. We therefore measured endogenous γ H2AX and RAD51 co-expressions by assessing baseline nuclear foci numbers with immunofluorescent assay in three molecularly distinct *PBRM1*-KO and -WT cell pairs.

Interestingly, we consistently identified a significantly higher number of both γ H2AX and RAD51 foci in *PBRM1*-KO cells compared to -WT cells, in all three cellular models tested (Figure 26). All RAD51 foci were found to co-localize with γ H2AX foci.

These observations highlighted two important features associated with *PBRM1* deficiency: (i) that *PBRM1* deficiency is associated with increased DNA damage signaling of DNA DSBs and (ii) that HR-related proteins could be correctly recruited at these DNA DSB sites, even in the absence of *PBRM1*.

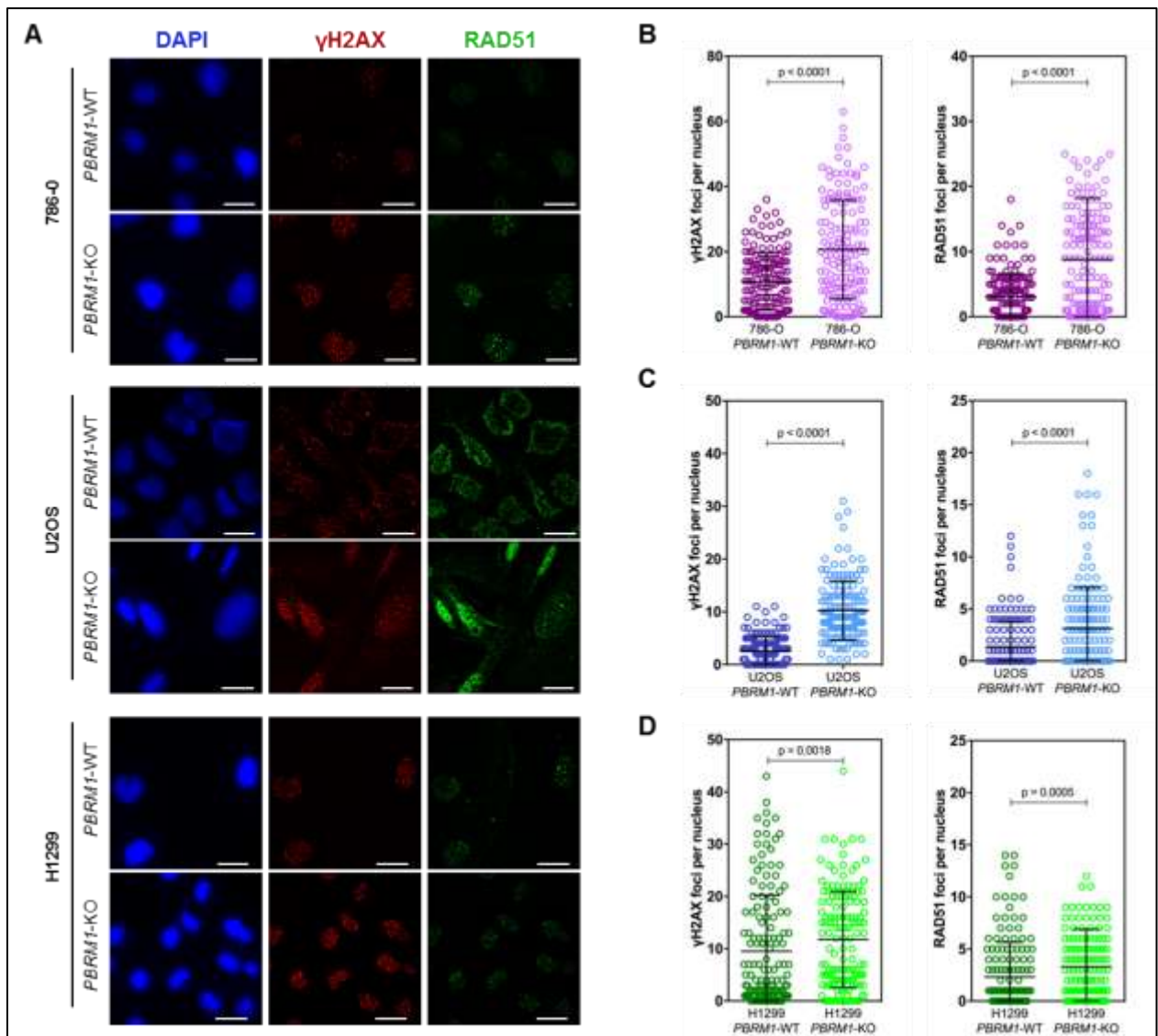


Figure 26. Quantification of γ H2AX and RAD51 foci per cells according to PBRM1 status. A, Representative immunofluorescence images of γ H2AX (red) and RAD51 (green) foci in the absence of exogenous treatment in 786-O, U2OS and H1299 *PBRM1*-isogenic cells. Scale bar: 20 μ m. B-D, Quantification of the baseline number of γ H2AX foci (left panels) and RAD51 foci (right panels) per nuclei in 786-O (B), U2OS (C) and H1299 (D) *PBRM1*-isogenic cells. At least 150 nuclei per condition were analyzed. Mean \pm SD; Wilcoxon-Mann-Whitney test.

C. Mutational load of PBRM1-defective tumours

Although PBRM1 loss-of-function does not seem to be linked to a HR defect, *PBRM1*-KO cells display a higher number of DNA damage response signaling at baseline compared to -WT cells (Figure 26), suggesting an increased genomic instability in those cells. To assess whether this higher rate of DNA DBSs might result in an increased number of oncogenic non-silent mutations in tumour samples, we estimated the mutational load within PBRM1-defective tumours compared to PBRM1-wild type tumours in the publicly available TCGA dataset (<https://www.cancer.gov/tcga>).

Using whole exome sequencing data, we first compared the total mutational load according to PBRM1 mutational status across all tumour types in which at least two samples were *PBRM1*-mutated. We observed that *PBRM1*-mutated samples had a higher mutational load than *PBRM1*-WT samples in all of the 19 tumour types, which were statistically meaningful (defined as adjusted p-value < 0.05) in 11 tumour types among the 19 (58%) (Figure 27A).

To further examine whether the mutational load also correlates with PBRM1 mRNA expression beyond its mutational status, we repeated the analysis but comparing PBRM1-low expressing tumours *versus* PBRM1-high expressing tumours using the RNA-sequencing TCGA data. High-expression samples were defined as samples that fell in the top quartile (top 25%) of expression for PBRM1, while low expression samples fell in the bottom two quartiles (bottom 50%). We found a significant negative correlation between PBRM1 expression and the mutational load in 6 tumours types: breast cancer (BRCA; p=0.00038), diffuse large B-cell lymphoma (DLBC; p=0.00013), ccRCC (KIRC; p<0.0001), low-grade glioma (LGG; p=0.0107), prostate cancer (PRAD; p=0.00016) and thyroid cancer (THCA; p=0.0141) (Figure 27B-E).

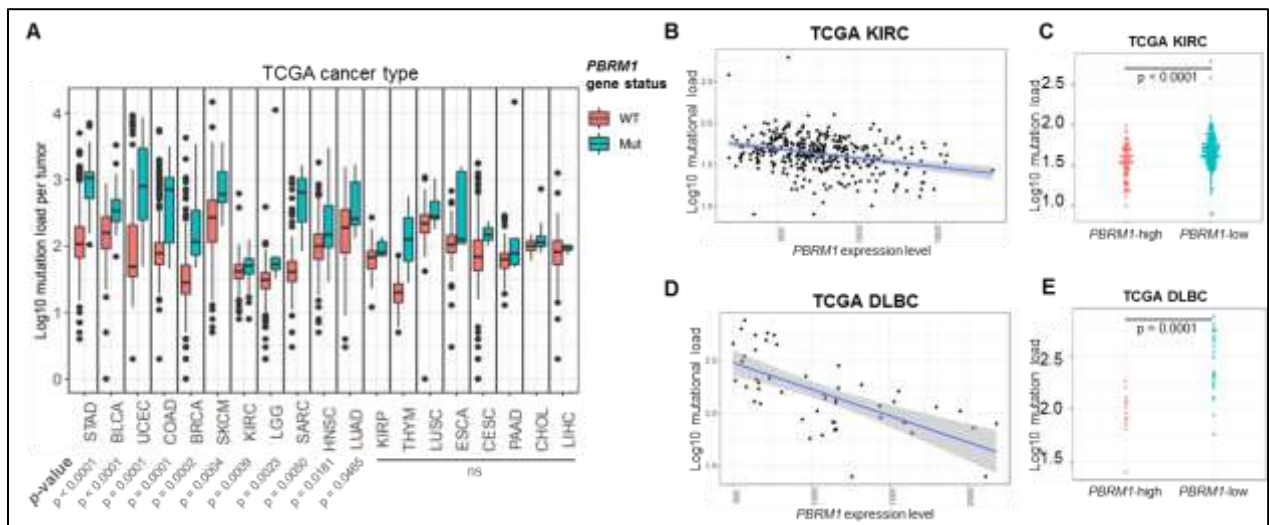


Figure 27. Mutational load of tumours according to PBRM1 mutation and expression. A, Log₁₀-valued mutational load in *PBRM1*-WT versus *PBRM1*-mutant (Mut) tumours from the 19 TCGA cancer types displaying at least 2 *PBRM1*-mutant samples; Mann-Whitney U test, cancer types with statistically significant differences with p-values < 0.05 are indicated. B,D, Scatter plots of the correlation between Log₁₀-valued mutation load and PBRM1 expression in RNA-Seq data from the TCGA. Samples from KIRC (B) and DLBCL (D) are shown; KIRC (N = 343; Pearson correlation = -0.20; p-value < 0.0001), DLBCL (N = 48; Pearson correlation = -0.586; p-value = 0.0001). C,E, Log₁₀-valued mutational load in TCGA tumours with high or low PBRM1 expression in clear cell renal cell carcinoma (KIRC, C) and diffuse large B-cell lymphoma (DLBCL, E). Shown are two histotypes among the 6 displaying significant differences between groups with p-values < 0.05; Mann-Whitney U test. (BRCA, p = 0.0003756; DLBC, p = 0.0001318; KIRC, p = 0.0000002; LGG, p = 0.0107637; PRAD, p = 0.0001554; THCA, p = 0.0140876). PBRM1-high and -low groups were defined as 25% and 50% of samples displaying the highest or lowest PBRM1 expression in RNAseq data respectively, as in Shen et al ¹⁰⁹.

These results indicate that PBRM1 defects associate with increased genomic instability which contributes to enhance mutational burden in human tumours, but does not associate with profound HR defects.

d. Micronuclei formation

A micronucleus is a small nucleus detached from the main nucleus of one cell due to its misincorporation during cell division ¹¹⁰. Micronuclei formation reflects genomic and chromosomal instability ¹¹¹. Micronuclei can arise from a clastogenic event (a chromosomal break that leads to a fragment of chromosome dissociated from the

rest of the nucleus during mitosis) or from an aneugenic event (a whole chromosome is lost during anaphase through irregularity with the spindle apparatus).

As we identified PBRM1 defect as a probable source of genomic instability in tumour samples (Figure 27), we intended to validate this finding in multiple isogenic cell lines using the micronucleus assay. We therefore enumerated the fractions of *PBRM1*-KO or -WT cells containing a micronucleus next to the main nucleus during interphase after fluorescent labeling with the PicoGreen® dye, which is highly specific for double-stranded DNA.

We consistently observed, across all cellular models tested, that *PBRM1*-KO cells displayed a significantly higher baseline rate of micronucleus-positive cells, as compared to their *PBRM1*-WT counterpart (Figure 28), which was again in favor of an increased genomic instability driven by PBRM1 loss.

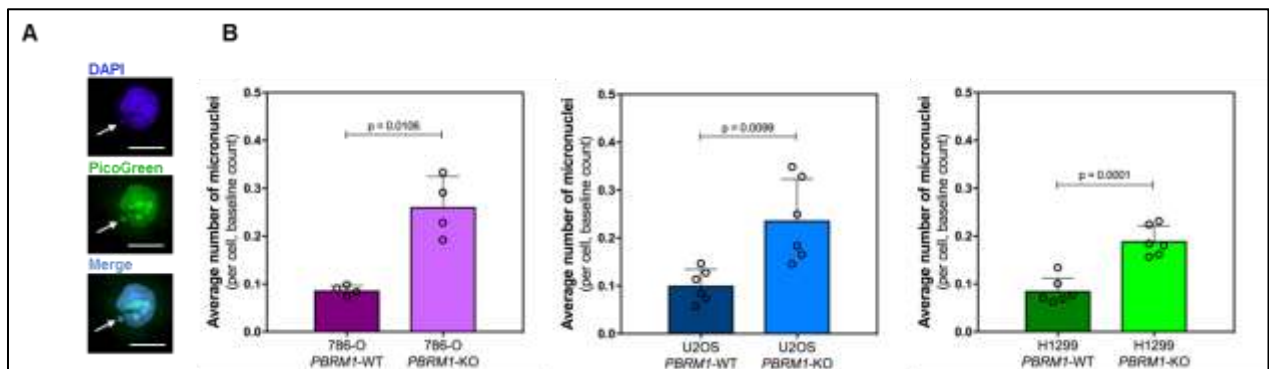


Figure 28. Micronuclei quantification according to PBRM1 status. A, Representative immunofluorescence images of a micronucleus-positive 786-O *PBRM1*-KO cell. Micronucleus is indicated with an arrow. Scale bar: 20 μ M. B, Automated quantification of baseline levels of micronuclei in 786-O, U2OS and H1299 *PBRM1*-isogenic cells. Shown is the number of micronuclei per cell normalized to the *PBRM1*-WT condition. Mean \pm SD, n = 3, Kruskal-Wallis test and post hoc Dunn's test

e. Mitotic spindle abnormalities

As micronuclei are generated during mitosis regardless of the initiating event (even clastogenic or aneugenic)¹¹², we generated a new cellular system stably expressing a mCherry-labeled histone H2B so that we could observe the nuclear aspect of the cells during mitosis under epifluorescence microscopy, without being too toxic with a permeable dye. To do so, we used confocal super-resolution time-lapse microscopy on synchronized 786-O H2B-mCherry-labeled *PBRM1*-KO and -WT cells. We pictured four fields per condition every 15 minutes for 48 hours using a Leica HR-SP8 confocal microscope in the mCherry channel, at 40X magnification. After creating the associated movies, we analyzed each mitosis.

We observed that *PBRM1*-KO cells needed on average almost twice more time to complete mitosis, from the time of prophase to the time of telophase (median duration: 45 vs 70 min in *PBRM1*-WT and -KO cells, respectively, $p < 0.0001$, two-way ANOVA) (Figure 29A,B). This was mainly due to difficulties for chromosomes to rapidly and appropriately forming the metaphase plate during prometaphase, as about half of *PBRM1*-KO cells took at least 45 minutes to align at the plate with "lagging" pre-metaphasic chromosomes, against only 2.1% of *PBRM1*-WT cells ($p = 0.0041$) (Figure 29C). Afterwards, we did not observe significant abnormalities during the division itself (anaphase), except for an increased rate of chromatin bridges observed during anaphase of *PBRM1*-KO cells (Figure 29D); although the formation of an anaphase bridge was not necessarily linked to the further formation of a micronuclei in daughter cells, and conversely, micronuclei often resulted from apparently-normal mitosis.

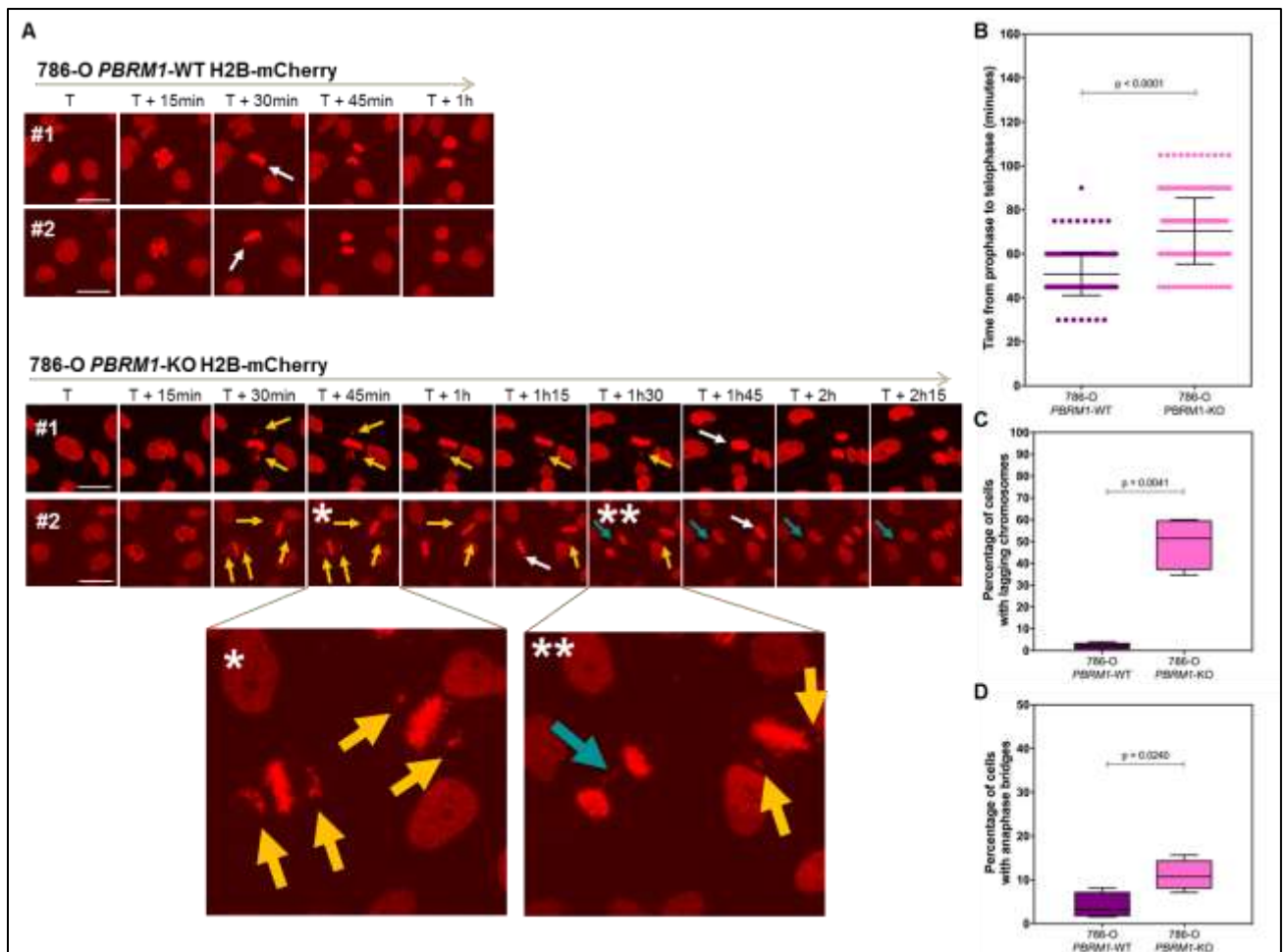


Figure 29. Mitosis abnormalities observation. A, Representative time-lapse microscopy images of mitosis over time (pictured every 15 minutes) from prophase to telophase of H2B-mCherry stably expressing 786-O *PBRM1*-WT (top) and -KO (bottom) cells. Two independent fields are shown for each cell line. White arrows indicate metaphase plates; yellow arrows indicate pre-metaphase lagging chromosomes; blue arrows indicate anaphase bridges. Scale bar: 20 μ m. B, Fraction of abnormal mitosis occurring in synchronized 786-O *PBRM1*-isogenic cells stably expressing a histone H2B mCherry-label and observed during 48 h using confocal time-lapse videomicroscopy. Beeswarm plot showing the time from prophase to telophase in 786-O *PBRM1*-WT and -KO cells. Mean \pm SD; n = 4 fields per condition, each corresponding to at least 200 mitosis; Welch's t-test. C,D, Box-and-whisker plots displaying quantification of the fraction cells with anaphase bridges (C), or pre-metaphase lagging chromosomes (D) detected in 786-O *PBRM1*-WT and -KO cells. Boxes indicate median, lower and upper quartiles; whiskers indicate the 5th to 95th percentile range; n = 4; Welch's t-test.

As PBRM1 has previously been shown to co-localize at kinetochores of mitotic cells, we used immunofluorescence labeling of PBRM1 and Centromere protein E (CENP-E) – an important component of the kinetochore involved in the connections between kinetochores and the spindle microtubules¹¹³ – in our 786-O H2B-mCherry model. We first observed that during interphase, PBRM1 was primarily localized within the

nuclei as expected, with more intense signal nearby nucleoli (Figure 30A). In mitotic cells, PBRM1 localization was enriched at the spindle poles, as previously described (Figure 30B)⁹³. We observed that even in the absence of PBRM1, CENP-E could be identified at kinetochores of lagged chromosomes (Figure 30C), suggesting that PBRM1 may not be required for the recruitment of CENP-E.

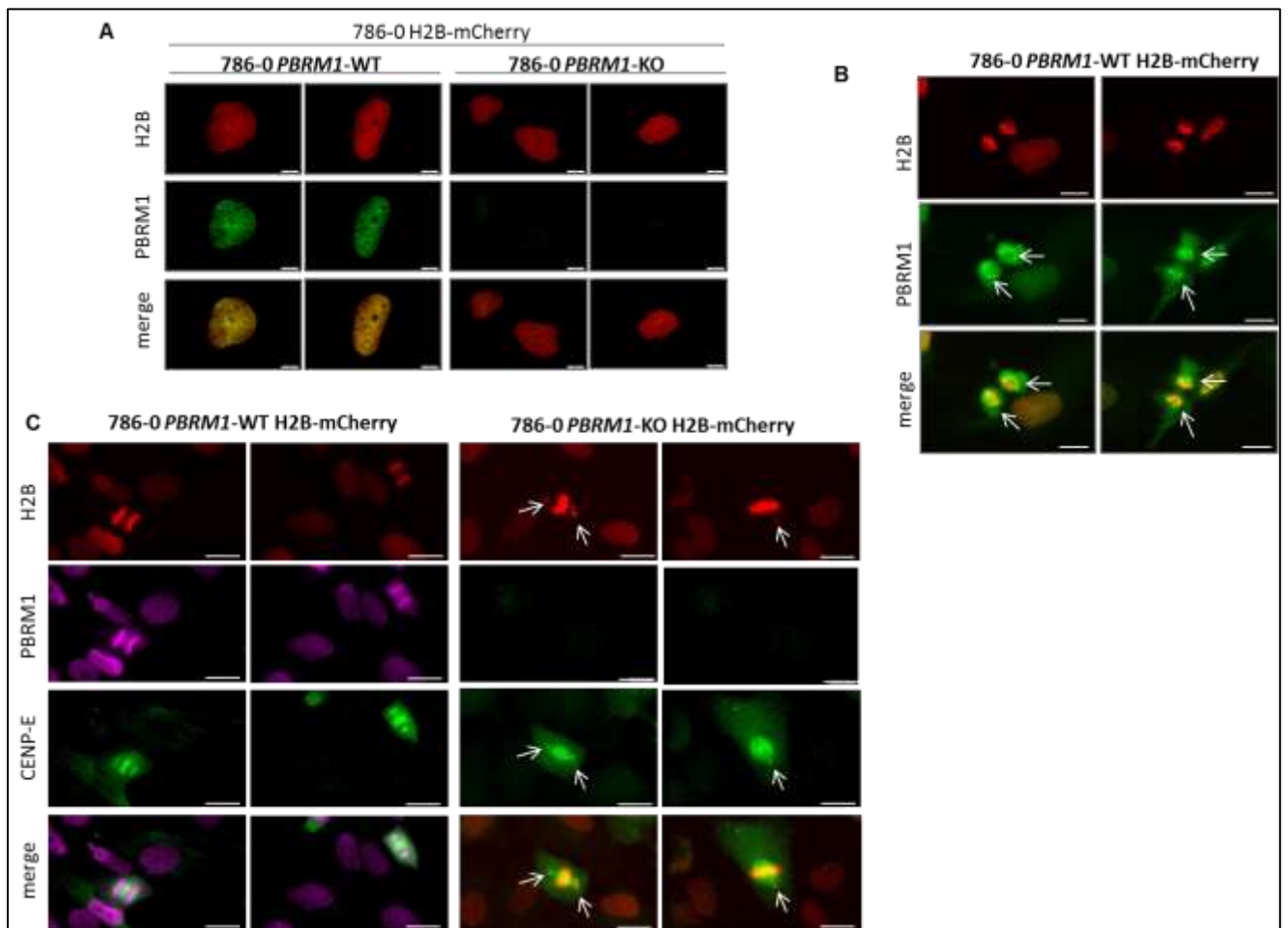


Figure 30. PBRM1 immunofluorescent labeling. A, Representative immunofluorescent images of H2B-mCherry labeled 786-O *PBRM1*-isogenic cells during interphase. H2B (red) and PBRM1 (green) expression are shown. Scale bar: 20 μ m. B, Representative immunofluorescent images of H2B-mCherry labeled 786-O *PBRM1*-WT cells during interphase. H2B (red) and PBRM1 (green) expression are shown. Arrows indicate more intense labeling of PBRM1. Scale bar: 20 μ m. C, Representative immunofluorescent images of H2B-mCherry labeled 786-O *PBRM1*-isogenic cells during mitosis. H2B (red), PBRM1 (purple) and CENP-E (green) expression are shown. Arrows indicate prometaphasic lagged chromosomes. Scale bar: 20 μ m.

Micronuclei can also result from supernumerary spindle poles or unfocused microtubule minus ends ¹¹⁴. We therefore investigated whether PBRM1 loss could impact the formation of bipolar spindle or the polymerization of mitotic microtubules, and therefore also prevent the chromosomes from reaching the metaphase plate. We used SiR-Tubulin to stain microtubules as a cell-permeable compound that is non-toxic for living cells and we repeated time-lapse confocal microscopy with an additional channel (green). We observed that the spindle poles formation and the microtubule polymerization were correctly initiated in the absence of PBRM1 (Figure 31A), which is in favor of a role for PBRM1 to attach the kinetochore onto the microtubule, rather than for the cytoskeleton organization itself.

Interestingly, the differential expression of kinetochore-related proteins (list retrieved from *Maiato et al.* ¹¹⁵) evaluated in the proteomic analysis of the HAP1 *PBRM1*-KO cells compared to -WT cells showed a consistent down-regulation of inner and outer kinetochore-related proteins in *PBRM1*-KO cells and conversely, a predominantly up-regulation of centromeric heterochromatin-related proteins (Figure 31B), suggesting that PBRM1 loss could disrupt the protein balance or recruitment at kinetochore sites.

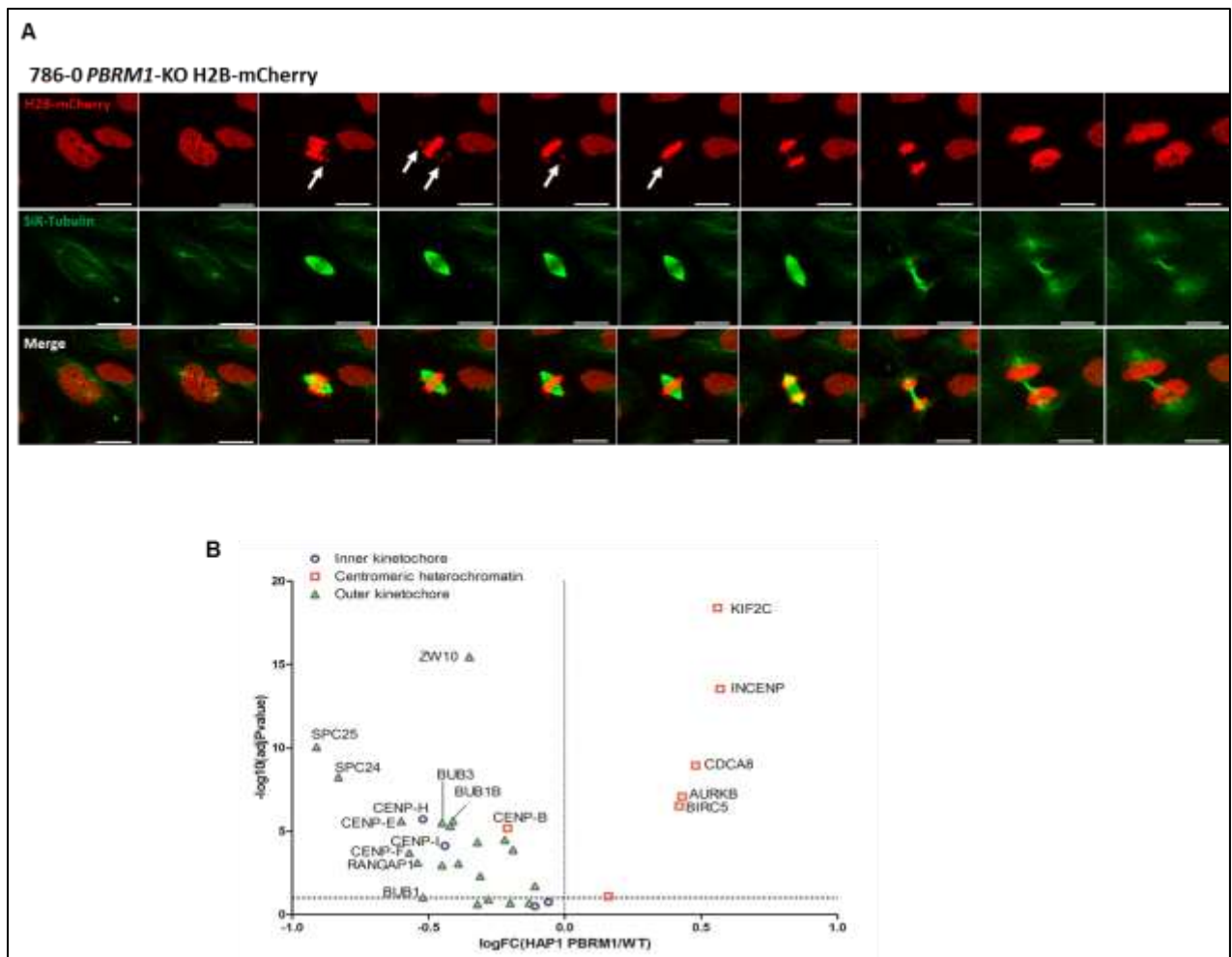


Figure 31. Spindle poles observation. **A**, Representative time-lapse microscopy images of mitosis over time (pictured every 7 minutes) from prophase to telophase of H2B-mCherry stably expressing 786-O *PBRM1*-KO cells transfected with SiR-Tubulin. H2B (red), tubulin (green) and merge are shown. Arrows indicate the presence of prometaphasic lagged chromosomes. Scale bar: 20 μ m. **B**, Volcano plot showing significantly (FDR q-value < 0.01) dysregulated proteins in HAP1 *PBRM1*-KO cells, as compared to *PBRM1*-WT cells, assessed by mass spectrometry. Kinetochore-associated proteins are shown (blue: inner kinetochore; red: centromeric heterochromatin; green: outer kinetochore).

Although we could not observe precisely the direct mechanism by which micronuclei were generated in *PBRM1*-KO cells through the observation of abnormal mitosis; yet we identified that the defect in *PBRM1* prolongs the duration of mitosis and in particular, the migration of chromosomes till the metaphase plate, possibly via destabilized kinetochore-microtubule interaction which is a known source of micronucleus generation. This is consistent with recent data that describe that *PBRM1* is a tubulin-binding protein that recognizes α -tubulin trimethylated on K40 during

mitosis⁹³. Altogether, this suggests a role for PBRM1 in establishing robust kinetochore-microtubule contacts which are required for correct chromosomal segregation and maintenance of genomic stability.

f. Impact of PBRM1 loss on the SWI/SNF stoichiometry

Synthetic lethal relationships and epigenetic antagonisms were previously described with defects in other SWI/SNF subunits, in particular in SMARCB1, SMARCA4 and ARID1A¹¹⁶⁻¹¹⁸. Notably, ARID1A deficiency has already been linked to DNA damage repair abnormalities and PARPi sensitivity^{116,117}. We therefore evaluated whether PBRM1 deficiency could directly influence the composition of the SWI/SNF complexes, including of ARID1A, to ensure that the PBRM1-PARP1 synthetic lethal relationship is primarily linked to PBRM1 loss, and not to a somewhat secondary effect on ARID1A expression.

To do so, we immunoprecipitated a SWI/SNF core subunit that is present in all forms of complexes, namely SMARCC2, using our four *PBRM1*-isogenic models, and then blotted subunits of interest (Figure 32). We confirmed that SMARCB1, SMARCA4 and ARID1A were correctly incorporated into the complex, even in the absence of PBRM1, which is in favor of a primary effect of PBRM1 loss in the sensitivity to PARPi.

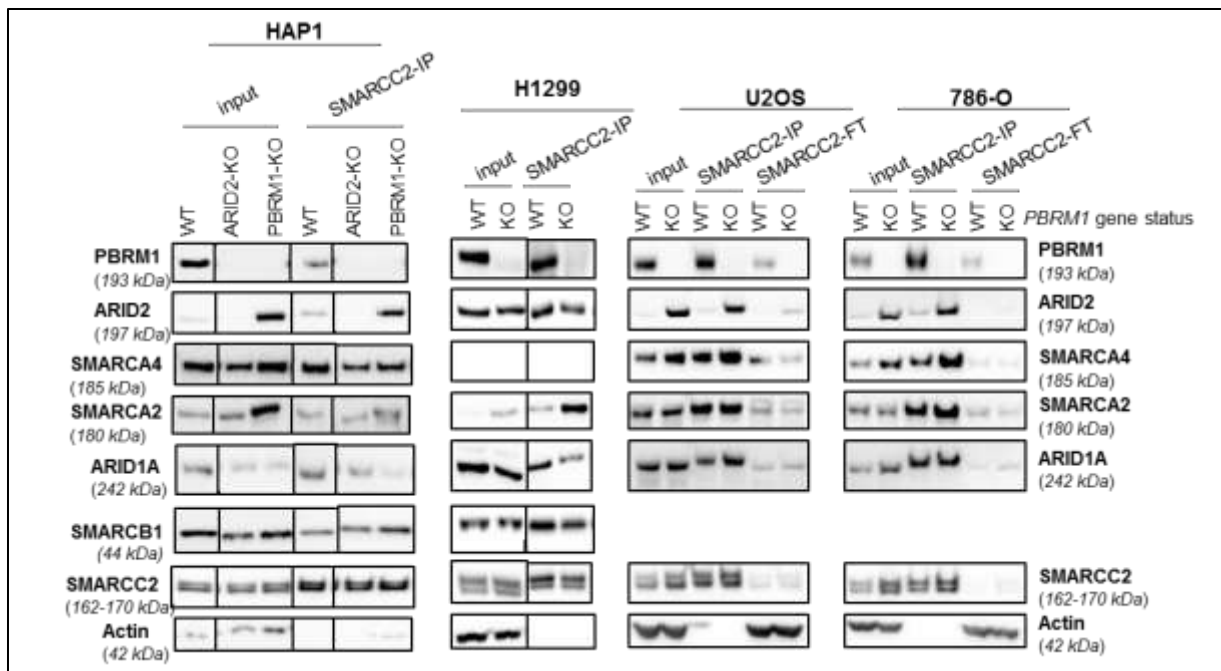


Figure 32. Western blot of selected SWI/SNF subunits expressions on total cell extracts following immunoprecipitation of SMARCC2 in HAP1 *PBRM1* and *ARID2*-isogenic cells, and in H1299, U2OS and 786-O *PBRM1*-isogenic cells. Input, immunoprecipitated (IP) and flow-through (FT) fractions are shown.

Interestingly and consistently with recent reports^{119,120}, we observed an increase in ARID2 expression in *PBRM1*-KO cells in the HAP1, U2OS and 786-O models, suggesting that ARID2 expression might partly buffer the loss of PBRM1 in these models. These observations were further validated using the whole transcriptomic and proteomic analysis of the HAP1 *PBRM1*-isogenic model (*data not shown*).

We also consistently noticed a moderate increase in SMARCA2 expression in *PBRM1*-KO cells, in particular in the *SMARCA4*-mutant H1299 cell lines. Importantly, SMARCA4 was not found to be essential for the incorporation of the PBAF specific subunits (PBRM1 and ARID2) into the complex within this H1299 model. Also as previously reported in *Schick et al.*, the *ARID2*-KO HAP1 cell line did not express PBRM1 either¹¹⁹.

g. Nucleolus fragmentation

In the proteomic analysis of HAP1 *PBRM1*-isogenic model, we identified a significant deregulation in several processes related to rRNA processing and transcriptional features following loss of PBRM1 among the top 20 of the most under-expressed biological processes (Figure 18) (GO terms: "ribosome biogenesis", ranked #3, NES = -2.4, adjusted pval = 0.0078; "rRNA processing", ranked #5, NES = -2.31, adjusted pval = 0.0078, "ribonucleoprotein complex biogenesis", ranked #8, NES = -2.25, adjusted pval = 0.078; "rRNA metabolic process", ranked #10, NES = -2.24, adjusted pval = 0.0078; "DNA-templated transcription, elongation", ranked #18, NES = -2.07, pval = 0.0078). In addition, using immunofluorescent labeling of PBRM1, we observed that its nuclear localization was more intense nearby nucleolar structures during interphase (Figure 30A, 33A), which is in line with previous reports of PBRM1 presence in actively transcribed genomic area^{88,89}.

In H2B-mCherry expressing 786-O *PBRM1*-KO cells, we noticed that nuclei presented a different phenotype than -WT cells, notably regarding the number and size of nucleoli. We therefore used an antibody directed against fibrillarin to specifically visualize nucleolar structures in our H2B-mCherry 786-O *PBRM1*-isogenic model. We identified that *PBRM1*-KO 786-O cells presented an increased absolute number of nucleoli per cell compared to -WT cells (*PBRM1*-WT: mean 4.6 nucleoli/cell; *PBRM1*-KO: mean 7.2 nucleoli/cell; $p < 0.0001$; unpaired t-test) (Figure 33B-C). When analyzing the foci sizes by automatic quantification using ImageJ software, we observed that the fibrillarin-positive foci sizes were significantly smaller in *PBRM1*-KO cells compared to -WT cells ($p < 0.0001$) (Figure 33D).

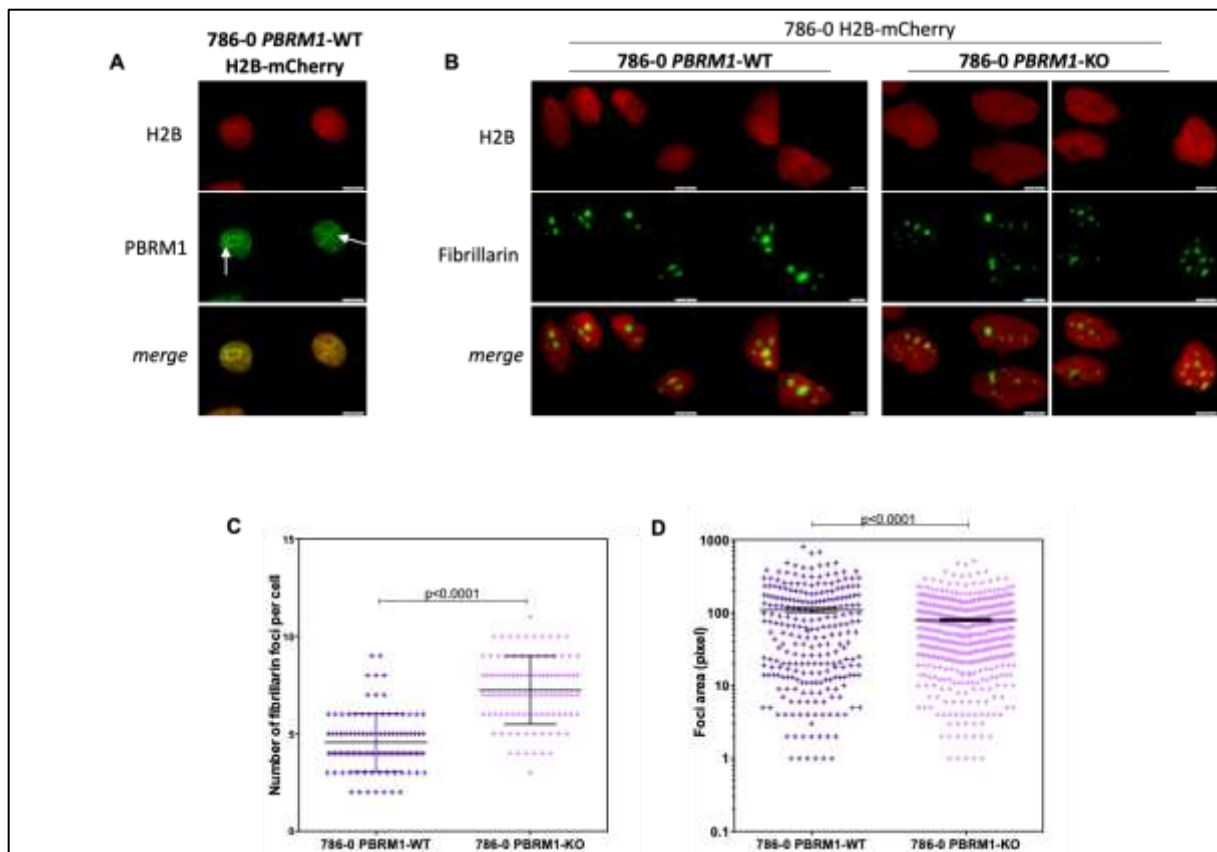


Figure 33. Nucleoli fragmentation observation. A, Representative immunofluorescence picture of H2B (red) and PBRM1 (green) expressions in 786-O H2B-mCherry *PBRM1*-WT cells during interphase. Arrows indicate nucleolar structures. Scale bar: 20 μ m. B, Representative immunofluorescence picture of H2B (red) and fibrillarin (green) expressions in 786-O H2B-mCherry *PBRM1*-isogenic cells during interphase. Scale bar: 20 μ m. C, Absolute number of fibrillarin foci per cell in 786-O *PBRM1*-isogenic cells. D, Automated quantification of fibrillarin foci sizes in 786-O *PBRM1*-isogenic cells.

Such nucleolar fragmentation to “multilobed nucleoli” was recently linked to the loss of H3K9 dimethylation histone mark (H3K9me2) and R-loop accumulation, that also may reflect genomic instability¹²¹. Importantly, the H3K9me2 histone mark was previously shown to be possibly recognized by the pairing of a BAH domain and a chromodomain¹²². We can therefore hypothesize that PBRM1 (which harbor two BAH domains) might be required to guide SWI/SNF over H3K9me2 histone marks, in collaboration with chromodomain-containing subunits (SMARCC1, SMARCC2). Of note, H3K9 dimethylation status is related to H3K14 acetylation status in highly transcribed genomic area¹²³, which is the main histone mark recognized by PBRM1;

PBRM1 might therefore bind to H3K14ac through its bromodomains, and to the adjacent H3K9me2 through its BAH domains.

h. Replication fork progression

Faithful genome replication is also essential for genetic stability and must be accurately ensured despite the presence of damaged DNA. When the replication machinery detects a DNA damage, it often pauses for a brief moment and rapidly manages to bypass the damage independently from any checkpoint-activation and without creating a mutation¹²⁴. However, replication forks can also stall at lesion sites, notably when the repair machinery cannot adequately repair the damage. In such case, single-stranded DNA accumulates at the lesion sites, which activates a checkpoint-dependent cellular response, and eventually results in a DSB formation. This also results in reduced fork velocity at affects all forks, not only those encountering a stalling event¹²⁴.

We already identified that *PBRM1*-KO cells presented increased DNA damage response signaling (Figure 26), we therefore investigated whether this baseline higher rate of DNA DSBs could be linked to increased replication stress resulting in stalled replication forks. Using automated immunofluorescence quantification of Replication Protein A2 (RPA2) foci after fixation of the cells in the absence of PARPi, we observed a significantly increased number of RPA2 foci in 786-O *PBRM1*-KO cells compared to –WT cells (Figure 34A). RPA2 is known to bind and stabilize single-stranded DNA that is formed upon DNA replication or upon DNA damage that may follow unresolved replication fork stalling¹²⁵, indicating that *PBRM1*-KO cells present increased single-stranded DNA exposure.

We further evaluated the expression of proteins implicated in the activation of the checkpoint – under their total and phosphorylated forms – by western blotting total

protein extracts from *PBRM1*-KO and -WT cells, from three independent isogenic models. We observed an increased expression and phosphorylation of ATR and ATM which however varied according to the cell type: 786-O *PBRM1*-KO cells over-expressed both ATM and ATR, HAP1 *PBRM1*-KO cells mainly over-expressed ATR, while U2OS *PBRM1*-KO cells mainly over-expressed ATM (Figure 34B).

To check whether these phenotypes had an impact on the replication fork rates, we performed DNA fiber combing after pulse-labeling the cells during 30 minutes with 100 μ M of CldU, rinsing and chasing with 100 μ M of IdU for another 30 minutes. To robustly analyze the forks speed, we considered only entire and definite origins of replication and excluded from the analysis forks occurring at the ends of the fibers that might have been randomly digested during the plug processing and might generate under-estimations of the actual fork rate (Figure 34C).

We found a significantly reduced replication forks velocity in *PBRM1*-KO cells of 786-O and U2OS models (Figure 34D; 786-O, mean speed of 0.51 kb/min for *PBRM1*-KO cells vs 0.71 kb/min for *PBRM1*-WT cells; U2OS, mean speed of 1.06 kb/min for *PBRM1*-KO cells vs 1.44 kb/min for *PBRM1*-WT cells; both $p < 0.0001$, Wilcoxon-Mann-Whitney test). This was however not reproduced in the H1299 model (Figure 34D), most likely due to the presence of SMARCA4-deficiency in this parental model - a genetic defect very recently reported to impair the replication fork progression ¹²⁶.

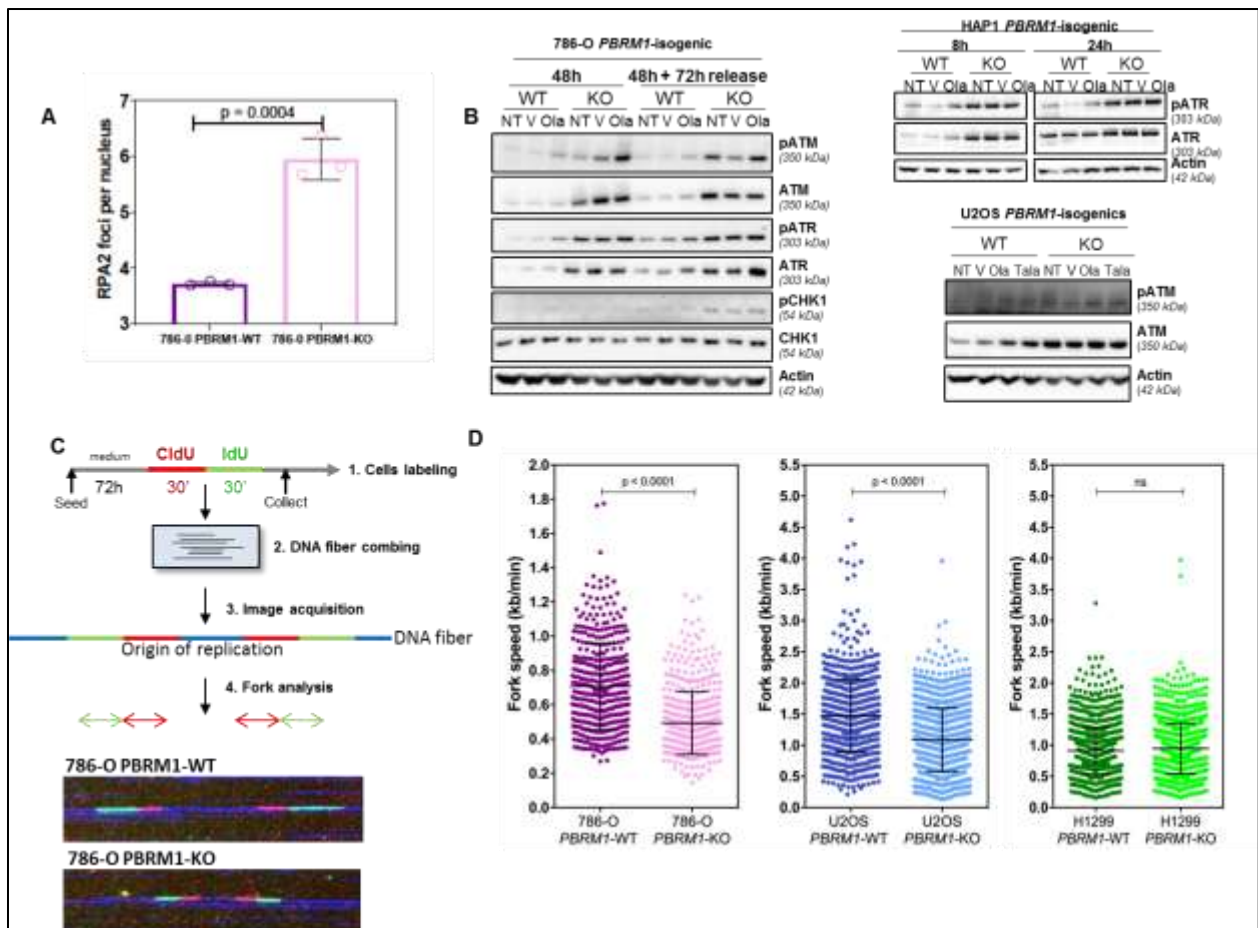


Figure 34. Replication stress assessment. **A**, Automated quantification of the baseline number of RPA2 foci per nucleus in 786-O *PBRM1*-isogenic cells. > 1500 nuclei per condition were analysed. Box-and-whisker plots show the average number of foci per nucleus. Boxes indicate median, lower and upper quartiles; whiskers indicate the 5th to 95th percentile range; $n = 3$, two-way ANOVA and post hoc Sidak's test. **B**, Western blot showing phosphorylated and total ATR and/or ATM and/or CHK1 in synchronized 786-O, HAP1 and U2OS *PBRM1*-isogenic cells at baseline and exposed to PARPi. 786-O: cells were exposed to 20 μM of olaparib during 48h, then released in fresh medium for 72h prior to harvesting. HAP1: cells were exposed to 50 nM of olaparib during 8h or 24h prior to harvesting. U2OS: cells were exposed to 10 μM of olaparib or 100 nM of talazoparib for 48h prior to harvesting. **C**, Schematic representation of the DNA fiber combing assay evaluating replication fork speed. Two representative origin of replication images are shown. **D**, Assessment of replication fork speed (kb/min) in 786-O, U2OS and H1299 *PBRM1*-isogenic cells. At least 800 forks per condition were analyzed. Mean \pm SD, each dot represents a single pulse; $n = 2$, Wilcoxon-Mann-Whitney test.

Altogether, these findings suggest that loss of PBRM1 is associated with increased replication stress, exhibited by increased single-stranded DNA exposure, activation of the replication checkpoint that leads to global slowing of replication forks progression. This is in line with our previous analysis of the proteomic landscape of HAP1 *PBRM1*-KO cells compared to -WT cells, which showed enrichment in down-

regulated processes related to DNA replication in a *PBRM1*-KO context (Figure 18) (GO term: "DNA replication", NES = -2.29, adjusted p-val = 0.0078).

i. Discussion

In this chapter, we identified that *PBRM1* loss leads to increased genomic instability, which interestingly, in our isogenic models, was not related to a defect in a DNA repair major protein, and particularly, in a protein belonging to the HR pathway. We however identified three mechanisms by which *PBRM1* deficiency may primarily contribute to increased genomic instability at almost all steps of the cell cycle: transcription perturbation, replication stress and mitosis abnormalities.

The role of *PBRM1* for cell cycle progression through mitosis is known since year 2000⁹², when it was first found to be localized at kinetochores of mitotic chromosomes, mirroring the fundamental role of RSC to progress through the cell cycle in yeast¹²⁷. The correlation between *PBRM1* deficiency and defective centromeric cohesion, hypersensitivity to DNA damage, increased frequency of chromosomal aberration and dynamic chromosomal instability in cancer has however been identified more recently⁸⁴, still without clearly identifying a causal connection. In this Chapter, we additionally identified that *PBRM1* loss impairs the migration of chromosomes to the metaphase plate during pro-metaphase without interfering with the polymerization/depolymerization of microtubules (Figure 29, 31), which is in line with recent data showing that *PBRM1* is required to anchor kinetochore-associated PBAF to α -tubulin during mitosis⁹³. Even though kinetochore-microtubule interaction defect is a known source of micronuclei formation, we could not observe a correlation between prolonged pro-metaphase with lagging chromosomes and further formation of a micronucleus in *PBRM1*-KO daughter cells. This suggests that the increased number of micronuclei observed in *PBRM1*-KO cells (Figure 28) might be preferentially resulting from a clastogenic event (for example, unresolved DNA

DSB) rather than a mitosis-related aneuploid event (chromosomal missegregation during anaphase).

The cell capacity to handle replication stress depends on the number and lengths of the replisome arrests^{104,124,128}. These pause sites can lead to replication fork collapses, which are great sources of DNA DSBs and chromosomal rearrangement, hence genomic instability. Therefore, the S-phase checkpoint activation prevents the over-acceleration or collapse of forks in case of high number of lesions. In our models, we observed that the increased DNA damage response signaling in *PBRM1*-KO cells in the absence of exogenous stress (Figure 26) was linked to increased RPA2 signaling and increased ATM and/or ATR protein expressions, respectively revealing accumulating single-stranded DNA and activation of cellular checkpoint during S phase of the cell cycle (Figure 34). This was subsequently linked to a reduced replication fork progression velocity, which reflects the overwhelming of the replication machinery facing a too large amount of damaged DNA – so called replication stress – in *PBRM1*-KO cells.

Except for ARID2 – and to a smaller extent to SMARCA2 – loss of PBRM1 did not drastically affect other SWI/SNF subunits' incorporation into the complex. This suggests that previous synthetic lethal relationships observed with deleterious mutations within *SMARCA4*, *SMARCB1* or *ARID1A* might not be generalized to PBRM1, including the previously described ARID1A-PARP_i synthetic lethal relationship^{116,117}.

Regarding these advances and the known role of PARP1 in managing replication stress, we hypothesized that PARP inhibitors might definitely disrupt the resolution of stalled replication forks in *PBRM1*-KO cells and therefore, guide deficient cells to death.

Chapter VI: PARPi exposure overtakes the capacity of PBRM1-deficient cells to maintain a phenotype suitable with survival

I. Introduction

As specified above, the main mechanism by which PARPi are known to sensitize cells is through synthetic lethality associated with HR deficiency, and particularly, DNA repair defect in BRCA1- or BRCA2-deficient tumours ¹²⁹. However, we showed that PBRM1-deficiency was not necessarily associated with HR defect in our isogenic cellular models, neither in tumour samples from the TCGA dataset; hence, could this not explain the vulnerability of *PBRM1*-KO cells to PARPi in our models.

Beyond being implicated in several DNA repair pathways, PARP1 and PARP2 orchestrate the protection of the replication fork upon replicative stress ¹³⁰. The stabilization of the forks stalled at damaged DNA sites is essential to prevent fork collapse and consecutive DNA DSB generation and genotoxic stress. As a consequence, it has been recently shown in ovarian and MYCN-overexpressing neuroblastoma models that replication stress-associated phenotypes can also sensitize cells to PARPi independently from HR-dependency ^{131,132}. This “other route” of PARPi-associated vulnerability is induced by persistent replication stress that eventually leads to replication catastrophe (following multiple fork collapses), accumulation of DNA damage, persistent checkpoint activation, and finally, cell death by PARPi-induced mitotic catastrophe.

Additionally to replication stress signals, we identified transcription stress signals in *PBRM1*-KO cells (Figure 18, 33), notably highlighted by nucleolar structure

fragmentations and deregulation of several transcriptional-related processes in the proteomic analysis of HAP1 cells. Co-occurrence of replication stress and transcriptional stress is observed notably when “replication-transcription collisions” occur – i.e. a conflict between a replication fork and a transcriptional bubble moving along the same DNA template^{133,134}. One of the physical outcomes of this collision is the formation of R-loops. R-loops are three-stranded nucleic acid structures that form when an RNA strand wrongly invades double-stranded DNA within the chromatin, resulting in a Watson-Crick RNA:DNA hybrid structure and a displaced section of non-hybridized single-stranded DNA¹³⁵⁻¹³⁷. R-loops occur naturally during replication and transcription, particularly in actively transcribed regions displaying “open” chromatin, although their accumulation is inaccurate and associates with increased DNA damage, especially under replication stress conditions.

In this final Chapter, we studied the response of *PBRM1*-KO cells following exposure to PARPi in order to estimate the implication of PBRM1 loss in the vulnerability to PARPi regarding both mitotic stress and replication/transcription stress, and therefore depicting a probable mechanism by which PBRM1 deficiency is synthetic lethal with PARPi. As replication fork velocity is tricky to assess and interpret following PARPi – due to the role of PARP in RF repair and progression, we directly focused on R-loop evaluation profiles of *PBRM1*-isogenic models with or without PARPi.

II. Results

a. DNA damage response following PARPi

We first evaluated the impact of increasing doses of PARPi on DNA damage response signaling via γ H2AX foci formation and further recruitment of RAD51 to damaged sites using immunofluorescence on three different *PBRM1*-isogenic models. We found a concentration-dependent increase in the number of both γ H2AX foci and RAD51 foci upon exposure to olaparib (Figure 35), which was significantly more intense in *PBRM1*-KO cells.

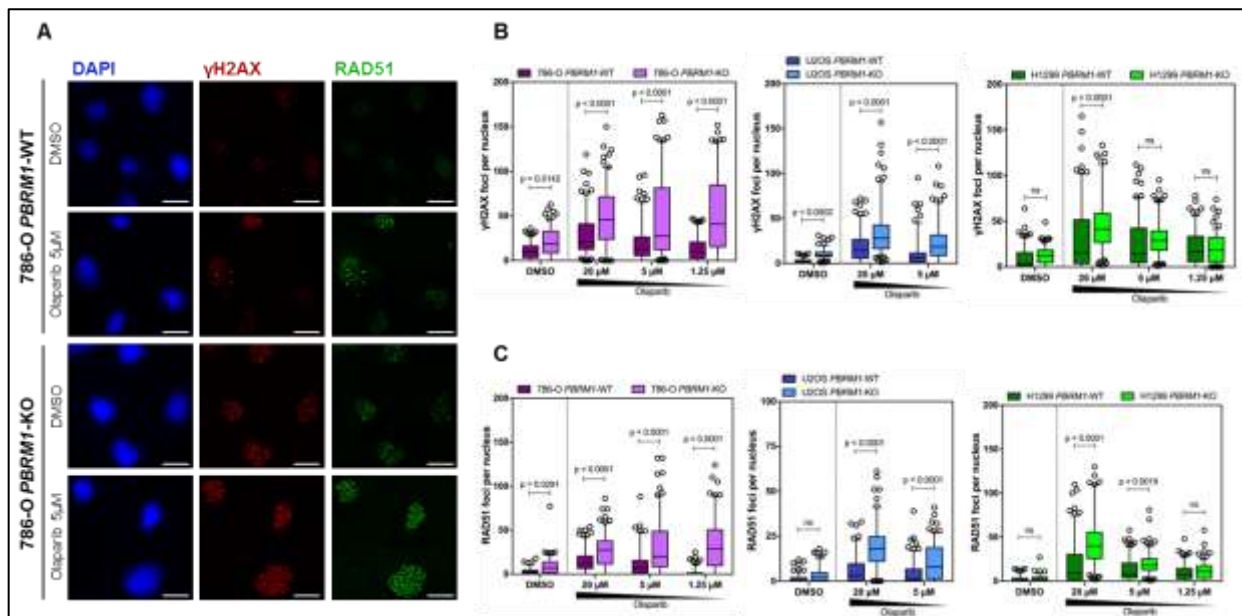


Figure 35. Quantification of γ H2AX and RAD51 foci after exposure to PARPi. A, Representative immunofluorescence images of γ H2AX (red) and RAD51 (green) foci in DMSO- and olaparib-treated 786-O *PBRM1*-isogenic cells. Cells were exposed to 5 μ M olaparib or DMSO (vehicle) for 48h prior to fixation. Scale bar: 20 μ m. B,C, Quantification of γ H2AX foci (B) and RAD51 foci (C) in 786-O, U2OS and H1299 *PBRM1*-isogenic cells exposed to increasing doses of olaparib (μ M) or DMSO for 48h. At least 150 nuclei per condition were analyzed. Box-and-whisker plots show the number of foci per nucleus. Boxes indicate median, lower and upper quartiles; whiskers indicate the 5th to 95th percentile range; outliers are shown as single data points; two-way ANOVA and post hoc Sidak's test.

We then investigated whether PARPi also increased the formation of micronuclei. We quantified the micronucleus-positive cells in three *PBRM1*-isogenic models, including

one model stably expressing a shRNA guided against PBRM1 and in our non-isogenic ccRCC cell lines. Exposure to two chemically-different clinical PARPi (olaparib and talazoparib) selectively led to an enhanced accumulation of micronuclei in PBRM1-defective cells of all models (Figure 36), with a magnitude that was equivalent to that caused by the clastogen agent mitomycin C (MMC), used as a positive control.

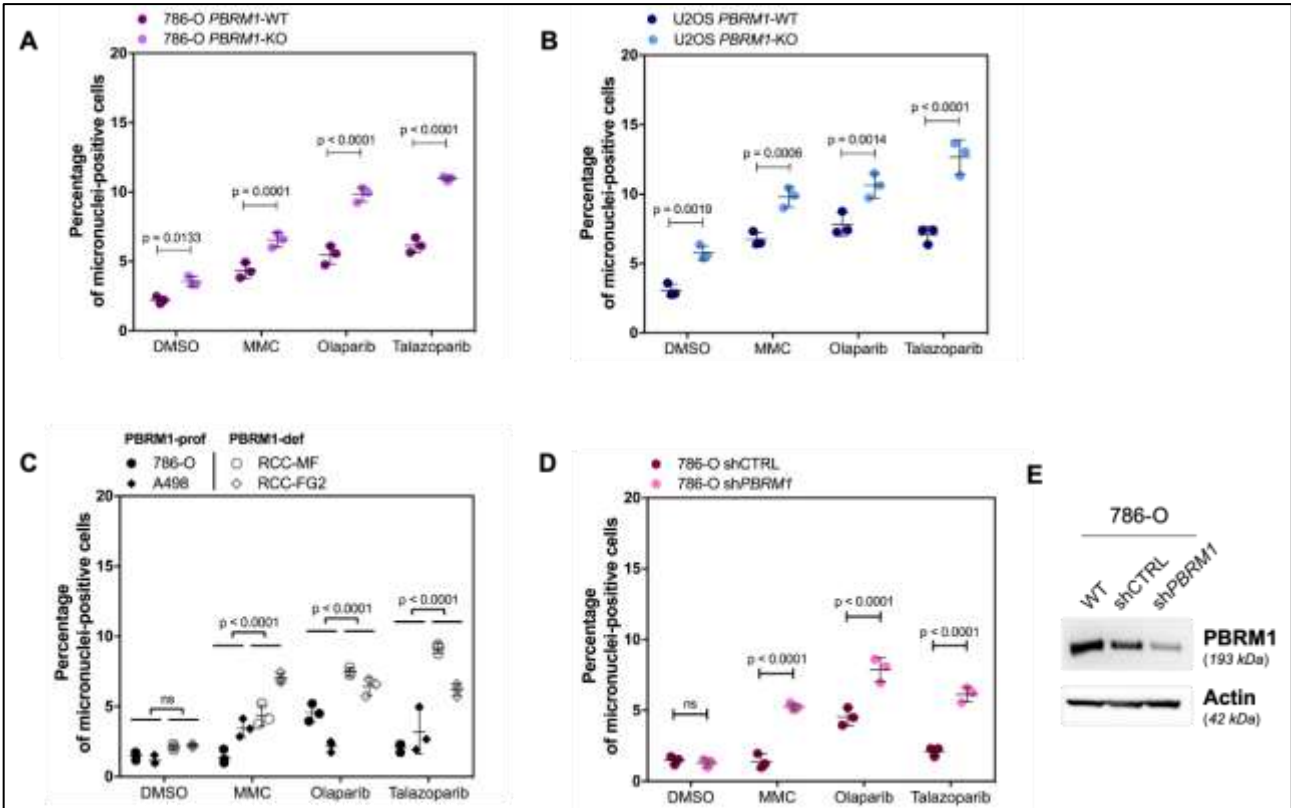


Figure 36. Micronuclei quantification after exposure to PARPi. A-D, Automated quantification of micronuclei-positive cells in 786-O (A) and U2OS (B) *PBRM1*-isogenic cell lines, in ccRCC non isogenic cell lines (C) and in 786-O after infection with a shRNA targeting *PBRM1* (D), as described in E. E, Western blot on total cellular extracts of *PBRM1* expression in 786-O after *PBRM1* silencing.

Interestingly, when extending these experiments in 786-O and U2OS *PBRM1*-isogenic models to the evaluation of other known inducers of DNA DSBs such as ionizing radiation (IR) or the topoisomerase II inhibitor etoposide, we did not observe a significant difference in viability, nor did we observe a reproducible and significantly

meaningful difference in the number of γ H2AX and RAD51 foci at early time points (< 5h) after IR (Figure 37).

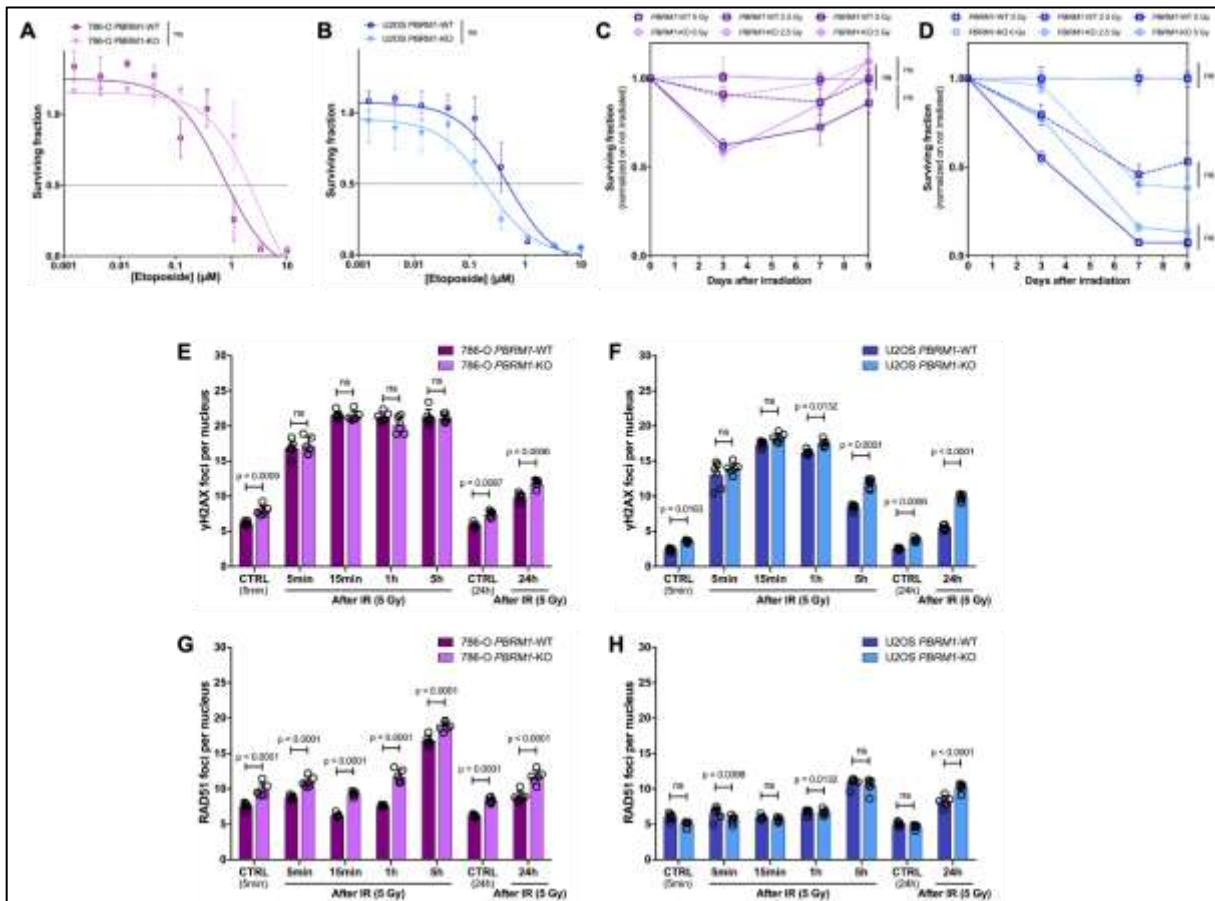


Figure 37. Sensitivity to other DSB-inducers. A,B, Dose-response survival curves of 786-O (A) or U2OS (B) *PBRM1*-isogenic models exposed to increasing concentrations of etoposide for 7 days in short-term survival assay. Mean \pm SD, n = 3; two-way ANOVA. **C,D,** Time-response survival curves of 786-O (C) and U2OS (D) *PBRM1*-isogenic cells exposed to irradiation at various doses (0 Gy, 2.5 Gy and 5 Gy) and cultured for 10 days in short-term survival assay. Mean \pm SD, n = 4; two-way ANOVA. **E,F,** Automated quantification of γ H2AX foci in 786-O (E) and U2OS (F) *PBRM1*-isogenic cells at various timepoints after irradiation. > 1500 nuclei per condition were analyzed. Mean number of foci per nucleus \pm SD, n = 3; two-way ANOVA and post hoc Sidak's test. **G,H,** Automated quantification of RAD51 foci in 786-O (G) and U2OS (H) *PBRM1*-isogenic cells at various timepoints after irradiation. > 1500 nuclei per condition were analyzed. Mean number of foci per nucleus \pm SD, n = 3; two-way ANOVA and post hoc Sidak's test.

b. Mitosis abnormalities

To determine whether mitosis abnormalities were exacerbated upon PARPi exposure, we performed time-lapse microscopy on synchronized H2B-mCherry expressing 786-

O *PBRM1*-isogenic cells during 48 hours of contact with 10 μ M of olaparib. Although we could observe mitotic catastrophes in olaparib-treated fields (Figure 38A), we could not rigorously quantify them over the 48 hours period of observation time (cells disappearing from the objective field or process not completed at the end of observation). However, we were able to quantify mitosis that completed the process, and observed a significantly increased time of mitosis upon olaparib exposure compared to DMSO, independently from *PBRM1* status (Figure 38B). The fractions of prometaphasic lagged chromosomes and anaphase bridges were unchanged following the PARPi treatment in both cell lines. These observations suggest that *PBRM1* deficiency-associated particular vulnerability to PARPi is not due to exacerbated mitotic defect, and the mechanism underlying this synthetic lethal relationship is likely to be interphase-specific.

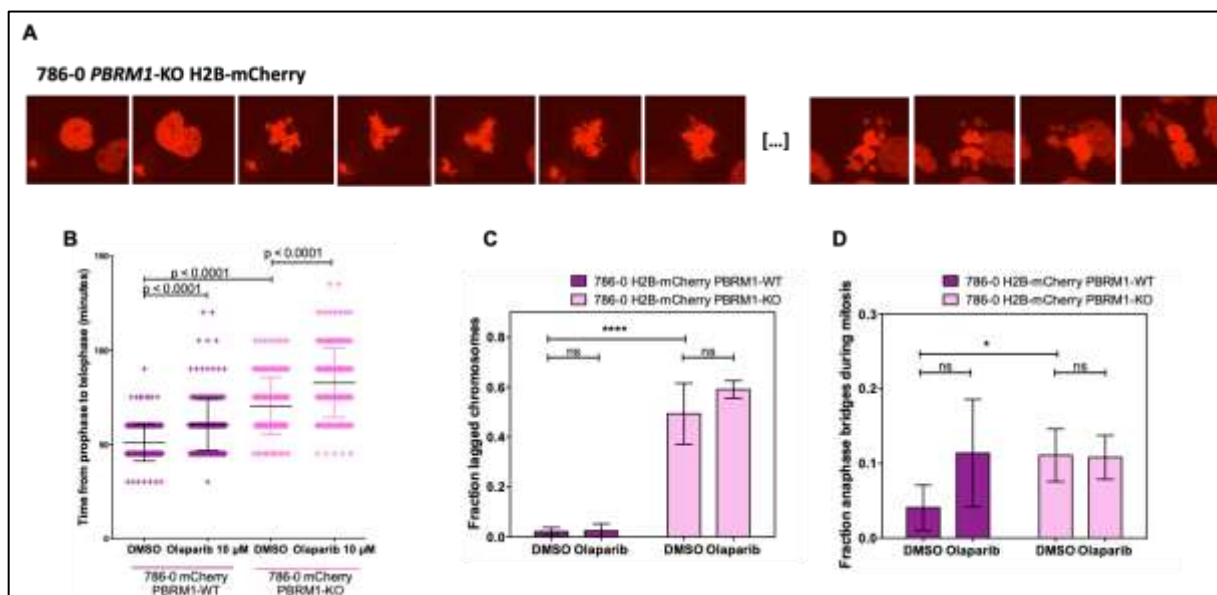


Figure 38. Mitosis abnormalities after exposure to olaparib. A, Time-lapse microscopy pictures of a representative mitotic catastrophe following treatment with 10 μ M of olaparib in a 786-O *PBRM1*-KO cell. Picutures were taken every 15 minutes. [...] indicates that several pictures were skipped, as the whole process took approximately 10 hours. **B,** Mitosis duration from time to prophase to time to telophase of 786-O H2B-mCherry *PBRM1*-isogenic cells observed during 48 hours in contact with 10 μ M of olaparib or vehicle (DMSO). **C,D,** Fractions of prometaphasic lagged chromosomes (C) and anaphase bridges (D) in 786-O H2B-mCherry *PBRM1*-isogenic cells observed during 48 hours in contact with 10 μ M of olaparib or DMSO

c. R-loop quantification

Because PBRM1 has a role in transcription and because we observed that *PBRM1*-KO cells presented several markers associated with R-loop accumulation, including (i) increased signals of RPA-bound single-stranded DNA, (ii) enhanced ATM signaling which is involved in R-loop resolution¹³⁸, (iii) enhanced PARPi sensitivity that was not linked to HR deficiency or to increased sensitivity to frank DNA DSBs or to exacerbated mitotic defects, (iv) disorganized nucleolar structures which are hot-spots of R-loop generation¹²¹, we hypothesized that *PBRM1*-deficient cells may present increased R-loop formation.

We performed DNA:RNA immunoprecipitation sequencing (DRIP-Seq) on independent duplicates of 786-O and H1299 *PBRM1*-isogenic models, in the presence and absence of PARPi (talazoparib), using the S9.6 monoclonal antibody, which is highly specific for RNA:DNA hybrids (Figure 39A). Immunoprecipitated DNA fragments were sequenced and aligned to the reference genome to identify and quantitatively compare sequences enriched in R-loops (peak calling) in each condition. Input and RNase H-treated conditions were used to evaluate the specificity of S9.6-associated peaks. Duplicates showed a high reproducibility, as illustrated by the Principal Component Analysis (PCA) of all cell lines, and negative controls showed a satisfying reduction of the signals (Figure 39B-D).

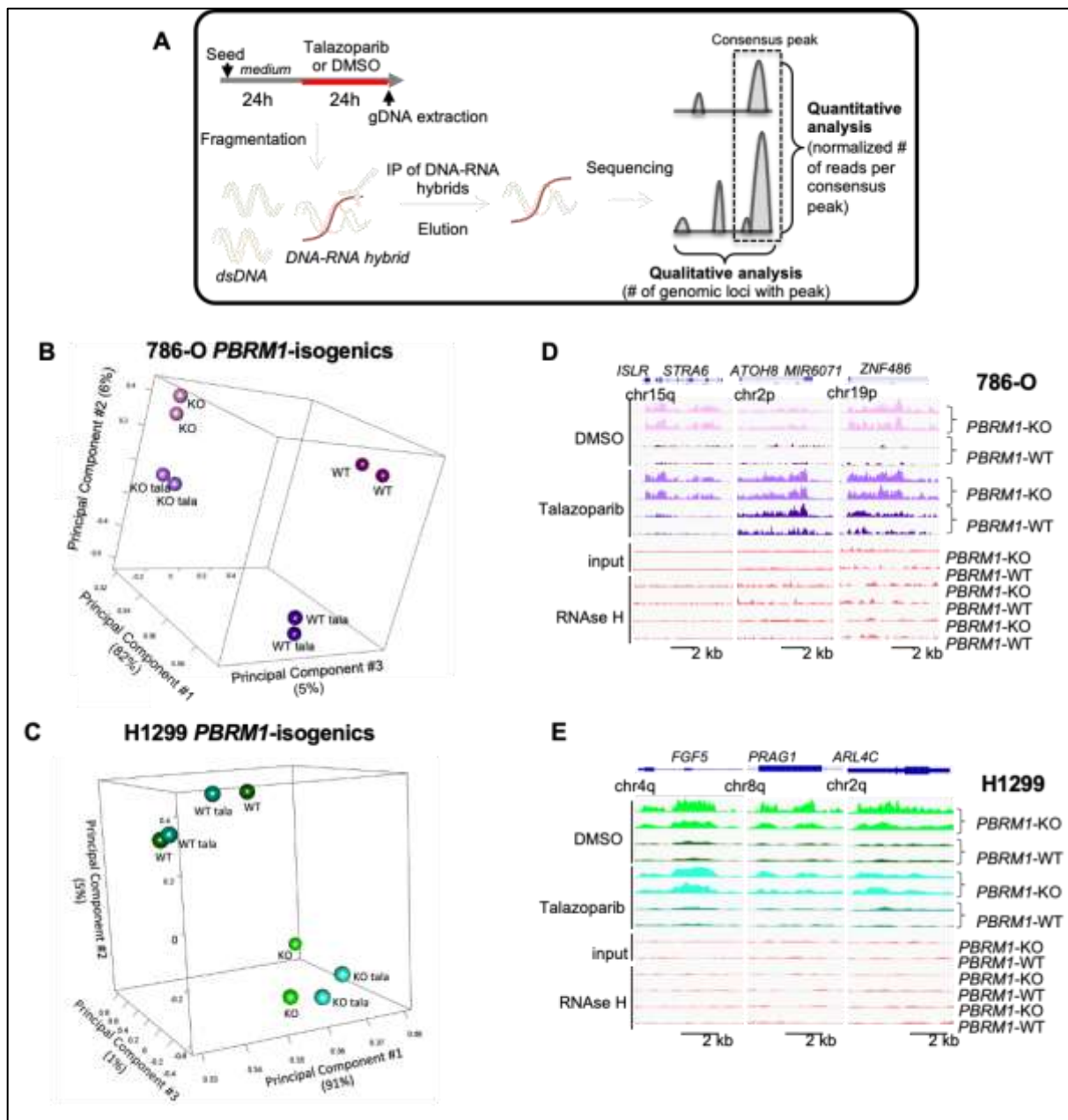


Figure 39. DRIP-seq analysis of *PBRM1*-isogenic models. A, Schematic representation describing the DRIP-Seq analysis performed on independent duplicates of 786-O and H1299 *PBRM1*-WT and -KO isogenic models. Cells were exposed to talazoparib (786-O, 0.5 μ M; H1299, 1 μ M) or DMSO for 24 h prior to DNA extraction. R-loops were immunoprecipitated using the S9.6 monoclonal antibody that recognizes DNA:RNA hybrids. Schematic of the qualitative and quantitative analyses performed on consensus peaks is depicted. B,C, First, second and third components analysis (PCA) with the percentage of total variance explained by each component. For each 786-O (B) or H1299 (D) replicate, normalized read counts of all binding sites were considered. D,E, Representative IGV (Integrative Genomics Viewer) tracks of genomic loci with DRIP-Seq peaks in 786-O (D) and H1299 (E) *PBRM1*-isogenic cell lines, in the presence or absence of talazoparib; input and RNase H treatment are shown as negative controls.

We then quantified the number of genomic regions associated with DRIP-Seq peaks to assess R-loop enrichment at specific genomic loci. We first observed that *PBRM1*-KO cells displayed almost twice more genomic loci associated with R-loop enrichment than *PBRM1*-WT cells (Figure 40A,B). The specific regions found to present R-loops in *PBRM1*-WT cells were often shared with *PBRM1*-KO cells (>90%); but conversely, about half of specific regions presenting R-loops in *PBRM1*-KO cells were free from R-loops in -WT cells, suggesting that PBRM1-loss may weaken certain regions of the genome to the formation of R-loops. When looking more precisely at these regions, we identified that *PBRM1*-KO cells presented increased accumulation of DRIP-seq peaks particularly in intronic regions (Figure 40C,D).

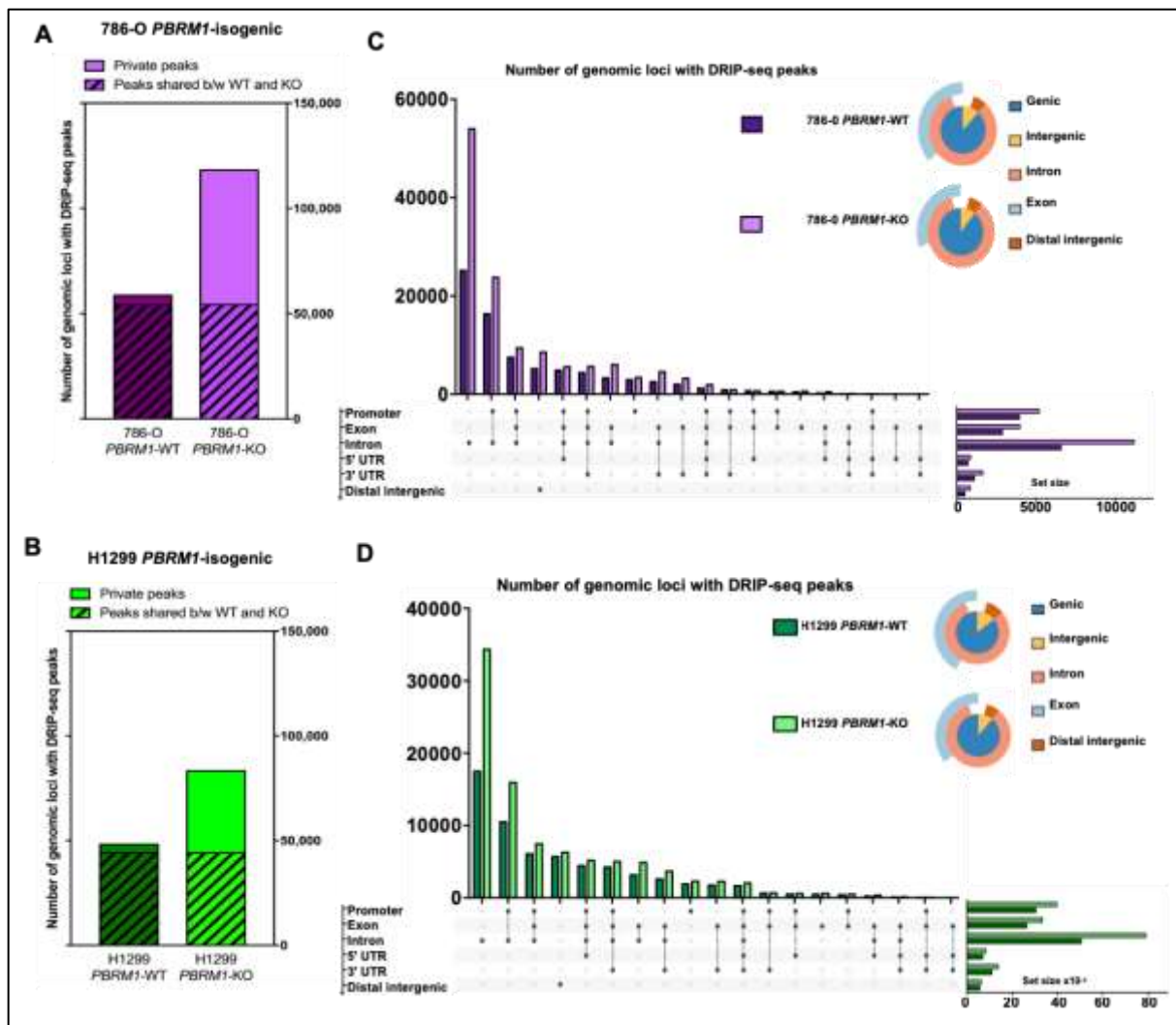


Figure 40. Genomic localisations of DNA-RNA hybrids according to PBRM1 status. A,B, Bar plots displaying the baseline number of genomic loci with DRIP-Seq peaks in merged replicates of 786-O (A) or H1299 (B) *PBRM1*-WT and -KO cells. Connected or overlapping peaks are counted as the minimal number of peaks involved in any group. C,D, UpSet plots showing the baseline number of genomic loci with DRIP-Seq peaks in 786-O (C) or H1299 (D) *PBRM1*-WT or -KO cells, according to their genomic localization. Peaks that overlap with more than one feature are indicated by connected dots below the graph. The total number of genomic loci of each feature is indicated by horizontal bars on the bottom right. Stacked pie charts provide an additional representation of the genomic repartition of DRIP-Seq peaks. Merge of both replicates was used for the analysis.

The number of specific genomic loci associated with DRIP-seq peaks was not drastically modified upon talazoparib exposure, in none of the cell lines, independently from PBRM1 status (Figure 41A,B). However, the intensity of the peaks – defined as the number of reads per consensus peaks which were present in at least two independent samples from the same cell line – was substantially increased

following talazoparib treatment, and particularly in *PBRM1*-KO cells, although no consistent pattern could be found across the 786-O and H1299 *PBRM1*-isogenic models (Figure 41E,F). This observation suggests that talazoparib might preferentially prevent the resolution of R-loops rather than promoting their formation at “new” genomic loci. This phenotype is likely to be exacerbated by *PBRM1* deficiency which leads to higher absolute number of potential fragile intronic loci for the generation of R-loops.

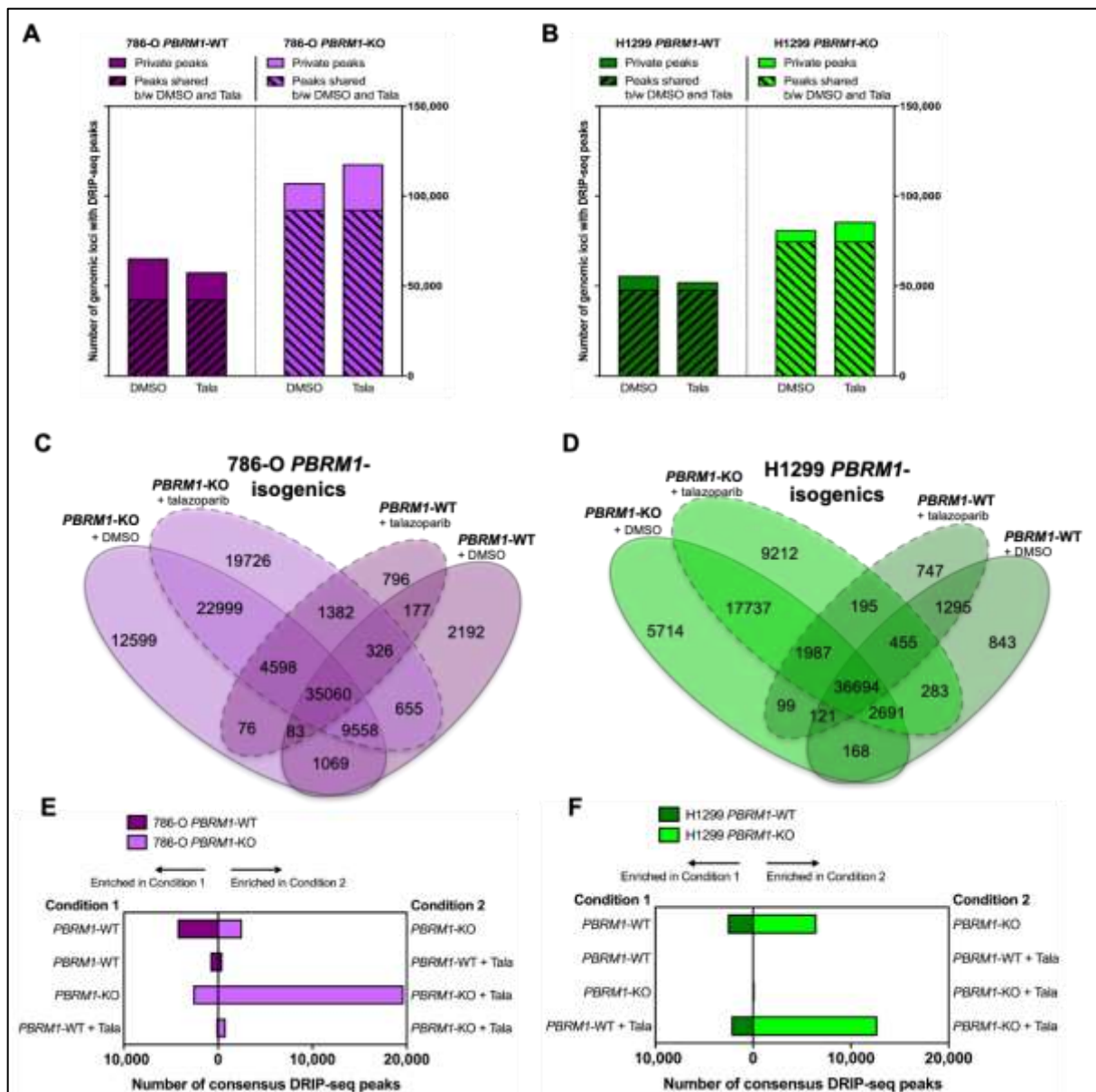


Figure 41. Impact of talazoparib exposure on DNA-RNA hybrids. A,B, Bar plots displaying the number of genomic loci with DRIP-Seq peaks in merged replicates of 786-O (A) or H1299 (B) *PBRM1*-isogenic cells upon DMSO (vehicle) or talazoparib exposure. Connected or overlapping peaks are counted as the minimal number of peaks involved in any group. C,D, Venn diagrams depicting all the 15 possible combinations of common DRIP-Seq peaks in merged replicates of 786-O (C) or H1299 (D) *PBRM1*-isogenic models, according to *PBRM1* status and talazoparib exposure. E,F, Mirror bar chart displaying the number of consensus peaks significantly enriched in a given condition (Condition 1) in the 786-O (E) or H1299 (F) *PBRM1*-isogenic model as compared to another condition (Condition 2), after differential analysis using DESeq2, FDR ≤ 0.05

d. R-loop resolution defects of *PBRM1*-KO cells

To further examine the origin of R-loops accumulation in *PBRM1*-KO cells, we first analyzed the mass spectrometry proteomic profiles of HAP1 *PBRM1*-isogenic cells. This revealed a significant downregulation of multiple proteins involved in R-loops resolution, including the RNA:DNA hybrids-specific endonuclease RNase H1 (Log₂(FC) = -0.460, FDR = 0.0083), the RNA:DNA hybrids helicases SETX (Log₂(FC) = -0.366, FDR = 0.0006), DHX9 (Log₂(FC) = -0.197, FDR = 0.0019) and BLM (Log₂(FC) = -0.476, FDR = 0.0002), the 5'-3' exoribonuclease XRN2 (Log₂(FC) = -0.193, FDR = 0.0024), as well as several other R-loops processing factors (Figure 42A).

We confirmed the decrease in SETX expression in *PBRM1*-KO cells by western blot in 786-O *PBRM1*-isogenic model, and effectively observed that it was reversed by the re-expression of PBRM1 (Figure 42B), suggesting a PBRM1-dependent regulation of SETX expression. To explore whether PBRM1 and SETX expressions were also correlated in human tumour samples, we analyzed mRNA expression data from the TCGA ccRCC (KIRC) and NSCLC (LUAD) cohorts. We found that SETX mRNA expression was positively correlated with PBRM1 mRNA expression in both cohorts (KIRC, Spearman's correlation coefficient $r = 0.7191$, $p < 0.0001$; LUAD, $r = 0.5458$, $p < 0.0001$; Figure 42C). Additionally, we observed a correlation between the mRNA expression of PBRM1 and other R-loop processing factors identified in the HAP1 proteomic dataset, such as DHX9 and XRN2 (Figure 42D,E). Altogether, these findings suggest that loss of PBRM1 associates with down-regulation of a number of factors involved in R-loops processing, which might, at least in part, explain the accumulation of these structures in PBRM1-KO tumour cells.

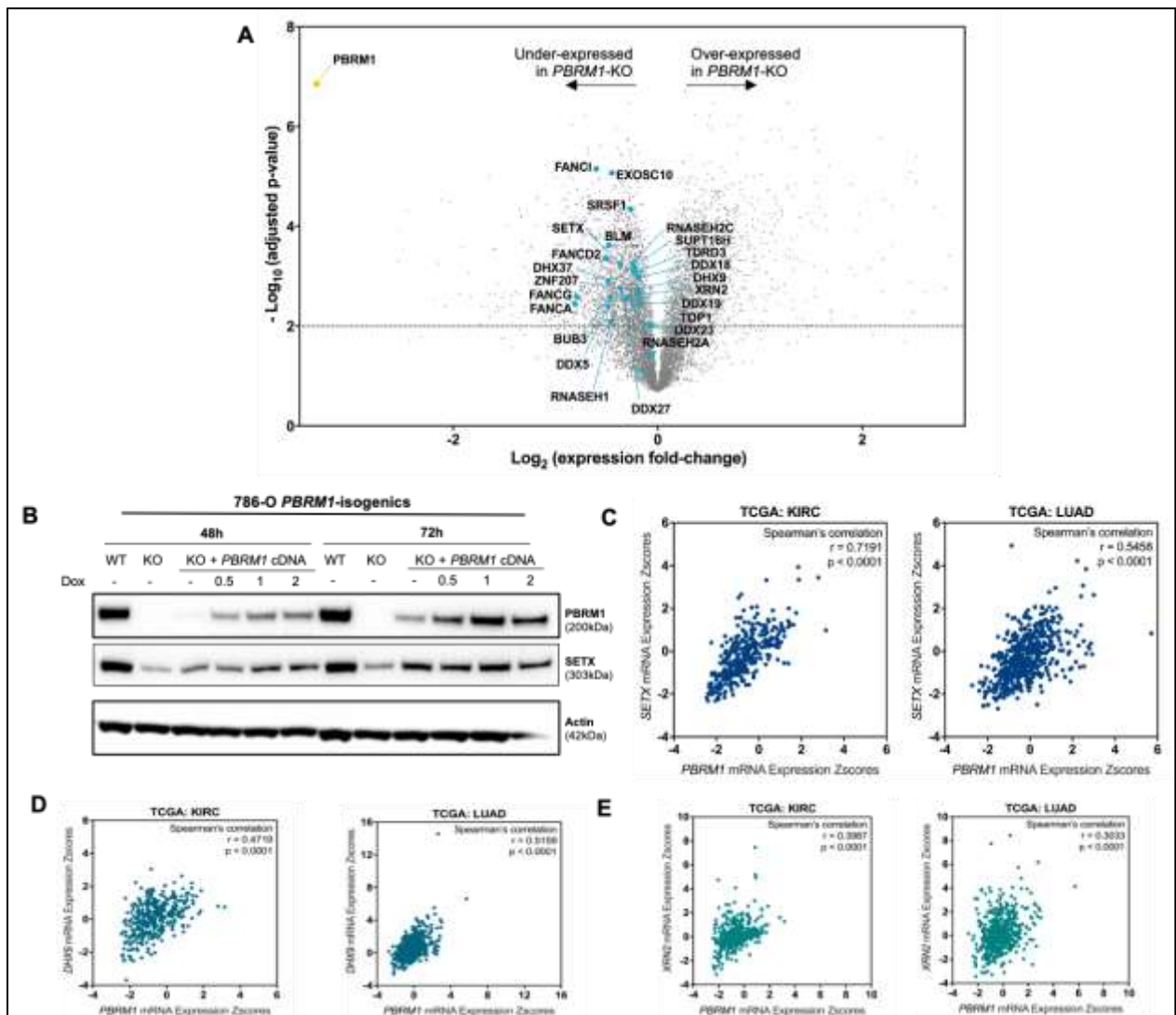


Figure 42. DNA-RNA helicases expressions according to PBRM1 status. A, Volcano plot showing the significantly dysregulated proteins (grey dots) in HAP1 *PBRM1*-KO cells, as compared to HAP1 *PBRM1*-WT cells assessed by mass spectrometry. Proteins that have been reported to be involved in R-loops resolution or metabolism are shown as blue dots; names of the significantly dysregulated ones (FDR q -value < 0.01) are depicted. B, Western blot of PBRM1 and SETX in 786-O *PBRM1*-WT cells, and 786 O *PBRM1*-KO cells upon induced transient re-expression of PBRM1. Cells were harvested at 48 and 72 h following transduction with a doxycycline-inducible construct containing PBRM1 cDNA in the absence or presence of doxycycline at various concentrations (μM). Lysates were probed with the indicated antibodies. There is a residual expression of PBRM1 in the absence of doxycycline because the re-expression system is slightly leaky. C-E, Scatter plots displaying the correlation between PBRM1 and SETX (C) or DHX9 (D) or XRN2 (E) gene expression in the TCGA KIRC (left) and LUAD (right) cohorts. Shown are PBRM1 (X axis) and SETX (Y axis) mRNA expression z-scores retrieved from cBioPortal.org for the corresponding cohorts (last accessed on 01/26/2020). Each dot represents an individual tumour sample.

III. Discussion

In this final Chapter, we identified that the genomic instability characterizing PBRM1-deficient cells was exacerbated under treatment with PARPi, eventually reaching a level not suitable with cell survival and leading to cell death. We notably observed: (i) increased DNA damage response signaling in *PBRM1*-KO cells following PARPi but not following other DNA DSB inducers, (ii) increased micronuclei formation following PARPi, exacerbated in a *PBRM1*-KO context, (iii) accumulation of R-loops in *PBRM1*-KO cells at specific, and mostly intronic, genomic loci, which were again exacerbated upon PARPi exposure, and (iv) reduced R-loop resolution capacities in PBRM1-deficient cells. Importantly, mitosis/kinetochore defects associated with PBRM1 deficiency were not correlated to increased vulnerability to PARPi in our model. Altogether, these findings indicate that PARPi exposure may exceed *PBRM1*-KO cells capacities to handle replication-transcription stress and therefore leading to apoptosis.

Chapter VII: Conclusion, discussion and perspectives

I. Critical findings resulted from this PhD work

In this PhD work, we used a unique combination of four *PBRM1*-isogenic cellular models and four non-isogenic ccRCC cell lines to identify and characterize genomic vulnerabilities associated with PBRM1 loss, in order to uncover therapeutic options that could specifically target PBRM1-mutant advanced ccRCC. We notably found that *PBRM1*-KO cells were vulnerable to PARPi and ATRi, and that combining PARPi and ATRi *in vitro* could enlarge the therapeutic window between *PBRM1*-KO and -WT cells by eliciting additive cytotoxic effects.

Unlike the synthetic lethal interaction previously described between loss-of-function of BRCA proteins and PARPi, we found no evidence of HR defects linked to PBRM1 loss in our models, which rather exhibited increased DNA damage response signaling when PBRM1-deficient. In particular, we observed that *PBRM1*-KO cells appropriately loaded RAD51 onto DNA DSB lesions, both in the absence of exogenous stress and following treatment with DSB-inducers. Additionally, the analysis of large RNA-sequencing data retrieved from the TCGA database showed that tumour samples associated with deleterious mutations in *PBRM1* displayed the same level of heterozygosity as *PBRM1*-WT samples, which is in favor of functional HR DNA repair pathway.

However, we evidenced that PBRM1-deficient cells presented increased baseline genomic instability assessed by the quantification of micronuclei-positive cells. In addition, using the TCGA dataset, we noticed that *PBRM1*-mutated samples consistently harbored higher rates of mutations per kb than *PBRM1*-WT samples across all tumour types, with a statistically meaningful difference in 11 out of 19 tumour types.

When investigating the potential sources of this genomic instability, we found that PBRM1 defect was associated with multiple stress phenotypes (Figure 43): (i) mitosis abnormalities with prolonged pro-metaphases characterized by chromosomes struggling to reach the metaphase plate, (ii) transcriptional irregularities with fragmented nucleoli structures, and (iii) replication stress with reduced replication fork progression which attests of the S-phase checkpoint constant activation.

Using time-lapse microscopy on H2B-mCherry stably-labeled cells, we found no correlation between the prolonged presence (> 45 minutes) of lagging chromosomes during pro-metaphase and subsequent formation of a micronucleus in daughter cells, thereby suggesting that mitosis abnormalities may not be the major source of genomic instability in *PBRM1*-KO cells.

Using DRIP-sequencing in our models with and without PARPi, we identified that *PBRM1*-KO cells presented almost twice more genomic loci associated with R-loops than *PBRM1*-WT cells, reflecting a higher rate of replication-transcription conflicts in case of PBRM1 deficiency, which is a major source of genomic instability and DNA DSB generation. Upon exposure to PARPi, the number and position of peaks within the genome were barely modified; however, the intensity of the peaks was exacerbated in *PBRM1*-KO cells, suggesting that PARPi act at preventing the resolution of R-loops rather than generating new ones.

We finally investigated whether this accumulation of R-loops was linked to a reduced ability to remove them in case of PBRM1-deficiency, and found that PBRM1-deficient cells expressed reduced levels of enzymes implicated in the resolution of R-loops, including SETX, DHX9 and XRN2, which were confirmed in the whole proteomic

analysis of the *PBRM1*-isogenic HAP1 model and TCGA mRNA expression data in multiple tumour types.

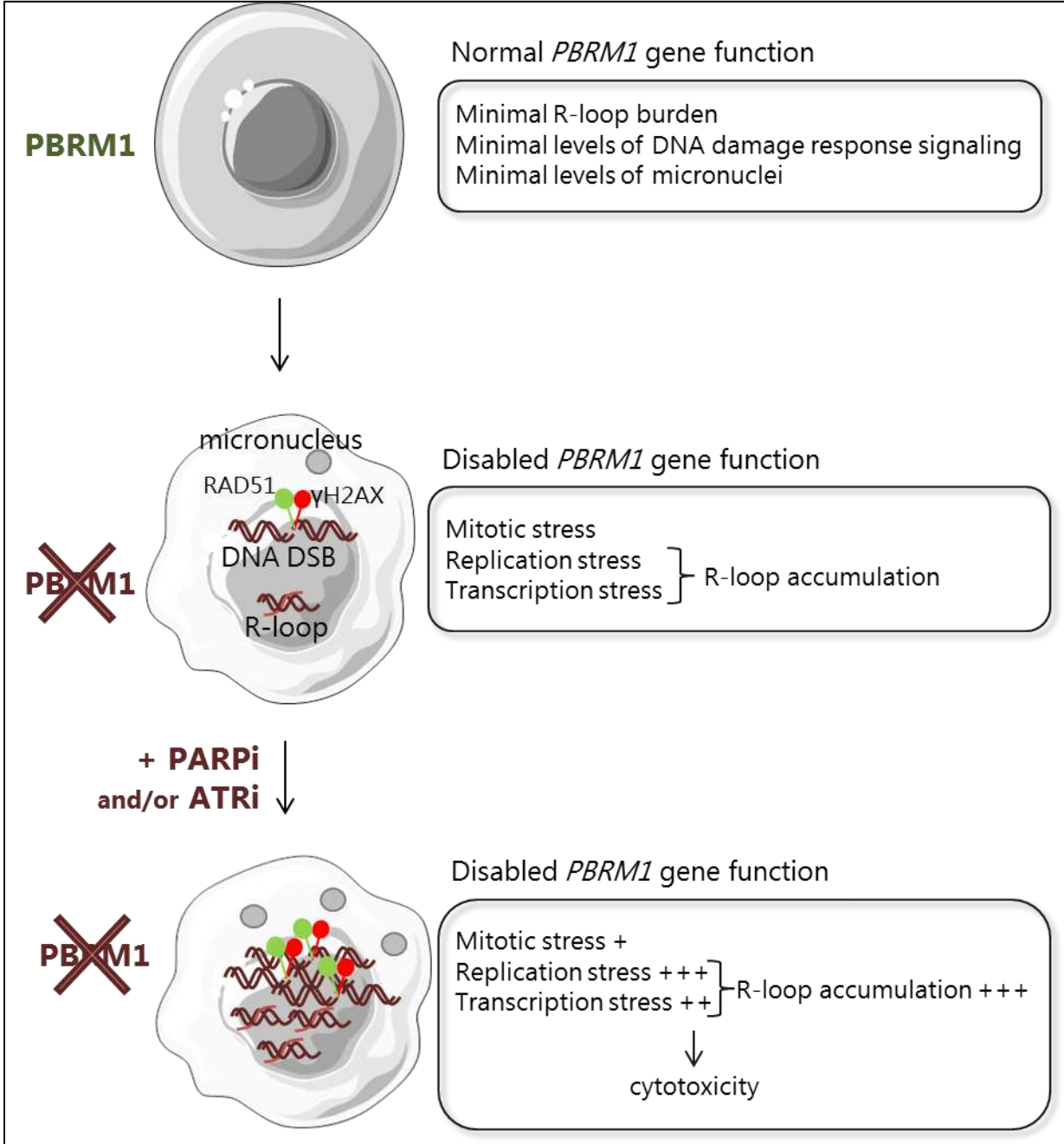


Figure 43. Model of *PBRM1* defect-dependent cytotoxicity following exposure to DNA repair inhibitors.

Altogether, this PhD work highlighted a previously unknown synthetic lethal interaction between PBRM1 loss and PARPi through a new route of PARPi-induced vulnerability – independent from HR deficiency – presumably by definitely disrupting the cell capacity to balance replication-transcription stress.

II. Final discussion and perspectives

Relevance and cost-effectiveness of a tissue-agnostic approach:

In this PhD work, we show that clinical PARPi and ATRi are synthetic lethal with PBRM1 defects. There is currently no approved precision medicine-based approach that specifically targets PBRM1 deficiency. PBRM1 defects are frequent in human cancers (more than 4% of all cases, among the 50 genes the most frequently altered, Table 5) and affects a wide range of tumour localizations, including chordoma (up to 60% of cases)⁷⁴, ccRCC (about 40% of cases), intrahepatic cholangiocarcinoma (up to 35% of cases)^{75,76}, mesothelioma (up to 20% of cases)⁷⁷, cutaneous squamous cell carcinoma (up to 16% of cases) (cbioportal.org) and endometrial carcinoma (up to 12% of cases).

We reproduced the PBRM1-PARP1 synthetic lethal interaction in multiple isogenic and non-isogenic models from various genetic backgrounds; therefore such connection appears to be cell type-independent, suggesting that these might have translational utility to other cancer types than ccRCC. Although we believe that the loss of PBRM1 needs to be a frequent and early event in the course of a tumour to represent a valuable biomarker – which is the case in ccRCC⁹ – but not necessarily in other localizations such as cholangiocarcinoma where it was found to be a late event⁷⁵. In addition, cholangiocarcinoma is generally a platinum-sensitive disease⁴¹, which indicates that PBRM1 loss might not be the major component that drives their response to drugs, although it may still benefit from a PARPi and ATRi treatment. On the other hand, chordoma is a rare bone cancer of the axial skeleton that displays characteristics similar to ccRCC in terms of high frequency of 3p and 9p loss and resistance to standard chemotherapy⁷⁴; therefore chordoma may represent a good candidate for the use of PBRM1 mutational status as a predictive biomarker of PARPi and ATRi response.

Despite being an early event during the oncogenesis process, *PBRM1* mutation frequency rate within each cancer types should be considered before pursuing to a tissue-agnostic evaluation of PARPi in all *PBRM1*-mutated cancers. A tissue-agnostic indication refers to the approval of a drug targeting an oncogenic driver event regardless of the primary organ; a recent example being larotrectinib ¹³⁹, which is approved for adult and pediatric patients with any solid tumour that harbors a NTRK-fusion. Basket clinical trials, which are designed to evaluate drugs upon a specific molecular alteration regardless of the cancer type, use this approach. A recent evaluation of the cost-effectiveness of a hypothetical targeted therapy used upon a systematic tissue-agnostic design showed that the cost-effectiveness of such an approach is highly related to (i) the tissue prevalence of the mutation and (ii) the positive predictive value of the screening test ¹⁴⁰. For example, for a screening test with 99% sensitivity and 95% specificity, the estimated cost per life-year gained would be 76,124\$ for a cancer type with a 20% prevalence of mutation, while it would be 532,000\$ for a cancer type where the mutation is found in 1% of cases.

Feasibility of PBRM1 status assessment in routine.

Of course, the implementation into the clinic of PBRM1 status as a predictive biomarker for a screen-and-treat strategy would require establishing guidelines on diagnostic tests. Loss-of function of PBRM1 is easy and cheap to assess using immunohistochemistry (IHC) on routine paraffin-embedded tumour tissue. We optimized an in-house protocol, using the antibody from Bethyl Laboratories: (ref A301-591A; dilution 1:250) on a series of cholangiocarcinoma samples (work of Clémence Astier, data not shown in this report).

Additionally, Sanger sequencing or targeted next-generation sequencing could be performed with the advantages of bringing the exact information of the location,

nature and allelic frequency of a given *PBRM1* alteration in a sample, keeping in mind that these results may vary. For example, *Ho et al.* noticed that 10% of PBRM1 IHC-negative ccRCC samples were not confirmed by Sanger sequencing in their cohort of 418 patients¹⁴¹. This over-diagnosis by IHC is not necessarily an artifact and could be explained by another SWI/SNF subunit defect (principally ARID2 and BRD7) that leads to PBRM1 under-expression while its gene sequence is unaffected^{120,142-144}.

We – and others^{120,142-144} – indeed observed that loss of ARID2 (and BRD7, data not shown) led to PBRM1 disruption from PBAF (Figure 32). This observation suggests that ARID2-defective tumours might under-express PBRM1 and therefore, might present increased vulnerability to PARPi as well. However, in the cutaneous melanoma TCGA dataset where 21% of samples are *ARID2*-mutated, there is no difference in PBRM1 mRNA expression according to ARID2 mutational status ($p = 0.12$); neither in endometrial carcinoma where 13% of samples are *ARID2*-mutated ($p = 0.09$) (<https://www.cbioportal.org/>). This indicates that the translational value of this *in vitro* observation might be limited and might not be extrapolated to actual *ARID2*-mutant tumour samples.

Alternative mechanisms.

In Figure 43, we propose a working model that is consistent with our experimental data. Exposure to PARPi causes increased replication stress, due to the accumulation of trapped-PARP1 lesions which stall the replication fork, or due to decreased S-phase checkpoint activation and impaired replication stress response. When PBRM1 function is intact, the replication stress induced by PARPi remains limited, potentially thanks to PBRM1-mediated replication fork re-priming post-repair⁸⁷ and ATM-dependent transcriptional silencing nearby DNA DSBs⁸⁵. This limited replication stress causes moderate formation of micronuclei. In PBRM1-deficient tumour cells, the DNA damage response signaling is permanently activated (Figure 26), the cells

display increased mitotic stress (Figure 29), increased transcriptional stress (Figure 33) and increased replication stress (Figure 34), resulting in a higher R-loop burden (Figure 40) which are caused by collisions between progressing replication forks and unstopped transcription bubbles. Exposure to PARPi or ATRi further enhances replication stress which, in a PBRM1-defective context, favors DNA damage accumulation and micronuclei formation, potentially following impaired fork resolution and defective ATM-dependent transcriptional silencing. Upon prolonged exposure to PARPi or ATRi, DNA damage accumulation eventually reaches levels that are no longer compatible with cell survival, thereby causing tumour cell death.

Although we suggest a working model in Figure 43 that fit our findings, additional mechanisms might also contribute to the PBRM1/DNA repair inhibitors synthetic lethality. R-loops induce a DNA damage response that can be mediated by ATM, ATR, or the non-canonical ATM-ATR response^{135,145,146}. Because PBRM1, when phosphorylated by ATM, contributes to transcriptional repression in the vicinity of DNA DSBs⁸⁷, it is possible that in the absence of PBRM1, the resulting defects in ATM-dependent transcriptional silencing favor the accumulation of R-loops and S-phase-dependent DNA damage response defects, which underlie sensitivity to PARPi and ATRi.

It is also possible that the transcriptional stress observed in PBRM1-defective cells is rather a consequence of baseline R-loop accumulation than a cause. Indeed, R-loop-dependent transcriptional stress can cause DNA damage by sequestering BRCA1 at sites of stalled RNA polymerase II¹⁴⁷, where BRCA1 recruits SETX to prevent DNA damage, notably at termination sites^{148,149}. Because SETX is also recruited at sites of DNA DSBs in transcriptionally active loci – where it limits translocations and genomic instability¹⁵⁰, a transcriptional stress-dependent sensitivity to DNA repair inhibitors might represent a second alternative model.

This model is also consistent with the previously described role of PBRM1 in regulating the transcription of stress response genes: PBRM1 has notably been shown to mediate cytoprotective effects against endogenous stresses – including oncogenic, replicative stress^{151,152} and exogenous stresses – including from oxidative, hypoxic, and thermal sources^{91,153,154}. Other publications have also reported an important role for PBRM1 in the regulation of p53 transcriptional activity^{151,155}.

Another potential hypothesis to explain the PBRM1/DNA repair inhibitors synthetic lethality is that PBRM1, which contributes to fork re-priming through PCNA recruitment through its BAH domains⁸⁷, might also interact with other chromatin remodelers that are ATR substrates and prevent replication forks from collapsing, such as the SWI/SNF family member SMARCAL1¹⁵⁶. This underlines the multifaceted functions of PBRM1 in various aspects of genome stability maintenance, including DNA repair, replication fork stress response and transcriptional stress.

Importantly, the nucleolar fragmentation and disorganized nucleoli structures that we observed (Figure 33) has never been previously described before in a PBRM1-defective context. The recent report from *Zhou et al.* identified that the loss of the H3K9me2 histone mark triggered R-loop accumulation which further led to multilobed nucleoli¹²¹, both phenotypes that are also present in *PBRM1*-KO cells. Even though PBRM1 has never been shown to directly interact with H3K9me2 to our knowledge, we might hypothesize that its BAH domains, together with the chromodomains of SMARCC1/SMARCC2, contribute to guide PBAF onto – or near – H3K9me2 (by similarity to the CMT3 protein, which binds H3K9me2 via both its BAH- and chromo-domains, described in plants in¹²²).

Highlighting the complexity of the system.

Altogether, we independently identified multiple mechanisms which could support an increased PARPi sensitivity in *PBRM1*-KO cells, including increased DNA damage response signaling, increased micronuclei formation, increased mutational load, increased DNA:RNA hybrids, decreased replication fork velocity, mitosis abnormalities, nucleoli fragmentation etc. All of these mechanisms can be interconnected with each other and grouped under a generic “genomic” stress signature.

For example, it remains complex to robustly evaluate whether the replication stress primarily generates the increased DNA damage response signaling (for example through replication fork collapse and DNA DSB generation), or whether the overall decreased capacity of DNA damage repair is the primarily source of stalling of replication forks, S-phase checkpoint activation and further decreased progression of replication forks. Alternatively, *PBRM1* dysfunction might alter the directing of the chromatin-remodeling capacity of PBAF over the genome; in such case, transcriptional perturbations may be the main source of replication stress via R-loop accumulation and nucleoli fragmentation as primary events.

Additional investigations will therefore be required to precisely detail whether the initiating event generating the genomic stress signature associated with *PBRM1*-deficiency is preferentially related to replication, transcription, DNA repair, mitosis or another dysfunctional mechanism.

PBRM1-SETD2 connection:

Importantly, *SETD2* and *PBRM1* – both located on the 3p21 chromosome locus and commonly co-deleted in ccRCC – were recently found to directly cooperate during the mitosis process. *SETD2* has been initially described as a histone methyltransferase specific for lysine 36 of Histone 3 (H3K36me3) trimethylation, a histone mark of

actively transcribed genomic regions shown to be required for DNA repair by HR¹⁵⁷⁻¹⁵⁹. To note, PBRM1 was never identified as a potential reader of the H3K36me3 histone mark, even though it recognizes the H3K14ac mark that is also found in actively transcribed regions, but more specifically at active promoters while H3K36me3 is more specific of the core gene bodies¹⁶⁰. SETD2 was more recently identified as a critical enzyme for the trimethylation of microtubules on lysine 40 during mitosis (α TubK40me3)¹⁶¹, a cytoskeleton mark which localizes at spindle microtubules during mitosis and is recognized by PBRM1⁹³.

Similarly to what we observed in PBRM1-deficient cells, loss of SETD2 has been linked to genomic instability, replication stress¹⁶² and mitosis defects, including multipolar spindle formation, chromosomal bridges during cytokinesis, micronuclei formation, polyploidy and polynucleation¹⁶¹. Interestingly, we observed that loss of PBRM1 in a cellular model which already lacks SETD2 (A498 ccRCC cell line) was not associated with an increased sensitivity to PARPi (*data not shown*), suggesting that both PBRM1 and SETD2 integral functions might be required to sustain PARPi response, and loss of either PBRM1 or SETD2 might be sufficient to confer a vulnerability to PARPi in ccRCC. Although SETD2-deficiency was previously linked to synthetic lethal interaction with WEE1 inhibitors¹⁶³ – WEE1 is the gatekeeper of the G2/M checkpoint required for completing DNA repair before mitotic entry – the hypothesis of a SETD2-PARP1 synthetic lethality needs further investigations. From a clinical point of view, this would improve the therapeutic options for a higher number of ccRCC patients.

Attractive option of combining PARPi/ATRi and immune-checkpoint inhibitors.

A therapeutic option which will be important to consider in a PBRM1-defective context is the combinatorial use of PARPi/ATRi with immune-checkpoint blockers – the latter being already approved for the treatment of advanced ccRCC^{10,27}. Published data currently remain conflicting about the potential role of PBRM1

deficiency in influencing the immunogenicity of the tumour microenvironment^{37,38,164,165}. In *Chabanon & Morel et al.*, we show that PBRM1 deficiency leads to increased activation of the cGAS-STING signaling pathway following exposure to PARPi or ATRi (work of Roman Chabanon, data not shown in the present report). The cGAS-STING cascade is stimulated by the presence of cytosolic DNA and induces an immune response via the production of interferon¹⁶⁶. We and others previously described that PARPi have cell-autonomous immunomodulatory properties and could notably activate the cGAS/STING pathway in specific DNA damage response-defective genetic contexts^{97,167-169}. Therefore, treatment with PARPi or ATRi could increase the immunogenicity more specifically in PBRM1-deficient tumours, hence sensitizing them to immune-checkpoint blockers. Additionally, we show in Figure 27 that PBRM1-defective tumours express an increased mutational burden compared to PBRM1-proficient tumours, which is a validated predictive biomarker for immune-checkpoint inhibitor response¹⁷⁰. This provides a strong preclinical basis for further clinical evaluation of combinatorial – either concomitant or sequential (i.e. PARPi and/or ATRi “priming”, then immune blockade) – use of these DNA repair inhibitors with immune-checkpoint blockers. Of note, the combination of PARPi and immune-checkpoint blockade already showed an acceptable safety profile¹⁷¹. We are currently evaluating such hypothesis in the ARIANES investigator-initiated basket study, which we developed at Gustave Roussy and in four additional French centers, and which has a dedicated ccRCC cohort.

Final conclusion:

Altogether, these data suggest that PBRM1-deficient tumour cells are characterized by a vulnerability to PARPi and ATRi that might vary across tumour types and is predominantly applicable to ccRCC. PBRM1 loss leads to multimodal increased genomic instability that associates mitotic stress, replication stress and transcription stress. Further investigation will be needed to fully elucidate the causal connections between each mechanism. In conclusion, our findings shed light on the genetic vulnerabilities associated with loss of PBRM1, related to its role in maintaining genome integrity.

References

1. Bray, F. *et al.* Global cancer statistics 2018: GLOBOCAN estimates of incidence and mortality worldwide for 36 cancers in 185 countries. *CA. Cancer J. Clin.* **68**, 394–424 (2018).
2. Chow, W.-H., Dong, L. M. & Devesa, S. S. Epidemiology and risk factors for kidney cancer. *Nat. Rev. Urol.* **7**, 245–257 (2010).
3. Macleod, L. C. *et al.* Risk factors for renal cell carcinoma in the VITAL study. *J. Urol.* **190**, 1657–1661 (2013).
4. Behrens, G. & Leitzmann, M. F. The association between physical activity and renal cancer: systematic review and meta-analysis. *Br. J. Cancer* **108**, 798–811 (2013).
5. Tahbaz, R., Schmid, M. & Merseburger, A. S. Prevention of kidney cancer incidence and recurrence: lifestyle, medication and nutrition. *Curr. Opin. Urol.* **28**, 62–79 (2018).
6. Capitanio, U. *et al.* Epidemiology of Renal Cell Carcinoma. *Eur. Urol.* **75**, 74–84 (2019).
7. Choyke, P. L., Glenn, G. M., Walther, M. M., Zbar, B. & Linehan, W. M. Hereditary renal cancers. *Radiology* **226**, 33–46 (2003).
8. Devita, Hellman and Rosenberg's Cancer: Principles & Practice of Oncology, 11th edition. <https://www.livres-medicaux.com/devita-hellman-and-rosenberg-s-cancer-11th-edition.html>.
9. Turajlic, S. *et al.* Deterministic Evolutionary Trajectories Influence Primary Tumor Growth: TRACERx Renal. *Cell* **173**, 595–610.e11 (2018).
10. EAU Guidelines. Edn. presented at the EAU Annual Congress Amsterdam. (2020).
11. Siegel, R. L., Miller, K. D. & Jemal, A. Cancer statistics, 2020. *CA. Cancer J. Clin.* **70**, 7–30 (2020).
12. Udager, A. M. & Mehra, R. Morphologic, Molecular, and Taxonomic Evolution of Renal Cell Carcinoma: A Conceptual Perspective With Emphasis on Updates to the 2016 World Health Organization Classification. *Arch. Pathol. Lab. Med.* **140**, 1026–1037 (2016).
13. Warren, A. Y. & Harrison, D. WHO/ISUP classification, grading and pathological staging of renal cell carcinoma: standards and controversies. *World J. Urol.* **36**, 1913–1926 (2018).
14. Gebhard, R. L. *et al.* Abnormal cholesterol metabolism in renal clear cell carcinoma. *J. Lipid Res.* **28**, 1177–1184 (1987).

15. Zbar, B., Brauch, H., Talmadge, C. & Linehan, M. Loss of alleles of loci on the short arm of chromosome 3 in renal cell carcinoma. *Cancer* **4** (1987).
16. Linehan, W. M. & Ricketts, C. J. The Cancer Genome Atlas of renal cell carcinoma: findings and clinical implications. *Nat. Rev. Urol.* **16**, 539–552 (2019).
17. Cancer Genomics of the Kidney. FP7-HEALTH-2009 – 241669 - CAGEKID - D9.6 Final report (M54).
18. Gerlinger, M. *et al.* Genomic architecture and evolution of clear cell renal cell carcinomas defined by multiregion sequencing. *Nat. Genet.* **46**, 225–233 (2014).
19. Huang, Y. *et al.* Clonal architectures predict clinical outcome in clear cell renal cell carcinoma. *Nat. Commun.* **10**, 1245 (2019).
20. Joseph, R. W. *et al.* Clear Cell Renal Cell Carcinoma Subtypes Identified by BAP1 and PBRM1 Expression. *J. Urol.* **195**, 180–187 (2016).
21. Peña-Llopis, S. *et al.* BAP1 loss defines a new class of renal cell carcinoma. *Nat. Genet.* **44**, 751–759 (2012).
22. Peña-Llopis, S., Christie, A., Xie, X.-J. & Brugarolas, J. Cooperation and Antagonism among Cancer Genes: The Renal Cancer Paradigm. *Cancer Res.* **73**, 4173–4179 (2013).
23. Turajlic, S. *et al.* Tracking Cancer Evolution Reveals Constrained Routes to Metastases: TRACERx Renal. *Cell* **173**, 581–594.e12 (2018).
24. Eckel-Passow, J. E. *et al.* BAP1 and PBRM1 in metastatic clear cell renal cell carcinoma: tumor heterogeneity and concordance with paired primary tumor. *BMC Urol.* **17**, 19 (2017).
25. Pawłowski, R. *et al.* Loss of PBRM1 expression is associated with renal cell carcinoma progression. *Int. J. Cancer* **132**, E11–E17 (2013).
26. de Velasco, G. *et al.* Targeted genomic landscape of metastases compared to primary tumours in clear cell metastatic renal cell carcinoma. *Br. J. Cancer* **118**, 1238–1242 (2018).
27. Escudier, B. *et al.* Renal cell carcinoma: ESMO Clinical Practice Guidelines for diagnosis, treatment and follow-up†. *Ann. Oncol.* **30**, 706–720 (2019).
28. Motzer, R. J. *et al.* NCCN Guidelines Insights: Kidney Cancer, Version 2.2020. *J. Natl. Compr. Canc. Netw.* **17**, 1278–1285 (2019).
29. Fuhrman, S. A., Lasky, L. C. & Limas, C. Prognostic significance of morphologic parameters in renal cell carcinoma. *Am. J. Surg. Pathol.* **6**, 655–663 (1982).
30. Heng, D. Y. C. *et al.* Prognostic Factors for Overall Survival in Patients With Metastatic Renal Cell Carcinoma Treated With Vascular Endothelial Growth Factor–Targeted Agents: Results From a Large, Multicenter Study. *J. Clin. Oncol.* **27**, 5794–5799 (2009).

31. Motzer, R. J., Bacik, J., Murphy, B. A., Russo, P. & Mazumdar, M. Interferon-alfa as a comparative treatment for clinical trials of new therapies against advanced renal cell carcinoma. *J. Clin. Oncol. Off. J. Am. Soc. Clin. Oncol.* **20**, 289–296 (2002).
32. Lokich, J. Spontaneous regression of metastatic renal cancer. Case report and literature review. *Am. J. Clin. Oncol.* **20**, 416–418 (1997).
33. Latif, F. *et al.* Identification of the von Hippel-Lindau disease tumor suppressor gene. *Science* **260**, 1317–1320 (1993).
34. Baldewijns, M. M. *et al.* VHL and HIF signalling in renal cell carcinogenesis. *J. Pathol.* **221**, 125–138 (2010).
35. Motzer, R. J. *et al.* Nivolumab plus Ipilimumab versus Sunitinib in Advanced Renal-Cell Carcinoma. *N. Engl. J. Med.* **378**, 1277–1290 (2018).
36. Rini, B. I. *et al.* Pembrolizumab plus Axitinib versus Sunitinib for Advanced Renal-Cell Carcinoma. *N. Engl. J. Med.* **380**, 1116–1127 (2019).
37. McDermott, D. F. *et al.* Clinical activity and molecular correlates of response to atezolizumab alone or in combination with bevacizumab versus sunitinib in renal cell carcinoma. *Nat. Med.* **24**, 749–757 (2018).
38. Liu, X.-D. *et al.* PBRM1 loss defines a nonimmunogenic tumor phenotype associated with checkpoint inhibitor resistance in renal carcinoma. *Nat. Commun.* **11**, 2135 (2020).
39. Braun, D. A. *et al.* Clinical Validation of PBRM1 Alterations as a Marker of Immune Checkpoint Inhibitor Response in Renal Cell Carcinoma. *JAMA Oncol.* (2019) doi:10.1001/jamaoncol.2019.3158.
40. Miao, D. *et al.* Genomic correlates of response to immune checkpoint therapies in clear cell renal cell carcinoma. *Science* **359**, 801–806 (2018).
41. Abou-Alfa, G. K. *et al.* Pemigatinib for previously treated, locally advanced or metastatic cholangiocarcinoma: a multicentre, open-label, phase 2 study. *Lancet Oncol.* **21**, 671–684 (2020).
42. Wu Ct, null & Morris, J. R. Genes, genetics, and epigenetics: a correspondence. *Science* **293**, 1103–1105 (2001).
43. Waddington, C. H. Canalization of Development and the Inheritance of Acquired Characters. *Nature* **150**, 563–565 (1942).
44. Molloy, P. L. Effects of DNA methylation on specific transcription by RNA polymerase II in vitro. *Mol. Biol. Rep.* **11**, 13–17 (1986).
45. Feenstra, A., Fewell, J., Lueders, K. & Kuff, E. In vitro methylation inhibits the promotor activity of a cloned intracisternal A-particle LTR. *Nucleic Acids Res.* **14**, 4343–4352 (1986).

46. Morel, D., Almouzni, G., Soria, J.-C. & Postel-Vinay, S. Targeting chromatin defects in selected solid tumors based on oncogene addiction, synthetic lethality and epigenetic antagonism. *Ann. Oncol.* **28**, 254–269 (2017).
47. Jones, P. A. & Baylin, S. B. The fundamental role of epigenetic events in cancer. *Nat. Rev. Genet.* **3**, 415–428 (2002).
48. Ohm, J. E. *et al.* A stem cell-like chromatin pattern may predispose tumor suppressor genes to DNA hypermethylation and heritable silencing. *Nat. Genet.* **39**, 237–242 (2007).
49. Jones, S. *et al.* Frequent mutations of chromatin remodeling gene ARID1A in ovarian clear cell carcinoma. *Science* **330**, 228–231 (2010).
50. Lawrence, M. S. *et al.* Discovery and saturation analysis of cancer genes across 21 tumor types. *Nature* **505**, 495–501 (2014).
51. Jackson, E. M. *et al.* Genomic analysis using high-density single nucleotide polymorphism-based oligonucleotide arrays and multiplex ligation-dependent probe amplification provides a comprehensive analysis of INI1/SMARCB1 in malignant rhabdoid tumors. *Clin. Cancer Res. Off. J. Am. Assoc. Cancer Res.* **15**, 1923–1930 (2009).
52. Sullivan, L. M., Folpe, A. L., Pawel, B. R., Judkins, A. R. & Biegel, J. A. Epithelioid sarcoma is associated with a high percentage of SMARCB1 deletions. *Mod. Pathol. Off. J. U. S. Can. Acad. Pathol. Inc* **26**, 385–392 (2013).
53. Jelinic, P. *et al.* Recurrent SMARCA4 mutations in small cell carcinoma of the ovary. *Nat. Genet.* **46**, 424–426 (2014).
54. Laurent, B. C. & Carlson, M. Yeast SNF2/SWI2, SNF5, and SNF6 proteins function coordinately with the gene-specific transcriptional activators GAL4 and Bicoid. *Genes Dev.* **6**, 1707–1715 (1992).
55. Chabanon, R. M., Morel, D. & Postel-Vinay, S. Exploiting epigenetic vulnerabilities in solid tumors: Novel therapeutic opportunities in the treatment of SWI/SNF-defective cancers. *Semin. Cancer Biol.* **61**, 180–198 (2020).
56. Kadoch, C. *et al.* Proteomic and bioinformatic analysis of mammalian SWI/SNF complexes identifies extensive roles in human malignancy. *Nat. Genet.* **45**, 592–601 (2013).
57. Shain, A. H. & Pollack, J. R. The Spectrum of SWI/SNF Mutations, Ubiquitous in Human Cancers. *PLOS ONE* **8**, e55119 (2013).
58. Dobzhansky, Th. Genetics of Natural Populations. Xiii. Recombination and Variability in Populations of *Drosophila Pseudoobscura*. *Genetics* **31**, 269–290 (1946).

59. Hartwell, L. H., Szankasi, P., Roberts, C. J., Murray, A. W. & Friend, S. H. Integrating Genetic Approaches into the Discovery of Anticancer Drugs. *Science* **278**, 1064–1068 (1997).
60. Kaelin, W. G. The concept of synthetic lethality in the context of anticancer therapy. *Nat. Rev. Cancer* **5**, 689–698 (2005).
61. Tamkun, J. W. *et al.* brahma: a regulator of Drosophila homeotic genes structurally related to the yeast transcriptional activator SNF2/SWI2. *Cell* **68**, 561–572 (1992).
62. Italiano, A. *et al.* Tazemetostat, an EZH2 inhibitor, in relapsed or refractory B-cell non-Hodgkin lymphoma and advanced solid tumours: a first-in-human, open-label, phase 1 study. *Lancet Oncol.* **19**, 649–659 (2018).
63. Stacchiotti, S. *et al.* Safety and efficacy of tazemetostat, a first-in-class EZH2 inhibitor, in patients (pts) with epithelioid sarcoma (ES) (NCT02601950). *J. Clin. Oncol.* **37**, 11003–11003 (2019).
64. Commissioner, O. of the. FDA approves first treatment option specifically for patients with epithelioid sarcoma, a rare soft tissue cancer. *FDA* <https://www.fda.gov/news-events/press-announcements/fda-approves-first-treatment-option-specifically-patients-epithelioid-sarcoma-rare-soft-tissue> (2020).
65. Kim, K. H. *et al.* SWI/SNF mutant cancers depend upon catalytic and non-catalytic activity of EZH2. *Nat. Med.* **21**, 1491–1496 (2015).
66. Sidker, R. PBRM1 re-introduction in PBRM1-mutant kidney cancer cell lines drives an Interferon-gamma expression signature. *AACR abstract #405* (2018).
67. Charlop-Powers, Z., Zeng, L., Zhang, Q. & Zhou, M.-M. Structural insights into selective histone H3 recognition by the human Polybromo bromodomain 2. *Cell Res.* **20**, 529–538 (2010).
68. Porter, E. G. & Dykhuizen, E. C. Individual Bromodomains of Polybromo-1 Contribute to Chromatin Association and Tumor Suppression in Clear Cell Renal Carcinoma. *J. Biol. Chem.* **292**, 2601–2610 (2017).
69. Wang, Y. *et al.* Histone H3 Lysine 14 Acetylation Is Required for Activation of a DNA Damage Checkpoint in Fission Yeast. *J. Biol. Chem.* **287**, 4386–4393 (2012).
70. Liao, L. *et al.* High affinity binding of H3K14ac through collaboration of bromodomains 2, 4 and 5 is critical for the molecular and tumor suppressor functions of PBRM1. *Mol. Oncol.* **13**, 811–828 (2019).
71. Slaughter, M. J. *et al.* PBRM1 bromodomains variably influence nucleosome interactions and cellular function. *J. Biol. Chem.* **293**, 13592–13603 (2018).

72. Duan, M.-R. & Smerdon, M. J. Histone H3 Lysine 14 (H3K14) Acetylation Facilitates DNA Repair in a Positioned Nucleosome by Stabilizing the Binding of the Chromatin Remodeler RSC (Remodels Structure of Chromatin). *J. Biol. Chem.* **289**, 8353–8363 (2014).
73. Lee, H.-S., Park, J.-H., Kim, S.-J., Kwon, S.-J. & Kwon, J. A cooperative activation loop among SWI/SNF, γ -H2AX and H3 acetylation for DNA double-strand break repair. *EMBO J.* **29**, 1434–1445 (2010).
74. Wang, L. *et al.* Genomic aberrations frequently alter chromatin regulatory genes in chordoma. *Genes. Chromosomes Cancer* **55**, 591–600 (2016).
75. Luchini, C. *et al.* PBRM1 loss is a late event during the development of cholangiocarcinoma. *Histopathology* **71**, 375–382 (2017).
76. Ma, B. *et al.* Distinct clinical and prognostic implication of IDH1/2 mutation and other most frequent mutations in large duct and small duct subtypes of intrahepatic cholangiocarcinoma. *BMC Cancer* **20**, 318 (2020).
77. Bratslavsky, G. *et al.* PBRM1 mutation and immunotherapy efficacy: A comprehensive genomic profiling (CGP) assessment. *J. Clin. Oncol.* **36**, 12091–12091 (2018).
78. Kadoch, C. & Crabtree, G. R. Mammalian SWI/SNF chromatin remodeling complexes and cancer: Mechanistic insights gained from human genomics. *Sci. Adv.* **1**, e1500447 (2015).
79. Brázda, V., Laister, R. C., Jagelská, E. B. & Arrowsmith, C. Cruciform structures are a common DNA feature important for regulating biological processes. *BMC Mol. Biol.* **12**, 33 (2011).
80. Downs, J. A. *et al.* Binding of chromatin-modifying activities to phosphorylated histone H2A at DNA damage sites. *Mol. Cell* **16**, 979–990 (2004).
81. Chai, B., Huang, J., Cairns, B. R. & Laurent, B. C. Distinct roles for the RSC and Swi/Snf ATP-dependent chromatin remodelers in DNA double-strand break repair. *Genes Dev.* **19**, 1656–1661 (2005).
82. Shim, E. Y., Ma, J.-L., Oum, J.-H., Yanez, Y. & Lee, S. E. The yeast chromatin remodeler RSC complex facilitates end joining repair of DNA double-strand breaks. *Mol. Cell. Biol.* **25**, 3934–3944 (2005).
83. Yu, Y., Teng, Y., Liu, H., Reed, S. H. & Waters, R. UV irradiation stimulates histone acetylation and chromatin remodeling at a repressed yeast locus. *Proc. Natl. Acad. Sci.* **102**, 8650–8655 (2005).
84. Brownlee, P. M., Chambers, A. L., Cloney, R., Bianchi, A. & Downs, J. A. BAF180 Promotes Cohesion and Prevents Genome Instability and Aneuploidy. *Cell Rep.* **6**, 973–981 (2014).

85. Kakarougkas, A. *et al.* Requirement for PBAF in Transcriptional Repression and Repair at DNA Breaks in Actively Transcribed Regions of Chromatin. *Mol. Cell* **55**, 723–732 (2014).
86. Meisenberg, C. *et al.* Repression of Transcription at DNA Breaks Requires Cohesin throughout Interphase and Prevents Genome Instability. *Mol. Cell* **73**, 212–223.e7 (2019).
87. Niimi, A., Chambers, A. L., Downs, J. A. & Lehmann, A. R. A role for chromatin remodellers in replication of damaged DNA. *Nucleic Acids Res.* **40**, 7393–7403 (2012).
88. Koch, C. M. *et al.* The landscape of histone modifications across 1% of the human genome in five human cell lines. *Genome Res.* **17**, 691–707 (2007).
89. Taverna, S. D. *et al.* Long-distance combinatorial linkage between methylation and acetylation on histone H3 N termini. *Proc. Natl. Acad. Sci.* **104**, 2086–2091 (2007).
90. Chowdhury, B. *et al.* PBRM1 Regulates the Expression of Genes Involved in Metabolism and Cell Adhesion in Renal Clear Cell Carcinoma. *PLoS One* **11**, e0153718 (2016).
91. Porter, E. G. *et al.* PBRM1 Regulates Stress Response in Epithelial Cells. *iScience* **15**, 196–210 (2019).
92. Xue, Y. *et al.* The human SWI/SNF-B chromatin-remodeling complex is related to yeast Rsc and localizes at kinetochores of mitotic chromosomes. *Proc. Natl. Acad. Sci.* **97**, 13015–13020 (2000).
93. Karki, M. *et al.* A Cytoskeletal Function for PBRM1 Reading Methylated Microtubules. *bioRxiv* (2020) doi:10.1101/2020.04.21.053942.
94. Morel, D., Jeffery, D., Aspeslagh, S., Almouzni, G. & Postel-Vinay, S. Combining epigenetic drugs with other therapies for solid tumours — past lessons and future promise. *Nat. Rev. Clin. Oncol.* **17**, 91–107 (2020).
95. Shorstova, T. *et al.* SWI/SNF-Compromised Cancers Are Susceptible to Bromodomain Inhibitors. *Cancer Res.* **79**, 2761–2774 (2019).
96. Benusiglio, P. R. *et al.* A germline mutation in PBRM1 predisposes to renal cell carcinoma. *J. Med. Genet.* **52**, 426–430 (2015).
97. Chabanon, R. M. *et al.* PARP inhibition enhances tumor cell-intrinsic immunity in ERCC1-deficient non-small cell lung cancer. *J. Clin. Invest.* **129**, 1211–1228 (2019).
98. Wang, X. *et al.* SMARCB1-mediated SWI/SNF complex function is essential for enhancer regulation. *Nat. Genet.* **49**, 289–295 (2017).

99. Kapałczyńska, M. *et al.* 2D and 3D cell cultures – a comparison of different types of cancer cell cultures. *Arch. Med. Sci. AMS* **14**, 910–919 (2018).
100. Lloyd, R. L. *et al.* Combined PARP and ATR inhibition potentiates genome instability and cell death in ATM-deficient cancer cells. *Oncogene* **39**, 4869–4883 (2020).
101. Lord, C. J. & Ashworth, A. PARP inhibitors: Synthetic lethality in the clinic. *Science* **355**, 1152–1158 (2017).
102. Satoh, M. S. & Lindahl, T. Role of poly(ADP-ribose) formation in DNA repair. *Nature* **356**, 356–358 (1992).
103. Kim, M. Y., Zhang, T. & Kraus, W. L. Poly(ADP-ribosyl)ation by PARP-1: ‘PAR-laying’ NAD⁺ into a nuclear signal. *Genes Dev.* **19**, 1951–1967 (2005).
104. McGlynn, P. & Lloyd, R. G. Recombinational repair and restart of damaged replication forks. *Nat. Rev. Mol. Cell Biol.* **3**, 859–870 (2002).
105. Lord, C. J. & Ashworth, A. BRCAness revisited. *Nat. Rev. Cancer* **16**, 110–120 (2016).
106. González-Martín, A. *et al.* Niraparib in Patients with Newly Diagnosed Advanced Ovarian Cancer. *N. Engl. J. Med.* **381**, 2391–2402 (2019).
107. Paull, T. T. *et al.* A critical role for histone H2AX in recruitment of repair factors to nuclear foci after DNA damage. *Curr. Biol. CB* **10**, 886–895 (2000).
108. Cruz, C. *et al.* RAD51 foci as a functional biomarker of homologous recombination repair and PARP inhibitor resistance in germline BRCA-mutated breast cancer. *Ann. Oncol.* **29**, 1203–1210 (2018).
109. Shen, J. *et al.* ARID1A deficiency promotes mutability and potentiates therapeutic antitumor immunity unleashed by immune checkpoint blockade. *Nat. Med.* **24**, 556–562 (2018).
110. Countryman, P. I. & Heddle, J. A. The production of micronuclei from chromosome aberrations in irradiated cultures of human lymphocytes. *Mutat. Res. Mol. Mech. Mutagen.* **41**, 321–331 (1976).
111. Test No. 487: In Vitro Mammalian Cell Micronucleus Test. (2016).
112. Fenech, M. *et al.* Molecular mechanisms of micronucleus, nucleoplasmic bridge and nuclear bud formation in mammalian and human cells. *Mutagenesis* **26**, 125–132 (2011).
113. Liu, D. *et al.* Human NUF2 interacts with centromere-associated protein E and is essential for a stable spindle microtubule-kinetochore attachment. *J. Biol. Chem.* **282**, 21415–21424 (2007).
114. *The Kinetochore:: From Molecular Discoveries to Cancer Therapy.* (Springer-Verlag, 2009). doi:10.1007/978-0-387-69076-6.

115. Maiato, H., DeLuca, J., Salmon, E. D. & Earnshaw, W. C. The dynamic kinetochore-microtubule interface. *J. Cell Sci.* **117**, 5461–5477 (2004).
116. Shen, J. *et al.* ARID1A Deficiency Impairs the DNA Damage Checkpoint and Sensitizes Cells to PARP Inhibitors. *Cancer Discov.* **5**, 752–767 (2015).
117. Park, Y. *et al.* Loss of ARID1A in Tumor Cells Renders Selective Vulnerability to Combined Ionizing Radiation and PARP Inhibitor Therapy. *Clin. Cancer Res.* **25**, 5584–5594 (2019).
118. Smith-Roe, S. L. *et al.* SWI/SNF complexes are required for full activation of the DNA-damage response. *Oncotarget* **6**, 732–745 (2015).
119. Schick, S. *et al.* Systematic characterization of BAF mutations provides insights into intracomplex synthetic lethalties in human cancers. *Nat. Genet.* **51**, 1399–1410 (2019).
120. Pan, D. *et al.* A major chromatin regulator determines resistance of tumor cells to T cell-mediated killing. *Science* **359**, 770–775 (2018).
121. Zhou, H. *et al.* H3K9 Demethylation-Induced R-Loop Accumulation Is Linked to Disorganized Nucleoli. *Front. Genet.* **11**, 43 (2020).
122. Du, J. *et al.* Dual Binding of Chromomethylase Domains to H3K9me₂-containing Nucleosomes Directs DNA Methylation in Plants. *Cell* **151**, 167–180 (2012).
123. Jurkowska, R. Z. *et al.* H3K14ac is linked to methylation of H3K9 by the triple Tudor domain of SETDB1. *Nat. Commun.* **8**, 2057 (2017).
124. Iyer, D. R. & Rhind, N. Replication fork slowing and stalling are distinct, checkpoint-independent consequences of replicating damaged DNA. *PLOS Genet.* **13**, e1006958 (2017).
125. Branzei, D. & Foiani, M. Maintaining genome stability at the replication fork. *Nat. Rev. Mol. Cell Biol.* **11**, 208–219 (2010).
126. Kurashima, K. *et al.* SMARCA4 deficiency-associated heterochromatin induces intrinsic DNA replication stress and susceptibility to ATR inhibition in lung adenocarcinoma. *NAR Cancer* **2**, (2020).
127. Cairns, B. R. *et al.* RSC, an Essential, Abundant Chromatin-Remodeling Complex. *Cell* **87**, 1249–1260 (1996).
128. Labib, K. & Hodgson, B. Replication fork barriers: pausing for a break or stalling for time? *EMBO Rep.* **8**, 346–353 (2007).
129. Bryant, H. E. *et al.* Specific killing of BRCA2-deficient tumours with inhibitors of poly(ADP-ribose) polymerase. *Nature* **434**, 913–917 (2005).
130. Ronson, G. E. *et al.* PARP1 and PARP2 stabilise replication forks at base excision repair intermediates through Fbh1-dependent Rad51 regulation. *Nat. Commun.* **9**, 746 (2018).

131. Colicchia, V. *et al.* PARP inhibitors enhance replication stress and cause mitotic catastrophe in MYCN-dependent neuroblastoma. *Oncogene* **36**, 4682–4691 (2017).
132. Pillay, N. *et al.* DNA Replication Vulnerabilities Render Ovarian Cancer Cells Sensitive to Poly(ADP-Ribose) Glycohydrolase Inhibitors. *Cancer Cell* **35**, 519–533.e8 (2019).
133. Keszthelyi, A., Minchell, N. E. & Baxter, J. The Causes and Consequences of Topological Stress during DNA Replication. *Genes* **7**, (2016).
134. Helmrich, A., Ballarino, M. & Tora, L. Collisions between replication and transcription complexes cause common fragile site instability at the longest human genes. *Mol. Cell* **44**, 966–977 (2011).
135. Crossley, M. P., Bocek, M. & Cimprich, K. A. R-Loops as Cellular Regulators and Genomic Threats. *Mol. Cell* **73**, 398–411 (2019).
136. Aguilera, A. & García-Muse, T. R Loops: From Transcription Byproducts to Threats to Genome Stability. *Mol. Cell* **46**, 115–124 (2012).
137. Allison, D. F. & Wang, G. G. R-loops: formation, function, and relevance to cell stress. *Cell Stress* **3**, 38–46 (2019).
138. Velichko, A. K. *et al.* Hypoosmotic stress induces R loop formation in nucleoli and ATR/ATM-dependent silencing of nucleolar transcription. *Nucleic Acids Res.* **47**, 6811–6825 (2019).
139. Looney, A.-M., Nawaz, K. & Webster, R. M. Tumour-agnostic therapies. *Nat. Rev. Drug Discov.* **19**, 383–384 (2020).
140. Ramsey, S. D., Shankaran, V. & Sullivan, S. D. Basket Cases: How Real-World Testing for Drugs Approved Based on Basket Trials Might Lead to False Diagnoses, Patient Risks, and Squandered Resources. *J. Clin. Oncol. Off. J. Am. Soc. Clin. Oncol.* **37**, 3472–3474 (2019).
141. Ho, T. H. *et al.* Loss of PBRM1 and BAP1 Expression Is Less Common in Non-Clear Cell Renal Cell Carcinoma Than in Clear Cell Renal Cell Carcinoma. *Urol. Oncol.* **33**, 23.e9–23.e14 (2015).
142. Mashtalir, N. *et al.* Modular Organization and Assembly of SWI/SNF Family Chromatin Remodeling Complexes. *Cell* **175**, 1272–1288.e20 (2018).
143. Roumeliotis, T. I. *et al.* Genomic Determinants of Protein Abundance Variation in Colorectal Cancer Cells. *Cell Rep.* **20**, 2201–2214 (2017).
144. Yan, Z. *et al.* PBAF chromatin-remodeling complex requires a novel specificity subunit, BAF200, to regulate expression of selective interferon-responsive genes. *Genes Dev.* **19**, 1662–1667 (2005).

145. Tresini, M. *et al.* The core spliceosome as target and effector of non-canonical ATM signalling. *Nature* **523**, 53–58 (2015).
146. Sollier, J. & Cimprich, K. A. Breaking bad: R-loops and genome integrity. *Trends Cell Biol.* **25**, 514–522 (2015).
147. Gorthi, A. *et al.* EWS–FLI1 increases transcription to cause R-loops and block BRCA1 repair in Ewing sarcoma. *Nature* **555**, 387–391 (2018).
148. Shivji, M. K. K., Renaudin, X., Williams, Ç. H. & Venkitaraman, A. R. BRCA2 Regulates Transcription Elongation by RNA Polymerase II to Prevent R-Loop Accumulation. *Cell Rep.* **22**, 1031–1039 (2018).
149. Hatchi, E. *et al.* BRCA1 Recruitment to Transcriptional Pause Sites Is Required for R-Loop-Driven DNA Damage Repair. *Mol. Cell* **57**, 636–647 (2015).
150. Cohen, S. *et al.* Senataxin resolves RNA:DNA hybrids forming at DNA double-strand breaks to prevent translocations. *Nat. Commun.* **9**, 533 (2018).
151. Burrows, A. E., Smogorzewska, A. & Elledge, S. J. Polybromo-associated BRG1-associated factor components BRD7 and BAF180 are critical regulators of p53 required for induction of replicative senescence. *Proc. Natl. Acad. Sci. U. S. A.* **107**, 14280–14285 (2010).
152. Espana-Agusti, J., Warren, A., Chew, S. K., Adams, D. J. & Matakidou, A. Loss of PBRM1 rescues VHL dependent replication stress to promote renal carcinogenesis. *Nat. Commun.* **8**, 2026 (2017).
153. Kuzmanov, A., Karina, E. I., Kirienko, N. V. & Fay, D. S. The Conserved PBAF Nucleosome-Remodeling Complex Mediates the Response to Stress in *Caenorhabditis elegans*. *Mol. Cell. Biol.* **34**, 1121–1135 (2014).
154. Gao, W., Li, W., Xiao, T., Liu, X. S. & Kaelin, W. G. Inactivation of the PBRM1 tumor suppressor gene amplifies the HIF-response in VHL^{-/-} clear cell renal carcinoma. *Proc. Natl. Acad. Sci.* **114**, 1027–1032 (2017).
155. Cai, W. *et al.* PBRM1 acts as a p53 lysine-acetylation reader to suppress renal tumor growth. *Nat. Commun.* **10**, 5800 (2019).
156. Couch, F. B. *et al.* ATR phosphorylates SMARCAL1 to prevent replication fork collapse. *Genes Dev.* **27**, 1610–1623 (2013).
157. Edmunds, J. W., Mahadevan, L. C. & Clayton, A. L. Dynamic histone H3 methylation during gene induction: HYPB/Setd2 mediates all H3K36 trimethylation. *EMBO J.* **27**, 406–420 (2008).
158. Pfister, S. X. *et al.* SETD2-Dependent Histone H3K36 Trimethylation Is Required for Homologous Recombination Repair and Genome Stability. *Cell Rep.* **7**, 2006–2018 (2014).

159. Carvalho, S. *et al.* SETD2 is required for DNA double-strand break repair and activation of the p53-mediated checkpoint. *eLife* **3**, e02482 (2014).
160. Identification and analysis of functional elements in 1% of the human genome by the ENCODE pilot project. *Nature* **447**, 799–816 (2007).
161. Chiang, Y. C. *et al.* SETD2 Haploinsufficiency for Microtubule Methylation is an Early Driver of Genomic Instability in Renal Cell Carcinoma. *Cancer Res. canres.3460.2017* (2018) doi:10.1158/0008-5472.CAN-17-3460.
162. Kanu, N. *et al.* SETD2 loss-of-function promotes renal cancer branched evolution through replication stress and impaired DNA repair. *Oncogene* **34**, 5699–5708 (2015).
163. Pfister, S. X. *et al.* Inhibiting WEE1 Selectively Kills Histone H3K36me3-Deficient Cancers by dNTP Starvation. *Cancer Cell* **28**, 557–568 (2015).
164. Abou Alaiwi, S. *et al.* Mammalian SWI/SNF Complex Genomic Alterations and Immune Checkpoint Blockade in Solid Tumors. *Cancer Immunol. Res. canimm;2326-6066.CIR-19-0866v2* (2020) doi:10.1158/2326-6066.CIR-19-0866.
165. Zhou, H. *et al.* PBRM1 mutation and preliminary response to immune checkpoint blockade treatment in non-small cell lung cancer. *Npj Precis. Oncol.* **4**, 1–4 (2020).
166. Sun, L., Wu, J., Du, F., Chen, X. & Chen, Z. J. Cyclic GMP-AMP Synthase is a Cytosolic DNA Sensor that Activates the Type-I Interferon Pathway. *Science* **339**, (2013).
167. Pantelidou, C. *et al.* PARP Inhibitor Efficacy Depends on CD8+ T-cell Recruitment via Intratumoral STING Pathway Activation in BRCA-Deficient Models of Triple-Negative Breast Cancer. *Cancer Discov.* **9**, 722–737 (2019).
168. Ding, L. *et al.* PARP Inhibition Elicits STING-Dependent Antitumor Immunity in Brca1-Deficient Ovarian Cancer. *Cell Rep.* **25**, 2972–2980.e5 (2018).
169. Sen, T. *et al.* Targeting DNA Damage Response Promotes Antitumor Immunity through STING-Mediated T-cell Activation in Small Cell Lung Cancer. *Cancer Discov.* **9**, 646–661 (2019).
170. Samstein, R. M. *et al.* Tumor mutational load predicts survival after immunotherapy across multiple cancer types. *Nat. Genet.* **51**, 202–206 (2019).
171. Peyraud, F. & Italiano, A. Combined PARP Inhibition and Immune Checkpoint Therapy in Solid Tumors. *Cancers* **12**, 1502 (2020).

Titre : Exploration de stratégies thérapeutiques ciblant la déficience en PBRM1 dans les carcinomes rénaux à cellules claires

Mots clés : létalité synthétique ; PBRM1 ; cancer du rein ; inhibiteurs de PARP

Résumé : L'inactivation de polybromo-1 (PBRM1) est un évènement fréquent dans de nombreux cancers. En particulier, les carcinomes rénaux à cellules claires présentent une déficience en PBRM1 dans 40 à 50% des cas. A ce jour, il n'existe pas d'approche de médecine précision connue capable de cibler spécifiquement les cellules tumorales déficientes en PBRM1.

Pour identifier des cibles de létalité synthétique associées à la perte de PBRM1, nous avons (i) réalisé un criblage pharmacologique à haut débit évaluant la sensibilité à 167 molécules dans un modèle cellulaire isogénique pour PBRM1, et (ii) étudié l'impact transcriptomique et protéomique de la perte de PBRM1 dans ce même modèle.

Nous avons ensuite caractérisé les mécanismes sous-jacents à la relation de létalité synthétique découverte.

Nous avons identifié et validé une relation de létalité synthétique existante entre la perte tumorale de PBRM1 et l'inhibition pharmacologique de PARP, pouvant être potentialisée par l'ajout d'un inhibiteur d'ATR.

Cette relation de létalité synthétique était caractérisée par un niveau basal élevé de stress cellulaire chez les cellules déficientes en PBRM1, associant anomalies mitotiques, stress transcriptionnel et stress réplcatif – tous ces phénomènes étant exacerbés à l'ajout d'inhibiteurs de PARP, jusqu'à dépasser les capacités cellulaires à maintenir un phénotype compatible avec la survie.

Ces observations apportent la preuve de concept préclinique que les inhibiteurs de PARP sont de potentiels candidats thérapeutiques pour cibler spécifiquement les tumeurs déficientes en PBRM1.

Title : Identifying synthetic lethal and selective approaches to target PBRM1-deficiency in clear cell renal cell carcinoma

Keywords : synthetic lethality ; PBRM1 ; kidney cancer ; PARP inhibitors

Abstract : Polybromo-1 (PBRM1) inactivation occurs in multiple malignancies and is of particular importance in clear cell renal cell carcinomas (ccRCC), as it drives 40 to 50% of cases. Currently, no precision-medicine approach uses PBRM1 deficiency to specifically target tumour cells.

To uncover novel synthetic lethal approaches to treat PBRM1-defective cancers, we performed (i) a high-throughput pharmacological screening, evaluating the sensitivity to 167 small molecules in a PBRM1-isogenic cellular model, and the (ii) systematic mapping of the whole transcriptomic and proteomic profiles associated with PBRM1 loss-of-function within this model.

We further investigated the mechanism underlying this synthetic lethal relationship.

We identified and validated synthetic lethal effects between PBRM1 loss and both PARP and ATR inhibition. Combinatorial use of PARP with ATR inhibitors exerted additive cytotoxic effects in PBRM1-defective tumor cells.

These synthetic lethal relationships were characterized by a pre-existing replication stress in PBRM1-deficient cells associated with mitosis and DNA damage repair abnormalities, which were exacerbated upon PARP inhibition selectively in PBRM1-defective cells.

These data provide the preclinical basis for evaluating PARP inhibitors as a monotherapy or in combination in patients with PBRM1-deficient ccRCC.